3-1-2015

Synchrophasor Sensing and Processing Based Smart Grid Security Assessment for Renewable Energy Integration

Huaiguang Jiang
University of Denver

Recommended Citation

Jiang, Huaiguang, "Synchrophasor Sensing and Processing Based Smart Grid Security Assessment for Renewable Energy Integration" (2015). *Electronic Theses and Dissertations*. 319.
https://digitalcommons.du.edu/etd/319

Synchrophasor Sensing and Processing based Smart Grid Security Assessment for Renewable Energy Integration

a dissertation

Presented to

the Faculty of the Daniel Felix Ritchie School of Engineering and Computer Science

University of Denver

in Partial Fulfillment

of the Requirements for the Degree

of Doctor of Philosophy

by

Huaiguang Jiang

March 2015

Advisor: Jun Zhang

Author: Huaiguang Jiang
Title: Synchrophasor Sensing and Processing based Smart Grid Security Assessment for Renewable Energy Integration
Advisor: Jun Zhang
Degree Date: March 2015

Abstract

With the evolution of energy and power systems, the emerging Smart Grid (SG) is mainly featured by distributed renewable energy generations, demand-response control and huge amount of heterogeneous data sources. Widely distributed synchrophasor sensors, such as phasor measurement units (PMUs) and fault disturbance recorders (FDRs), can record multi-modal signals, for power system situational awareness and renewable energy integration.

An effective and economical approach is proposed for wide-area security assessment. This approach is based on wavelet analysis for detecting and locating the short-term and long-term faults in SG, using voltage signals collected by distributed synchrophasor sensors.

A data-driven approach for fault detection, identification and location is proposed and studied. This approach is based on *matching pursuit decomposition* (MPD) using Gaussian atom dictionary, *hidden Markov model* (HMM) of real-time frequency and voltage variation features, and fault contour maps generated by machine learning algorithms in SG systems. In addition, considering the economic issues, the placement optimization of distributed synchrophasor sensors is studied to reduce the number of the sensors without affecting the accuracy and effectiveness of the proposed approach. Furthermore, because the natural hazards is a critical issue for power system security, this approach is studied under different types of faults caused by natural hazards.

A fast steady-state approach is proposed for voltage security of power systems with a wind power plant connected. The impedance matrix can be calculated by the voltage and current information collected by the PMUs. Based on the impedance matrix, locations in SG can be identified, where cause the greatest impact on the voltage at the wind power plants point of interconnection. Furthermore, because this dynamic voltage security assessment method relies on time-domain simulations of faults at different locations, the proposed approach is feasible, convenient and effective.

Conventionally, wind energy is highly location-dependent. Many desirable wind resources are located in rural areas without direct access to the transmission grid. By connecting MW-scale wind turbines or wind farms to the distributions system of SG, the cost of building long transmission facilities can be avoid and wind power supplied to consumers can be greatly increased. After the effective wide area monitoring (WAM) approach is built, an event-driven control strategy is proposed for renewable energy integration. This approach is based on support vector machine (SVM) predictor and multiple-input and multiple-output (MIMO) model predictive control (MPC) on linear time-invariant (LTI) and linear time-variant (LTV) systems. The voltage condition of the distribution system is predicted by the SVM classifier using synchrophasor measurement data. The controllers equipped with wind turbine generators are triggered by the prediction results. Both transmission level and distribution level are designed based on this proposed approach.

Considering economic issues in the power system, a statistical scheduling approach to economic dispatch and energy reserves is proposed. The proposed approach focuses on minimizing the overall power operating cost with considerations of renewable energy uncertainty and power system security. The hybrid power system scheduling is formulated as a convex programming problem to minimize power operating cost, taking considerations of renewable energy generation, power generation-consumption balance and power system security. A genetic algorithm based approach is used for solving the minimization of the power operating cost.

In addition, with technology development, it can be predicted that the renewable energy such as wind turbine generators and PV panels will be pervasively located in distribution systems. The distribution system is an unbalanced system, which contains single-phase, two-phase and three-phase loads, and distribution lines. The complex configuration brings a challenge to power flow calculation. A topology analysis based iterative approach is used to solve this problem. In this approach, a self-adaptive topology recognition method is used to analyze the distribution system, and the backward/forward sweep algorithm is used to generate the power flow results.

Finally, for the numerical simulations, the IEEE 14-bus, 30-bus, 39-bus and 118-bus systems are studied for fault detection, identification and location. Both transmission level and distribution level models are employed with the proposed control strategy for voltage stability of renewable energy integration. The simulation results demonstrate the effectiveness of the proposed methods. The IEEE 24-bus reliability test system (IEEE-RTS), which is commonly used for evaluating the price stability and reliability of power system, is used as the test bench for verifying and evaluating system performance of the proposed scheduling approach.

Acknowledgements

I would like to extend my sincere gratitude to my supervisor Dr. Jun Jason Zhang for his continuous advice and support for my PhD study and research. I am deeply grateful of his help in the completion of this dissertation. Since Jan, 2012, Dr. Jun Jason Zhang has deeply influenced me in different aspects of my life, not only through his great guidance in research, but also through his patience, preciseness, enthusiasm, and genuine concern for students. His high standards for the quality of work has encouraged me to purse better and perfection of each project and work. I learned a lot of knowledge from his excellent performance in teaching and research capabilities as well as high motivation and responsibility to his students.

I also gratefully thank Dr. Yingchen Zhang, who is an engineer working in the National Renewable Energy Laboratory (NREL). From April 2013, the research experience in NREL granted me a lot of knowledge in renewable energy integration, control strategy and economic dispatch. He was and remains one of my best role models for an engineer, mentor and teacher. I am also deeply indebted to all the other tutors and teachers for their direct and indirect help to me.

Last but not least, I am indebted to my mother Anwen Ning, my father Xuman Jiang for their continuous support and encouragement. I dedicate this dissertation to my family as an inadequate appreciation of everything that they have done for me.

Table of Contents

List of Tables

List of Figures

Chapter 1

Introduction

1.1 Motivation and background

In the last decades, the increasing demand of energy world wide requires to rapid development of modern power systems and renewable energy. The future intelligent power system faces new challenges in dealing with extremely large data sets, often called big data, and using them to improve power system wide area monitoring (WAM), stability margin prediction, fault detection, identification, location, power system control and decision making [68, 59, 110].

Smart sensors are being widely embedded in the modern power system as devices such as phasor measurement unit (PMU) and fault disturbance recorder (FDR) [43, 121, 40]. Compared to the traditional slow-response supervisory control and data acquisition (SCADA) system, the PMUs and FDRs can generate measurements with a high data rate to help better analyze wide area events. Furthermore, wide-area monitoring data can be utilized to implement new approaches for better situational awareness and help operators determine the best response to an event, or allow system to act autonomously in cases where human response time would be exceedingly slow.

In addition to the data directly from the power system, other very large data sets are also widely used in power system operation, such as weather data, data from the National Lightning Detection Network (NLDN), Geographic Information System (GIS) data, and electricity market data [68, 39, 110]. For example, the weather data and GIS data are increasingly significant in light of variable renewable sources such as wind farms and solar farms. The electricity market data is also important to facilitate applications such as distributed demand response, integration of distributed renewable energy resources (DERs), and electric vehicles.

After sensor data collection, the network architecture and the communication medium in the modern power system is used to fulfill the diverse requirements for the event information exchange and event-driven control. For example, the protection information and commands exchanged between the intelligent electronic devices in a distribution grid will require a lower network latency than the SCADA information messages exchanged between electrical sensors and control centers. Moreover, the information exchanged can be event-driven such as for protection and control purposes, or periodic such as for real-time monitoring.

The optimal scheduling of economic dispatch and energy reserves in a hybrid power system becomes a new challenge in renewable energy integration (REI) recently. The scheduling objective is minimizing the power operating cost in a hybrid power system with high renewable energy penetration. A credible scheduling economic dispatch and energy reserves is able to increase the efficiency of the power production and ensure the reliability of the power system operations. The population around world is predicted to double by 2050 [59], and the energy demand would be certainly keep growing. As what has happened, the energy demand rised and the prices of some energy resources increased over last two or three decades. To enhance the energy demand rising and avoid environment pollution increasing simultaneously, one solution is to use much more renewable energy from wind , solar and others. In [121], the wind power capacity is expected to increase to $48,000$ MW by 2020 which is threefold to the amount in 2004.

With technology development, distributed wind turbine generators and PV panels are widely located in distribution power systems. Different from transmission system, the distribution system is an unbalanced three-phase system, which contains single-phase, two-phase and three-phase loads, and distribution lines, which results in that the power flow calculation of distribution systems is different from that of transmission systems.

1.2 Contribution

The objective of this dissertation is to propose a novel power system security approach for renewable energy integration based on synchrophasor measurement units, such as PMUs and FDRs. First, with the widespread PMUs and FDRs, the power system security monitoring is studied as the beginning. Second, based on the monitoring results, the control strategy with the renewable energy integration is investigated to improve the performance of the hybrid power system. Finally, considering the stochastic characteristic of the renewable energy and the robustness of the hybrid power system, a credible scheduling economic dispatch method is studied and proposed in this paper. In detail, the contribution of this paper is listed as following:

1. A power system fault detection and fault location method is proposed based on wavelet analysis and unsupervised learning algorithm.
    (a) Based on the wavelet analysis, the fault signal features can be extracted and further processed by the clustering algorithm.
    (b) With the fault contour map, the fault can be located in a short time.

2. Based on the method above, a fault detection, identification and location method is proposed.
    (a) Compared to the wavelet analysis, the MPD is more robust and higher efficient.
    (b) The HMM provides a high accuracy for fault detection and identification rate under different fault scenarios.
    (c) A hybrid clustering algorithm is proposed to provide an efficient and effective way to generate the fault contour map.
3. Considering the impact of the wind power plant, a fast steady-state voltage stability security assessment is proposed.
    (a) With the impedance matrix, the voltage security of the hybrid system can be evaluated.
    (b) The impact of the wind power plant can be calculated.
4. After system monitoring, a novel auxiliary coordinated-control method is investigated in high wind power penetration scenarios.
    (a) A MIMO coordinated-control strategy is proposed for both LTI and LTV power systems.
    (b) The method is investigated in different types of wind turbine generators located in both transmission and distribution systems.
    (c) The proposed control strategy can be easily adapted to cooperate with exiting voltage control methods.
5. Based on the dynamic programming and stochastic control strategy, a economic dispatch method is studied in this paper.

    (a) Both Weibull distribution and Gaussian distribution are studied for the wind speed model.
    (b) The chance constrain is developed from a probability format into a feasible convex format in order to solve the nonlinear stochastic problem.

6. Considering the renewable energy in distribution system, a power flow problem in distribution system is researched.
    (a) Both depth-first search and breadth-first search is used to analyze the topology information of a distribution system
    (b) Based on the topology analysis, the backward/forward sweep algorithm is used to calculate the power flow.

1.3 Dissertation outline

In Chapter 1, the literature of current research are studied, which provides the motivation, rationale and background for the paper. In Chapter 2, WAM is carefully studied in different SGs including fault detection, identification and location. Considering the economic issue, the optimization placement of the distributed synchrophasor sensors is studied to reduce the number of the sensors. In addition, considering the wind power peneration is increasing, a fast voltage security assessment approach is investigated for a wind power plant. In Chapter 3, an even-driven control strategy is proposed for renewable energy integration, which contains both transmission level and distribution level. The economic dispatch strategy for the hybrid power system is also presented, and a distribution system power flow problem is researched. In Chapter 4, in the numerical simulation part, the IEEE 14, 30, 39, 118 system are studied for fault detection, identification and location. Both transmission level and distribution level model are built for renewable energy integration. The simulation results demonstrate the effectiveness of the proposed methods.

Chapter 2

Literature review

The Smart Grid (SG) is regarded as the new generation of power grid, for its improved energy efficiency, profiled demand, maximized utility, reduced cost and controlled emission. The SG uses two independent flows of electricity and information to create a widely distributed automated energy delivery network [43, 77, 94, 141].

2.1 Current research on wide area monitoring

A frequency disturbance recorder (FDR) is a real-time data acquisition device attached in SG, which is less expensive and easier to install than PMU. The FDR can provide synchronized measurements of multi-dimensional information such as voltage, phase angle and frequency, all of which are essential for wide-area monitoring (WAM) applications. With such capability of distributed FDRs, once a fault takes place, the resulting multi-modal signals can be recorded to help diagnose the fault type and locate the topological position, which is critical for shortening the response time and improving the reliability of the SG system in avoiding cascading outages [18, 67, 95, 137].

A fault detection and identification mechanism is necessary for secure SG operations. With regard to fault detection, a system line outage detection method is designed in [120] based on phasor angle measurements and system topology information. Furthermore, in [119], this method is developed for double line outage detection. A power network adaption of the worst configuration heuristics is developed combined with linear programming algorithm in [31] to predict power grid weak points. For fault identification, in [23], four feature selection methods, hypothesis test, stepwise regression, stepwise selection by Akaike's information criterion, and LASSO/ALASSO are compared to identify their applicabilities. In [24], a fault detection and identification method is proposed based on Petri net, which is designed to capture the modelling details of the protection system of the distribution network. A discrimination method on transient voltage stability and voltage sag is proposed in [113]. In this method, the matching pursuit decomposition (MPD) with sinusoid dictionary is used for feature extraction and the learning vector quantization (LVQ) network is used for discriminating different types of voltage signals. In [123], a framework is described for utilizing FDR measurements for steady-state stability analysis and computation of system stability limits.

Once a fault in SG is detected and identified, the next step is to locate its geographic position and estimate its region of influence. In [52, 53], a fault location method is proposed based on Gaussian Markov random field (GMRF) using the phasor angle measurements across the buses in SG. In [45, 99], a wavelet-based method is designed for fault detection and location. Using the maximum wavelet coefficients (WCs) of the frequency and voltage signals under fault disturbance, the relationship between the WCs and power variation is investigated, which is shown to improve the accuracy of load and fault location estimation. In [83], through forced low-frequency oscillation, a fault location method is proposed based on the signals collected from FDRs, which are attached on the ultra-high and high-voltage buses. This method takes the advantage of FDR measurements to reduce the searching area for locating disturbance sources. In [114], certain types of incipient failures are detected from substation waveforms by intelligent distribution fault anticipation (DFA) algorithms with the discussion on related data requirements and processing analysis.

In power systems, fault detection, identification and location usually need to be solved as a unified problem. However, most methods discussed in previous literature focus on only one or two aspects and cannot solve the three problems simultaneously. It can be foreseen that a multi-functional approach, which can achieve fault detection, identification and location, will have a wide range of applications in SG systems. In the last few decades, research in machine learning [72, 2, 96, 134, 133] has advanced data-driven approaches to detect and diagnose faults in power systems. However, in real-world applications, there are many factors that affect and deteriorate measured signals from FDRs, which requires the fault detection, classification and location approaches to be highly effective and robust. Economic issues also need to be considered, as equipment, installation and maintenance costs are some of the major concerns in power systems. Therefore, it is imperative to study a multi-functional method, which is flexible, robust, effective and economic to meet the future power system requirements [18, 43, 101].

In addition, although the machine learning based fault analysis approaches are accurate and comprehensive, a relative simple approach is proposed in this paper as a supplement, which is focusing on voltage stability assessment for the power systems with wind power plants. Voltage stability assessment methods in power systems can be classified into two categories: dynamic simulation and steady-state. A dynamic simulation is a method in which a high-accuracy dynamic test bench is built to determine the fault impact. To generate an accurate analysis of voltage stability, the dynamic test bench includes excitation systems, capacitors, high-order generator models, relay protections, and so on. In [32], the dynamic simulation provides a more accurate result than that of the V-Q power flow simulation. In [15], dynamic wind turbine models are built to study the voltage stability of the power system with a large amount of wind power. Although the dynamic approach is accurate, this method relies on time-domain simulations of faults at different locations. Ref. [93] illustrates that steady-state analysis provides another effective way to analyze voltage stability. In [51], a steady-state method is used to assess voltage security by using decision tree. In [124], by using times-series power flow, a steady-state method is used to analyze voltage stability of power system with high penetrations of wind. By using artificial intelligence in [61], a steady-state method is used to analyze voltage stability of power system. Assuming the involved dynamics are very slow, a steady-state method is designed for the voltage collapse analysis [13, 11, 12].

2.2 Current research on renewable energy integration

The voltage control of a power system with high penetration of renewable resources becomes a major concern recently [43]. The objective of voltage control in power systems is monitoring the voltage and keeping voltage stability margin within an acceptable range in the presence of various disturbances [116]. With the development and large deployment of synchrophasor measuring device (also known as phasor measurement unit - PMU), a real time data acquisition can be achieved in synchronized time frame over hundreds of buses consisting of multi-dimensional information (i.e. voltage magnitude, phase angle and frequency) [111, 58]. Using the synchrophasor measurements, the wide-area monitoring system (WAMS) based transient voltage stability prediction and control strategy with renewable energy is proposed in this paper.

There are two major classic methods to determine the transient stability status of a power system, one is the time-domain simulation of the system nonlinear differential equations and the other is the Lyapunov stability or energy function principle based transient-energy-function (TEF) method [4, 102]. However, the first one requires accurate information of the network configuration and the second requires the levels of kinetic energy and potential energy, which are not easy to determine [73, 102].

Recently, machine learning and data mining based methods are attracting more attention. Examples of these methods include artificial neural network (ANN), decision tree (DT), and support vector machine (SVM). These methods provide a new promising way to analyze power system stability [134, 133]. The perturbation in the power system network can cause power imbalance between generation and load, and it can affect generator angles and generator speed in the power system. Meanwhile, the post-fault voltage can also be used to decipher the perturbations. Reference [47] illustrates method to predict the outcome of system stability by observing and analyzing a short-term post-fault period. In this paper, an support vector machine (SVM) based modelling method is developed to predict stability of a power system with high penetration renewable source.

The use of traditional proportional-integral derivative (PID) control strategy has limitations for multiple-input and multiple-output (MIMO) or nonlinear control systems with constraints. The PID based control solution decomposes a complex system into single-input single-output loops such as cascaded systems, or linearizes the system around an operating point in a very small range [5, 7].

On the other hand, the model predictive control (MPC) action at the current time step is obtained by solving a finite horizon open-loop optimal control problem in real-time, using the current state of the system as the initial state. The optimization with respect to control variables yields an optimal control variable sequence and the first control variable in this sequence is applied to the control system [105]. The MPC has several advantages including robust control, easy inclusion of nonlinear systems with constraints and MIMO systems controls [76, 71]. However, due to the high computational complexity and complicated control mechanism, this scheme is not a widely used in power system control. Therefore, it is imperative to study a multi-functional method, which is flexible, robust, effective and economic to meet renewable energy integration requirements [18, 43, 126].

As renewable energy penetration keeps increasing in recent decades, the wind plant playing a more important role in modern power system configuration [39, 110, 108, 129]. The economic scheduling in hybrid power systems becomes an emerging challenge and urgent requirement on the road map of renewable energy integration [80, 130, 122, 127].

In [101], a method is focusing on how to determine the amount of spinning reserve with large wind power penetration. And this method is based on [127] which does not evaluate the impacts of wind generation uncertainty, and concentrates on conventional energy generator outage and load prediction errors. An method of managing stochastic renewable energy generation uncertainty is considered in [112], and the approach generates schedules for a 24-hour period with hourly resolution. In [139], a stochastic optimal power scheduling of generators and reserves with large wind generation is studied on the WSCC-179 buses testing model [9, 112, 90]. A probabilistic method is formulated in [48] to optimize the spinning reserve on different level of loads. This problem is caused by the generator outages or the load forecast errors. In [100], a novel approach is used to determine the optimal reserve with wind penetration in a power system. The mixed-integer linear program is an indispensable issue, which is formulated for the unit commitment problem in [25], which aids to reduce the computational complexity. These can be also found in [130, 109]. The technique focuses on researching the conventional generation outages and load forecasting errors of the system, which shows a larger spinning reserve is not necessarily required if the wind penetration increasing during the operating process.

Chapter 3

Wide area monitoring with synchrophasor measurement systems

In power systems, fault detection, identification and location usually need to be solved as a unified problem. However, most methods discussed in previous literature focus on only one or two aspects and cannot solve the three problems simultaneously. It can be foreseen that a multi-functional approach, which can achieve fault detection, identification and location, will have a wide range of applications in SG systems. In the last few decades, research in machine learning [72, 2, 97, 8] has advanced data-driven approaches to detect and diagnose faults in power systems.

However, in real-world applications, there are many factors that affect and deteriorate measured signals from FDRs, which requires the fault detection, classification and location approaches to be highly effective and robust.

Economic issues also need to be considered, as equipment, installation and maintenance costs are some of the major concerns in power systems. Therefore, it is imperative to study a multi-functional method, which is flexible, robust, effective and economic to meet the future power system requirements [18, 43, 127, 10]. In this chapter, two data-driven computational approaches are proposed to analysis the fault in SGs for WAM. The first is fault location approach based on wavelet analysis. Based on the first approach an advance method is proposed to detect, identify and locate power system faults, which utilizes voltage and frequency signals measured by FDRs. The frequency signals are used to detect and identify different types of fault, and the voltage signals are used to locate the fault in SG.

3.1 Problem formulation of wide area monitoring

The scheme of the IEEE New England 39-bus System is illustrated in Fig. 3.1, which contains 10 generators, 36 transmission lines, 12 transformers and 19 loads. The mathematical notations that describe this power system for our fault analysis method are given as follows. m_l is used to denote the fault type of the lth fault occurrence, where $l = 1, 2, 3, ..., L$ with L being the total number of fault occurrences, $m_l = 1$ represents generator ground fault, $m_l = 2$ represents transmission line outage, $m_l = 3$ represents generator outage and $m_l = 4$ represents load loss. And other type of faults can also be represent with different value of m_l. If $m_l = 0$, the SG is in a normal condition. If there is a fault occurring in the system, the SG is in an abnormal condition; otherwise, it is in a normal condition. The set of the 39 buses for the lth fault occurrence with type m_l is denoted as $\mathcal{S}_l^{(m_l)} = \left\{\mathbf{S}_{1,l}^{(m_l)}, \mathbf{S}_{2,l}^{(m_l)}, \mathbf{S}_{3,l}^{(m_l)}, \cdots, \mathbf{S}_{39,l}^{(m_l)}\right\}$, and $\mathbf{S}_{i,l}^{(m_l)}$ is a set defined as $\mathbf{S}_{i,l}^{(m_l)} = \{\mathbf{F}_{i,l}^{(m_l)}, \mathbf{V}_{i,l}^{(m_l)}\}$, where $i = 1, 2, 3, ..., 39$ is the bus index, $\mathbf{F}_{i,l}^{(m_l)} = \left[f_{i,l}^{(m_l)}[1] \cdots f_{i,l}^{(m_l)}[k] \cdots f_{i,l}^{(m_l)}[K]\right]^T$ represents the discrete time domain frequency measurement vector resulting from the fault type m_l with k as the time index, and T as the matrix transpose. Similarly, $\mathbf{V}_{i,l}^{(m_l)} = \left[v_{i,l}^{(m_l)}[1] \cdots v_{i,l}^{(m_l)}[k] \cdots v_{i,l}^{(m_l)}[K]\right]^T$ represents the voltage signal vector in discrete time domain. This is a example of problem formulation for IEEE New England 39-bus System. Based on this, the other power system model such as the

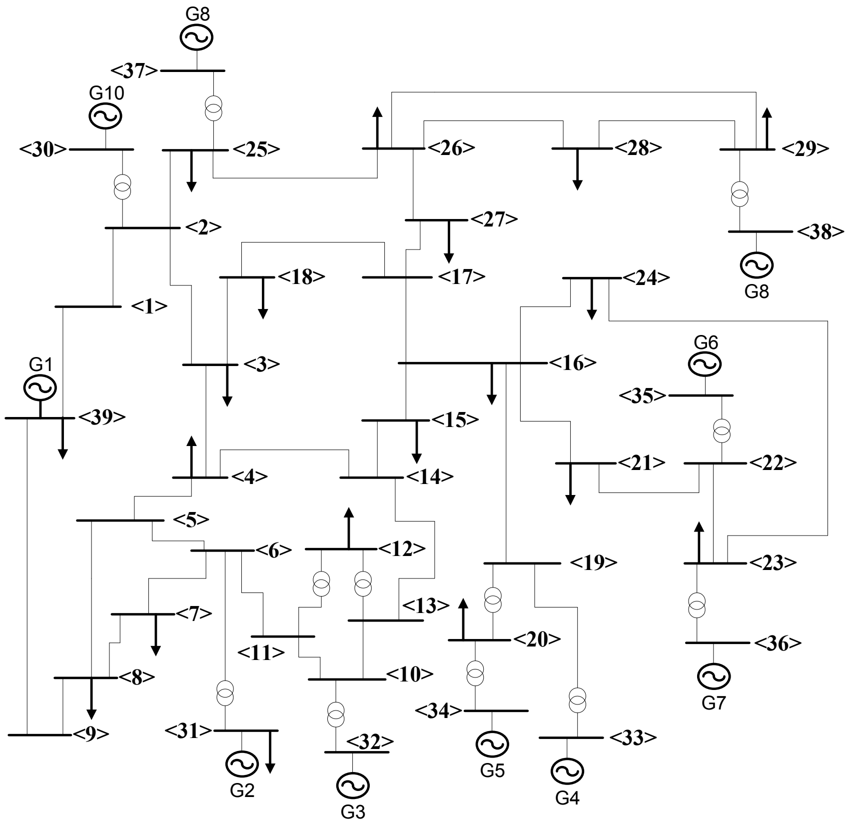

Figure 3.1: The scheme of the IEEE New England 39-bus system.

IEEE 14-bus, 30-bus, 39-bus, 108-bus system can be similarly worked out.

3.2 Wavelet based fault analysis and fault location approach

3.2.1 Architecture of the wavelet based fault analysis

In this section, $c_{i,l}^{(m_l)}$ denotes the feature wavelet transformed coefficients extracted from the wavelet analysis of $\mathbf{V}_{i,l}^{(m_l)}$. The whole data processing flowchart is in Fig. 3.2. After the input real-time voltage signal $\mathbf{V}_{i,l}^{(m_l)}$ are collected, the signals are processed by the wavelet-based multi-resolution analysis and the WCT feature

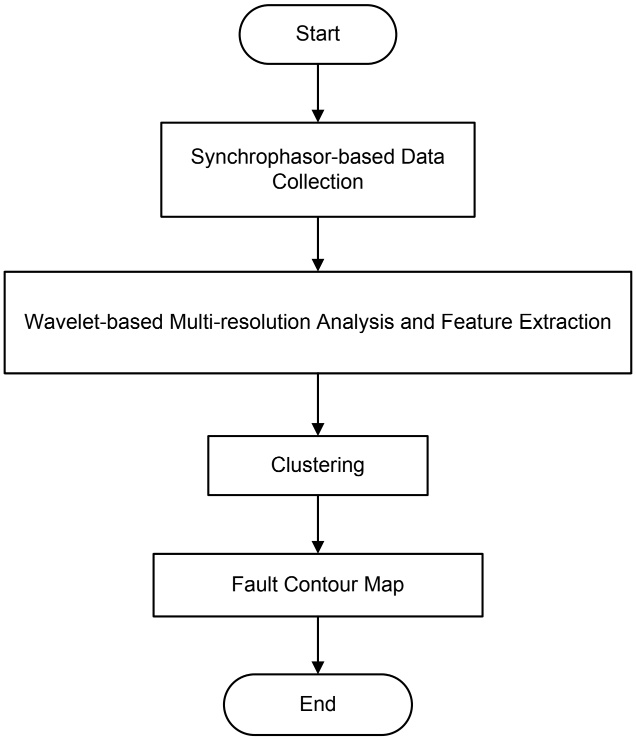

Figure 3.2: The proposed wavelet-based and fault location method.

set $C_l^{(m_l,n_l)}$ are extracted. Then the extracted features are clustered using k-means algorithm to map each feature vector into different subsets for fault location. With the geophysical map of the SG, the fault contour map could be determined and the fault can be localized.

3.2.2 Wavelet analysis of voltage signals

Compared with the Fourier transform that only focuses in frequency domain, wavelet based multi-resolution analysis is able to provide flexible time, frequency and scale domain analysis, especially for edge detection and positioning in time domain [79, 87]. Through the cascading filter bank filters in wavelet analysis, the original signal is divided into several orthogonal subspaces. In the meanwhile, the noise in the original signal is suppressed and the features of the original signal can be extracted and analyzed in certain subspaces. To achieve our goal of signal edge detection and positioning for fault localization, we choose the symlets wavelets as they can 1) accurately locate signal edges when long-term or short-term faults take place, 2) reduce the data volume with its high decomposition level, 3) suppress noise in the original signal, and 4) be suitable for implementation as they are approximate linear filters [79, 87].

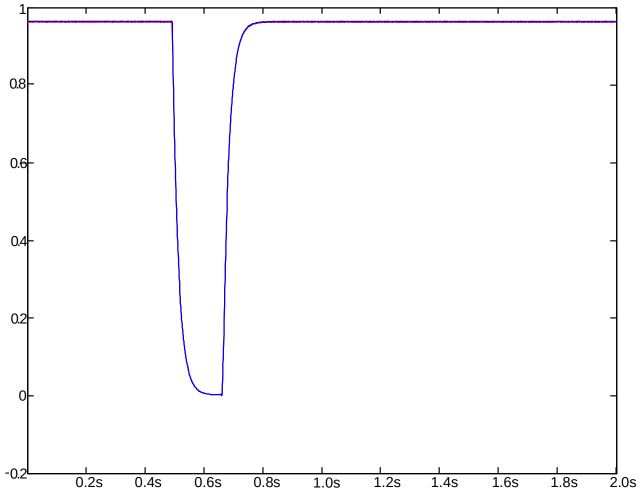

Figure 3.3: Voltage signals for the short term transmission line fault

The results of symlets wavelet analysis for a long-term and a short-term fault are demonstrated in Fig. 3.3, Fig. 3.4, Fig. 3.5, and Fig. 3.6. The voltage signal vector $\mathbf{v}_{i,l}^{(m_l,n_l)}$ is obtained with a sampling rate of 1 kHz which is a common sampling rate for PMUs in realistic system, and the simulation duration is 2 s. We assume that the fault is a transmission line short fault at bus 15, thus $i = 15$. The short term fault starts on 0.5 s and lasts 10 cycles (about 0.167 s). The long-term fault starts on 0.5 s and lasts to the end of the simulation.

Fig. 3.3 demonstrates the voltage signal variation when the fault takes place, and Fig. 3.4 demonstrates its wavelet analysis results. In Fig. 3.4, variable $\mathbf{d}_i$ denotes the symlets wavelet coefficients obtained from the band-pass filter at scale level i,

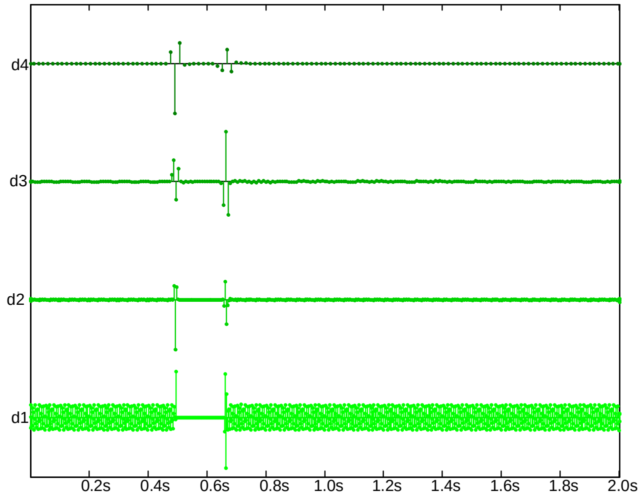

Figure 3.4: Symlets wavelet analysis results for the short-term fault

where $i = \{1, 2, 3, 4\}$. As we can see, the maximum WTCs in $\mathbf{d}_3$ and $\mathbf{d}_4$ indicate the starting or ending of the fault occurrence. At the same time, the maximum WCTs in $\mathbf{d}_4$ is negative, which indicates that the voltage fluctuation is downward at the start. And the maximum WCTs in $\mathbf{d}_3$ is positive, which indicates that the voltage fluctuation is upward at the end.

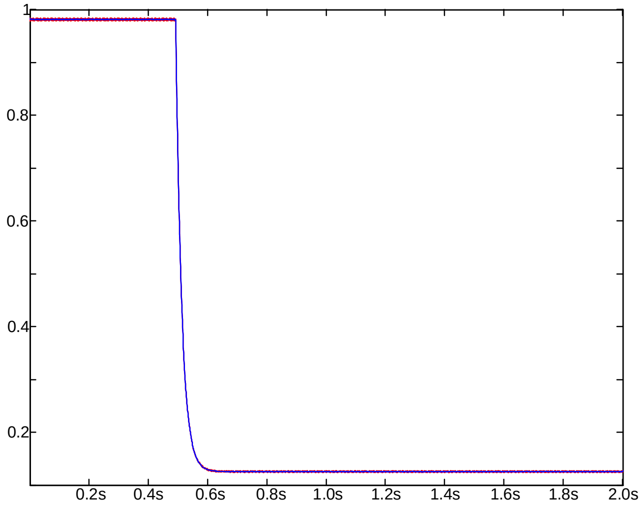

Figure 3.5: Voltage signals for long-term transmission line fault

Similarly, for long term faulty analysis, the maximum WTCs in Fig. 3.6 in $\mathbf{d}_3$ and $\mathbf{d}_4$ also indicate the fault occurrence in time domain. And the maximum WCTs is negative, which also indicates that the voltage fluctuation is downward at this time. In addition, the data volume in $\mathbf{d}_4$ is only 1/16 of the voltage data samples, which compresses the data and release the storage and transmission pressure of the system. As a result, we use the maximum WTCs in $\mathbf{d}_4$ the feature WTCs for further processing for fault localization.

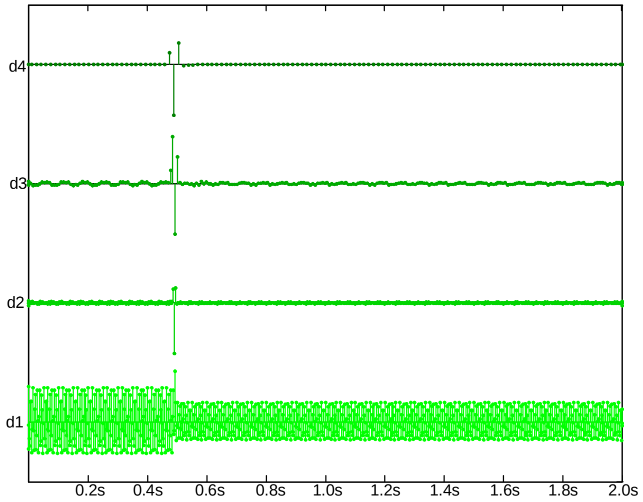

Figure 3.6: Symlets wavelet analysis results for the long-term fault

3.2.3 Noise suppression of wavelet-based fault analysis

In Fig. 3.8, the two maximum WCTs at decomposition level 5 can indicate the fault starting and ending in time domain. And between the two maximum WTCs, the other coefficient are decreasing first and then increasing, which indicate the voltage is decreasing first and then increasing.

For the permanent fault, its symlets wavelet analysis in Fig. 3.10 is not as clear as the transient fault. At decomposition level 5, there are two coefficients between 0.44 s and 0.6 s with almost the same amplitude, which cannot indicate the fault

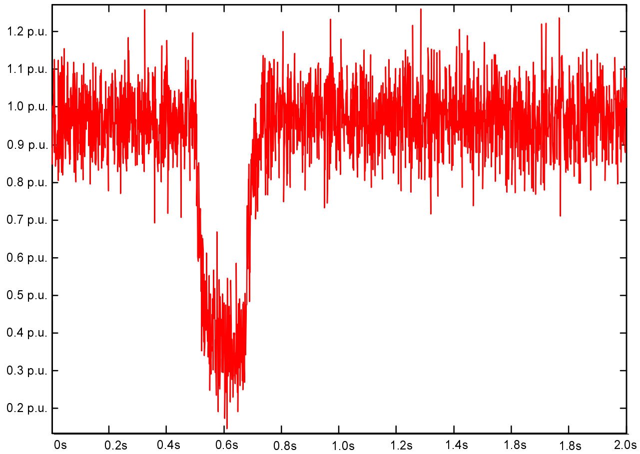

Figure 3.7: Voltage signals with noise of a transient transmission line outage

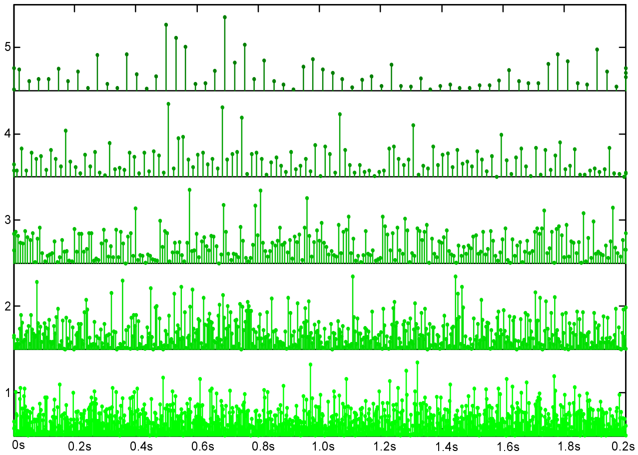

Figure 3.8: Symlets wavelet analysis results for Fig. 3.7

starting clear in the time domain. In sum, in the scenario SNR = 5 dB, the symlets wavelet analysis performance better in transient fault, this because the waveform of the symlets wavelet is more similar to the transient fault, and has higher recognition ability to the transient fault.

In Fig. 3.12, it is clear that the two maximum WTCs between 0.4 s and 0.6 s at decomposition level 5 indicate the starting and ending of the transient fault in time domain. And in Fig. 3.14, the maximum WTCs at decomposition level 5 indicates

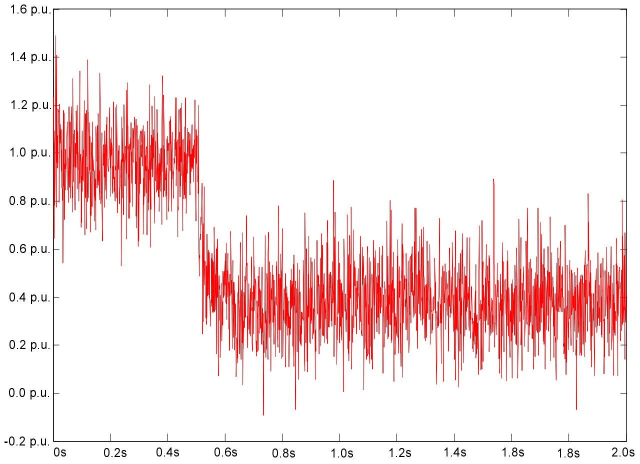

Figure 3.9: Voltage signals with noise of a permanent transmission line outage

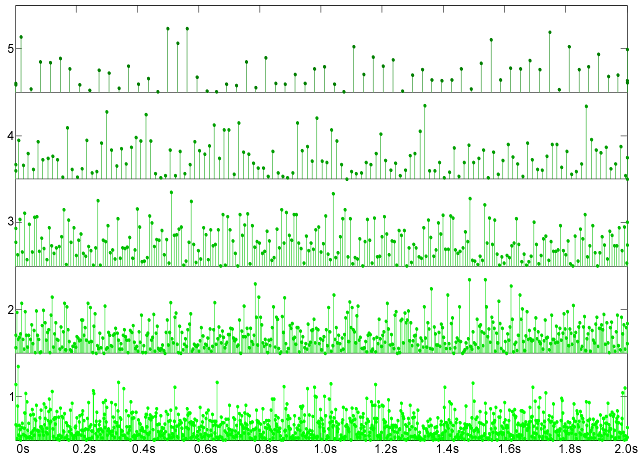

Figure 3.10: Symlets wavelet analysis results for Fig. 3.9

the starting of the permanent fault clearly. This also implies that for the scenario with SNR larger than 10 dB, the symlets wavelet analysis can localize the transient and permanent fault clearly in time domain.

In sum, with the SNR increasing, the symlets wavelet analysis performances better in fault feature extraction and timing localization for both permanent fault and transient fault. But as the experiments, for different fault scenarios, such as the transient fault last for 1 second, the parameters of the wavelet need to be re-selected

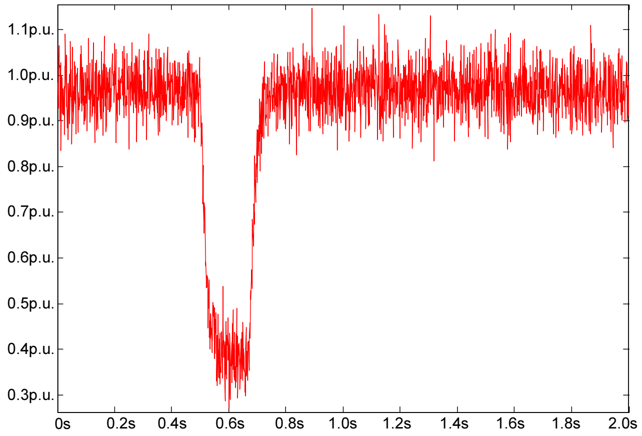

Figure 3.11: Voltage signals with noise of the transient transmission line outage

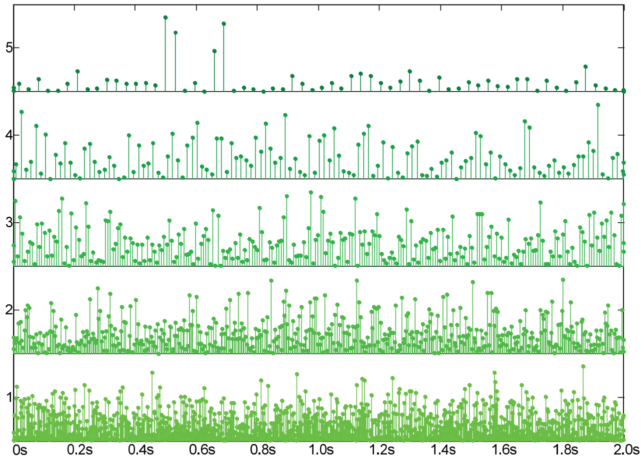

Figure 3.12: Symlets wavelet analysis results for Fig. 3.11

to get the best performance of the fault feature extraction.

3.2.4 Numerical result of transformer fault

A transformer disabling fault at Transformer 12 is simulated in the system. The feature WTCs are clustered into 5 subset as in Table 3.1. The fault can be successfully located using the fault contour map as in Fig. 3.15. The blue circle which is near the boundary of the system corresponds to the subset 5, and represents

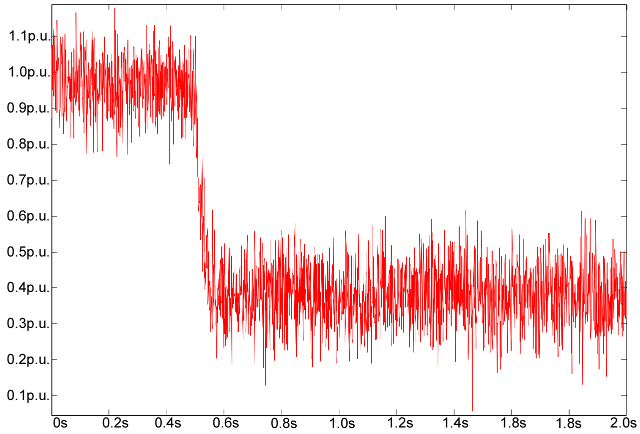

Figure 3.13: Voltage signals with noise of the permanent transmission line outage

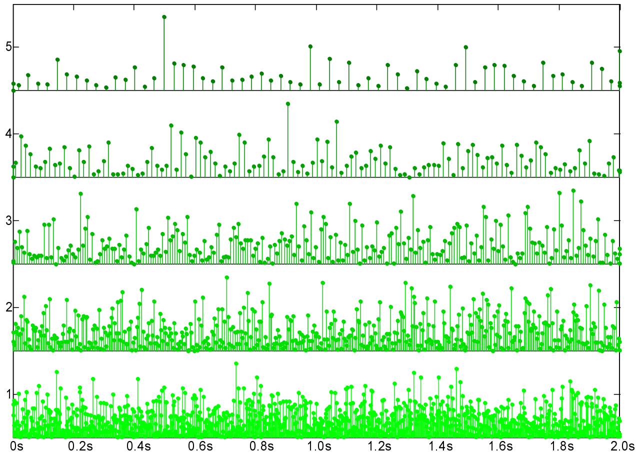

Figure 3.14: Symlets wavelet analysis results for Fig. 3.13

the lowest impact level. In this subset, the buses are either directly connected to the generators or near them, as a result, these buses have the smallest fluctuations in the system as the generators can compensate the voltage fluctuation in power systems. The yellow, orange and pink circles represent the subsets 4, 3 and 2, respectively. The voltage fluctuation gradually increases in these bus subsets. The subset 1 is denoted with a red ellipse with the largest feature WTC value. The red ellipse illustrates that the fault is located in this area. Also, the pink circle indicates the

Table 3.1: Impact level of transformer fault

Level	Bus number
1st (nearest to fault)	13,12
2nd	4,11,14,15
3rd	3,5,6,7,8,9,10,16,17,18,21,24,27
4th	1,2,23,25,26,28,29
5th	19,20,22,30,31,32,33,34,35,36, 37,38,39

area where the electronic equipments would be damaged if the fault exist for a long time.

3.3 Data-driven fault diagnosis approach

This is a multifunctional approach including fault detection, identification and location.

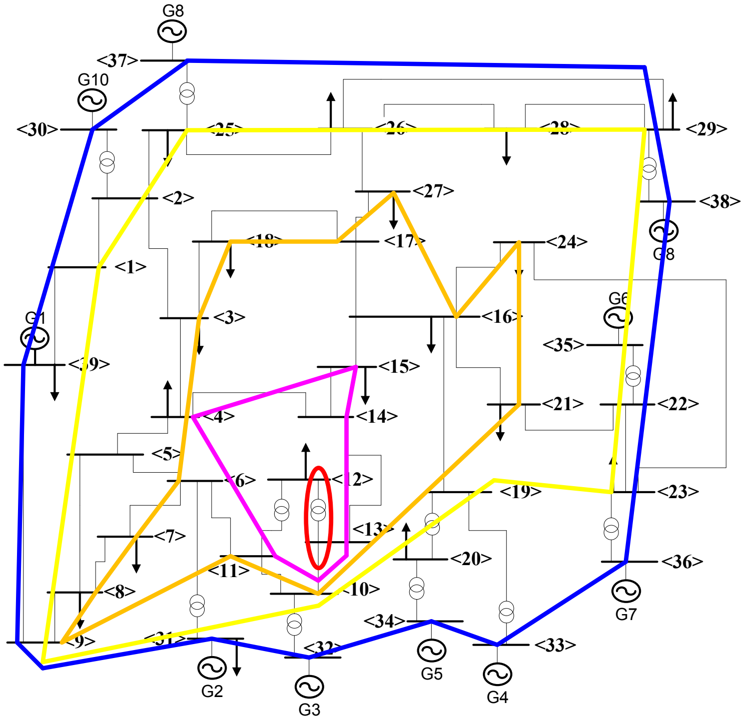

Figure 3.15: The proposed wavelet-based and Fault Location Method.

The first step of fault detection and identification is frequency signal feature extraction, which is achieved by the MPD with Gaussian atom dictionary that provides an effective way to decompose the frequency signals and extract the feature vectors corresponding to certain physical meanings [27, 88]. After a number of MPD iterations, the frequency signals are decomposed into a combination of weighted Gaussian atoms with a small amount of energy in the residual signals. After the MPD feature extraction, a hybrid clustering algorithm is designed to cluster the feature vectors into several subsets, and thus map the feature vectors into different symbols. Then the signal feature transitional properties are modelled with hidden Markov models (HMMs) using the obtained symbols under various normal and faulty operation scenarios. Finally, the HMMs are used to detect and identify the fault.

3.3.1 Architecture of the advanced fault diagnosis approach

In this paper, frequency signals are chosen for fault detection and identification because they are deemed to be closely related to power balance variations [45]. In SG, any disturbance that leads to a large or sudden mismatch of active power causes a frequency variation [41]. For example, if a generator is lost or if there is a significant increase in load, the local frequency will drop immediately. In [45, 22, 41, 14], various methods are proposed for fault detection and identification using frequency signal, which proves that frequency signals are effective in analyzing power system faults. On the other hand, the voltage and current variations caused by fault can indicate the fault position. In [92, 46], fault location methods are proposed using the measured voltage and current signals. In [115, 19], the fault location methods for transmission lines are proposed using measured voltage signals. Based on the success of fault detection, identification and location methods in previous literature, in this paper, the frequency signals are chosen to detect and identify the fault, and voltage signals are chosen to locate the fault in SG, with encouraging results.

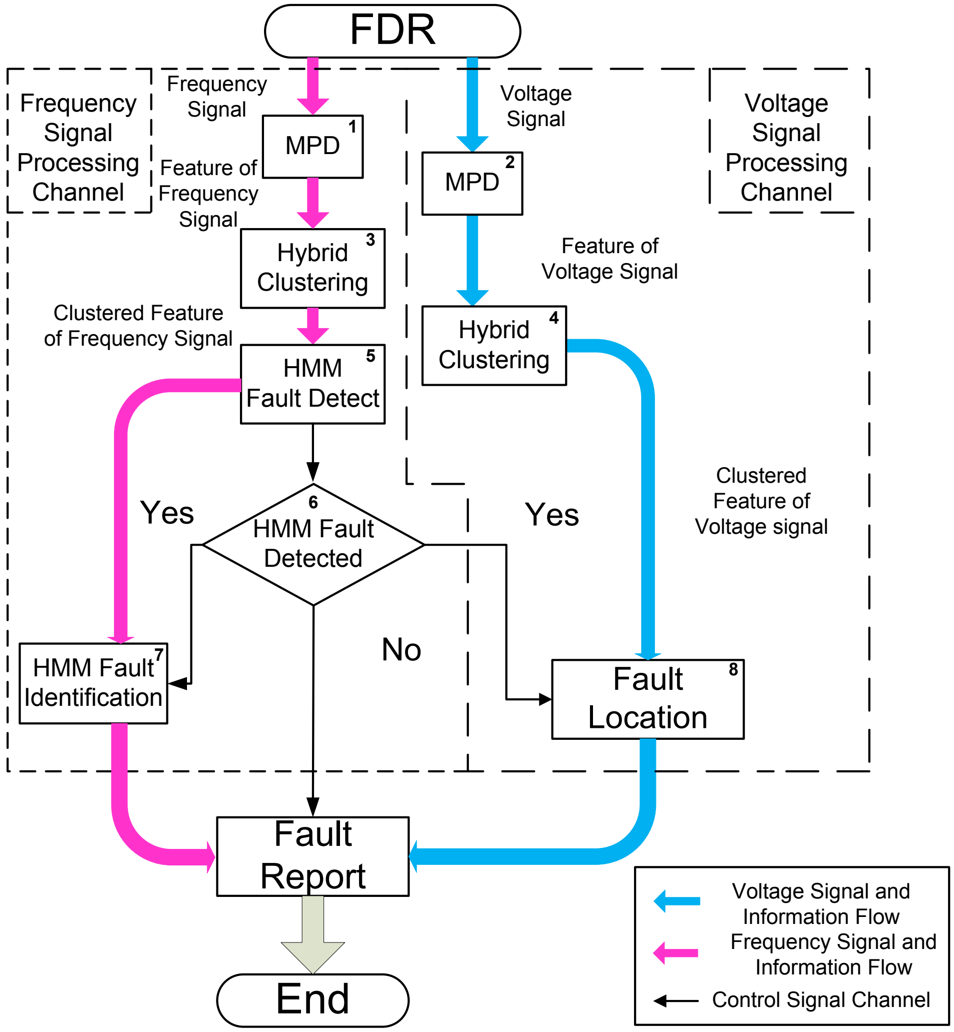

Figure 3.16: The data processing flowchart of the proposed fault analysis method.

The architecture of the proposed approach is illustrated in Fig. 3.16, where the real-time frequency signal and voltage signal are collected by the FDRs in SG. The frequency signal processing channel is used to detect and identify different types of fault. The frequency signal $\mathbf{F}_{i,l}^{(m_l)}$ is processed by the MPD algorithm with Gaussian dictionary for generating frequency feature vector $\mathbf{\Phi}_{i,l}^{(m_l)}$. $\mathbf{\Phi}_{i,l}^{(m_l)} = \left[\Phi_{i,l,1}^{(m_l)}\ \Phi_{i,l,2}^{(m_l)}\ \Phi_{i,l,3}^{(m_l)}\ \cdots\ \Phi_{i,l,P}^{(m_l)}\right]^T$ denotes the feature vector extracted from $\mathbf{F}_{i,l}^{(m_l)}$ by the MPD algorithm where P is the iteration number of the MPD algorithm in Block

1 of Fig. 3.16. Through the hybrid clustering algorithm (Block 3), the frequency features are mapped into symbols, which are used for modelling and training the HMMs for detecting and identifying the faults in the system. In Block 5, two HMMs $\mathbf{\Lambda}^0$ and $\mathbf{\Lambda}^\phi$ are trained and then used for normal and abnormal operating conditions, respectively. Specifically, in the Block 7, the HMM identification block, different HMMs $\left\{\mathbf{\Lambda}^{(m)}, m = 1, 2, 3, 4\right\}$ are trained and then used to identify different types of fault.

Similarly, in the voltage signal processing channel, the MPD is used for extracting voltage signal $\mathbf{\Theta}_{i,l}^{(m_l)}$. Through the hybrid clustering algorithm, the voltage features are clustered into different subsets for fault location. As shown in Fig. 3.16, the arrows from Block 6 to Block 7 and Block 8 represent the control signals. If there is a fault detected by Block 5 and 6, the HMM fault identification (Block 7) and fault localization (Block 8) will be enabled to identify and then locate the fault in SG. Otherwise, the two blocks are not enabled for reducing computational load.

3.3.2 Matching pursuit decomposition for feature extraction

A time-frequency analysis algorithm, MPD, is used to extract data features from frequency and voltage signals. Compared with many time-frequency representations such as Wigner distribution which may result in cross-terms causing information distraction when processed incorrectly, the MPD feature extraction algorithm with Gaussian atom dictionary can decompose the original signal into Gaussian atoms and generate minimum residual signal energy [88]. Compared with the MPD with sinusoid dictionary [113] and MPD with Gabor dictionary [57], the MPD with Gaussian atom dictionary provides more information in each extracted feature vector which includes the amplitude coefficient, time-shift, frequency-shift and variance of the Gaussian atom. This approach has the potential to generate a more dense time-frequency representation.

The MPD algorithm is summarized as following. We denote a continuous signal $f(t)$ which can be decomposed as a weighted summation of the Gaussian signal atoms as

$$f(t) = \sum_{p=1}^{\infty} \alpha_p \, g_p(t) \,, \tag{3.3.1}$$

where $\alpha_p \in \mathcal{A}$ is the coefficient for the Gaussian atom $g_p(t)$ which is selected from a given Gaussian atom dictionary, p is the index of Gaussian atoms and its coefficient. The convergence of this representation is defined as [88]

$$\lim_{N\to\infty} ||f(t) - \sum_{p=1}^{N-1} \alpha_p \, g_p(t)||_2 = 0 \,, \tag{3.3.2}$$

and the energy of $f(t)$ is related to (3.3.1) as

$$E_f = \int_{-\infty}^{\infty} f(t) f^*(t) dt = \sum_{p=1}^{\infty} |\alpha_p|^2 \,, \tag{3.3.3}$$

where $f^*(t)$ is the complex conjugate of $f(t)$, and since every Gaussian atom is normalized, the energy of the signal equals to the sum of the squared coefficient modules. Furthermore, although the orthogonality is not required for the Gaussian atom dictionary $\mathcal{D}$, the completeness is required for the MPD. The original signal $f(t)$ can be represented using decomposition with in finite iterations and a reminder $r_N(t)$ with small energy residual as

$$f(t) = \sum_{p=1}^{N-1} \alpha_p \, g_p(t) + r_N(t) \,. \tag{3.3.4}$$

With the notations in (3.3.4), the MPD algorithm is described as follows. Let $r_1(t) = f(t)$, and search the atoms $g_p(t)$ in the Gaussian atom dictionary $\mathcal{D}$ for the one which has the maximum magnitude of the projection in $r_p(t)$, where $p =$

$1, 2, 3 \cdots P$. Specifically $g_p(t)$ is obtained and $\mathbf{e} = \{\tau, \nu, \sigma\}$ are the time-shifting, frequency-shifting and related normalization coefficient for the Gaussian atoms.

$$g_p(t) = \underset{g^{(\mathbf{e})}(t) \in \mathcal{D}}{\arg\max} \left| \int_{-\infty}^{\infty} r_p(t)\, g^{(\mathbf{e})}(t) dt \right|, \tag{3.3.5}$$

After $g_p(t)$ is obtained, the corresponding coefficient α_p is calculated as

$$\alpha_p(t) = \int_{-\infty}^{\infty} r_p(t)\, g_p(t) dt\,. \tag{3.3.6}$$

The relationship between the reminder $r_p(t)$ and $r_{p+1}(t)$ iteration MPD is

$$r_{p+1}(t) = r_p(t) - \alpha_p\, g_p(t) \tag{3.3.7}$$

where the Nth reminder after $N-1$ iteration is given by $r_N(t) = r_1(t) - \sum_{p=1}^{N-1} \alpha_p\, g_p(t)$. The series $||r_1(t)||_2$, $||r_2(t)||_2$, $\cdots$ $||r_N(t)||_2$ is a monotonically decreasing series and infinitely approaching zero.

The Gaussian atoms we utilize are given by

$$g^{(\mathbf{e})}(t) = \rho^{-1} e^{-\mathcal{K}_x (t-\tau_y)^2} \cos(2\pi\nu_z t) \tag{3.3.8}$$

where ρ is the normalization coefficient given by

$$\rho = (\pi/\mathcal{K}_x)^{1/2} e^{-((2\pi\nu_z)^2/4\mathcal{K}_x)} \cos(2\pi\nu_z\tau_y) \tag{3.3.9}$$

where $\mathcal{K}_x$ is the variance scale with $x = 1, 2, 3, \cdots, X_e$ and X_e being the largest index, τ_y is the time-shifting with $y = 1, 2, 3, \cdots, Y_e$ and Y_e being the largest index, ν_z is the frequency-shifting with $z = 1, 2, 3, \cdots, Z_e$ and Z_e is the largest index, and $\sigma = (\mathcal{K}_x)^{-1/2}$. The variance scale, time-shift and frequency-shift constitute the three-dimensional grid of Gaussian dictionary and the algorithm flow is shown in

Fig. 3.18. In detail, since the coefficient ρ is the normalization coefficient for the Gaussian atoms, so the

$$\rho = (\int_{-\infty}^{\infty} exp(-\mathcal{K}_x(t-\tau_y)^2)cos(2\pi\nu_z t)dt)^{-1}. \tag{3.3.10}$$

Here, it is assumed that

$$k = 2\pi\nu_z. \tag{3.3.11}$$

And it is defined that

$$I(k) = \int_{-\infty}^{\infty} exp(-\mathcal{K}_x(t-\tau_y)^2)cos(kt)dt. \tag{3.3.12}$$

It is supposed $t - \tau_y = \theta$, then $t = \theta + \tau_y$.

It can be derived that

$$\begin{aligned} I(k) &= \int_{-\infty}^{\infty} exp(-\mathcal{K}_x(\theta)^2)cos(k(\theta+\tau_y))d\theta \\ &= \int_{-\infty}^{\infty} exp(-\mathcal{K}_x(\theta)^2)cos(k\theta)cos(k\tau_y))d\theta \\ &\quad - \int_{-\infty}^{\infty} exp(-\mathcal{K}_x(\theta)^2)sin(k\theta)sin(k\tau_y))d\theta \end{aligned} \tag{3.3.13}$$

Because the formula can be derived as

$$\int_{-\infty}^{\infty} exp(-\mathcal{K}_x(\theta)^2)cos(k\theta)d\theta = (\pi/\mathcal{K}_x)^{1/2}exp(-k^2/4\mathcal{K}_x). \tag{3.3.14}$$

In addition, after the FDR signals are collected, the MPD is used to analyze these signals and extract features.

$$\int_{-\infty}^{\infty} exp(-\mathcal{K}_x(\theta)^2)sin(k\theta)d\theta = (\pi/\mathcal{K}_l)^{1/2}exp(-k^2/4\mathcal{K}_x) \tag{3.3.15}$$

Feature vector $\mathbf{\Phi}_{i,l}^{(m_l)} = \left[\Phi_{i,l,1}^{(m_l)}\ \Phi_{i,l,2}^{(m_l)}\ \Phi_{i,l,3}^{(m_l)}\ \cdots\ \Phi_{i,l,P}^{(m_l)}\right]^T$ is generated by applying MPD on the frequency signal $\mathbf{F}_{i,l}^{(m_l)}$. The pth element $\Phi_{i,l,p}^{(m_l)}$ is defined as $\Phi_{i,l,p}^{(m_l)} = [\alpha_{i,l,p}^{(m_l)} \tau_{i,l,p}^{(m_l)} \nu_{i,l,p}^{(m_l)} \sigma_{i,l,p}^{(m_l)}]^T$, representing the amplitude, time-shifting, frequency-shifting and variance of the Gaussian atom selected by the MPD. Therefore

$$\int_{-\infty}^{\infty} exp(-\mathcal{K}_x(t-\tau_y)^2)cos(2\pi\nu_z t)dt = \tag{3.3.16}$$
$$(\pi/\mathcal{K}_x)^{1/2}e^{-((2\pi\nu_z)^2/4\mathcal{K}_x)}[cos(2\pi\nu_z\tau_y) - sin(2\pi\nu_z\tau_y)]$$

Similarly, $\mathbf{\Theta}_{i,l}^{(m_l)} = \left[\Theta_{i,l,1}^{(m_l)}\ \Theta_{i,l,2}^{(m_l)}\ \Theta_{i,l,3}^{(m_l)}\ \cdots\ \Theta_{i,l,P}^{(m_l)}\right]^T$ denotes the voltage signal feature vector extracted from $\mathbf{V}_{i,l}^{(m_l)}$ by the MPD algorithm.

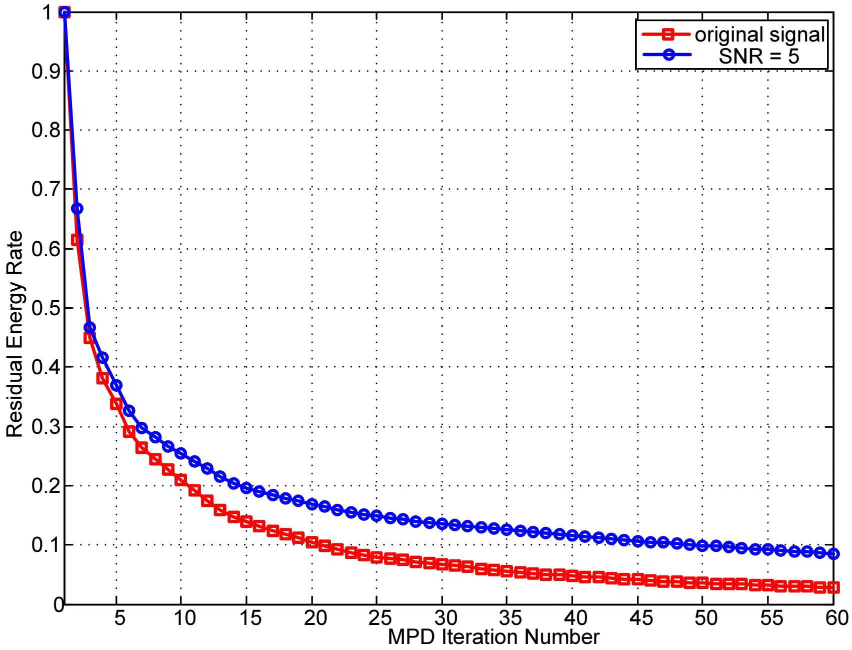

Figure 3.17: Residual energy fraction vs. MPD iterations

As shown in Fig. 3.17, the residual energy is below 30% after 10 iterations for both signals, original signal and noise-distributed signal. After 60 iterations, the residual energy is below 10% for the both signals. In sum, as shown in Fig. 3.16, in the frequency signal processing channel, the transitional properties of the frequency signal features are used to detect and identify different faults. So the MPD in Block 1 for frequency signal feature extraction should extract more detailed information from the original signals.

In our experiments, the iteration number for the frequency signal MPD is set to 30. In the voltage signal processing channel, the Gaussian atom with the maximum coefficient amplitude is defined as the feature Gaussian atom. Meanwhile, the amplitude of the feature Gaussian atom in the voltage signal MPD result is used to represent the impact of the power system fault on the corresponding bus where the voltage signal is collected. And the MPD algorithm is a type of greedy algorithm, the amplitude of the feature Gaussian atom can be computed in the first several iterations [88]. So in this paper, the iteration of the MPD in Block 2 is set to 10 to save the computation load.

Ground fault of load bus

The MPD results corresponding to ground fault of load bus are demonstrated as following. The simulation duration is 500 ms; the ground fault of load bus fault takes place at 200 ms for 10 cycles, about 166.7 ms, at bus 4. The FDR is located at bus 15 with a sampling rate of 1 kHz [137, 141]. In this simulation scenario, it is observed that the frequency keeps unchanged at the beginning, then the frequency fluctuation starts at 230 ms. As the fault location and the FDR location are in different areas, the frequency fluctuation experiences a trough first and then crest to balance the power flow in the system. In order to investigate the feature extraction performance, a white noise is added to the FDR readings, resulting in 5 dB SNR. As shown in Fig. 3.19 and 3.20, the synthesized signal tracks the original signal very well and it can be observed that the original signal curve and synthesized signal curve are almost identical. For the case of noisy signals, although there are a lot of small burrs and spikes in the signal, the synthesized signal is consistent with the

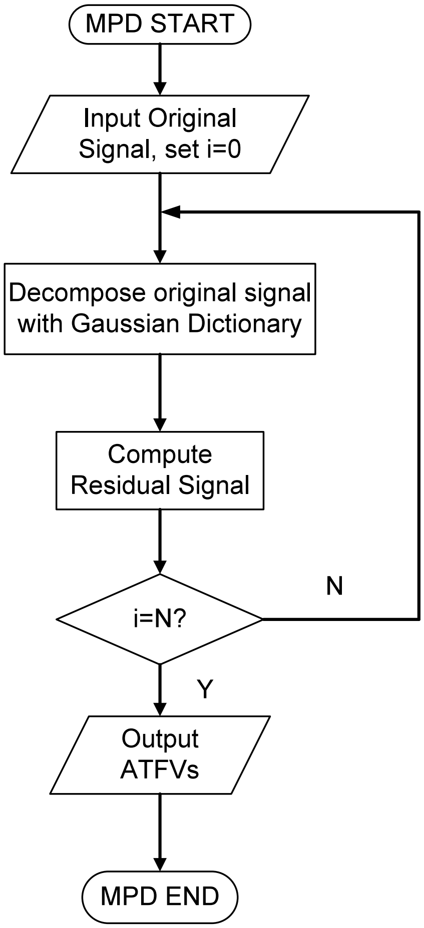

Figure 3.18: The MPD algorithm processing flow.

original signal.

The time-frequency representation (TFRs) of the two signals are shown in Fig. 3.21 and 3.22. From Fig. 3.21, it is noticed that the original signal can be decomposed using a number of Gaussian atoms. The signal in time duration from 200 ms to 300 ms is decomposed by Gaussian atoms with large coefficient amplitude, which indicates a high fluctuation. In Fig. 3.22, in addition to the Gaussian atoms with large coefficient amplitude, a number of atoms with small coefficient amplitude are used to decompose the noisy signal.

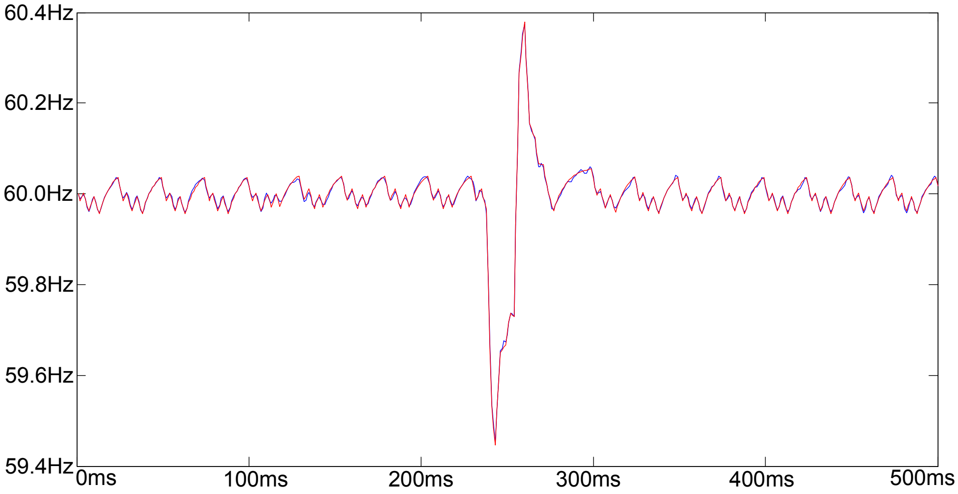

Figure 3.19: The frequency signal without noise and synthesized signal

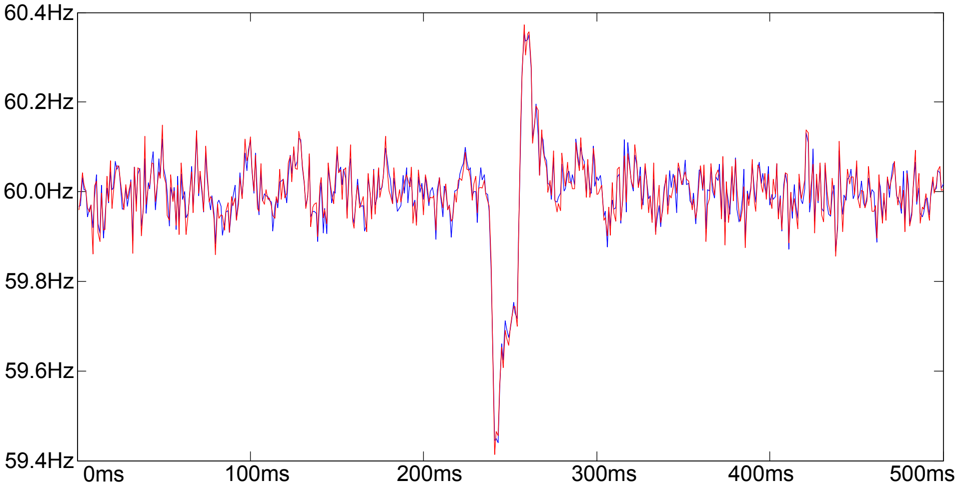

Figure 3.20: The frequency signal with SNR = 5 dB and synthesized signal

Generator disconnection

The figures below demonstrate the MPD results corresponding to a generator disconnection with generator 3 disconnected on bus 32 and the PMU for data acquisition on bus 10. From Fig. 3.23 we notice that there is a significant negative impact of the frequency signal from 200 ms to 230 ms due to a generator disconnection caus-

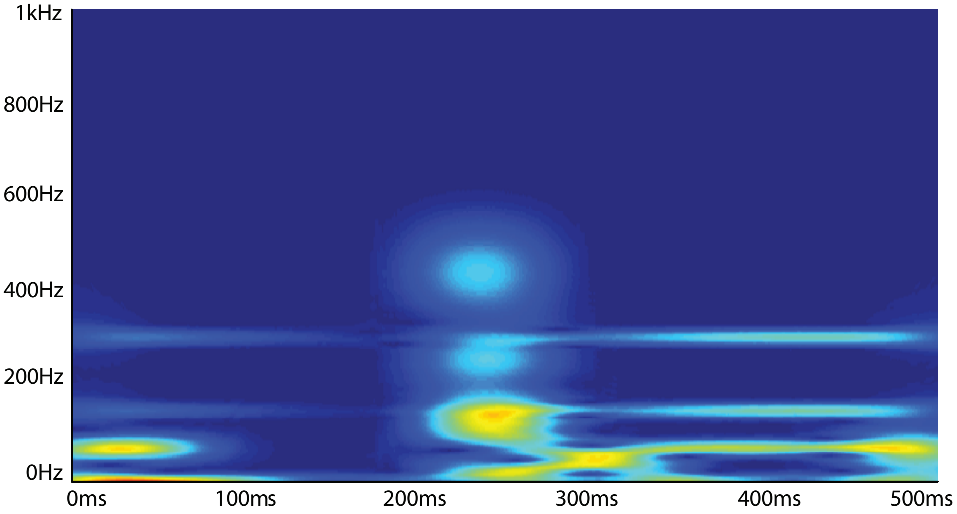

Figure 3.21: The MPD-TFR of 3.19

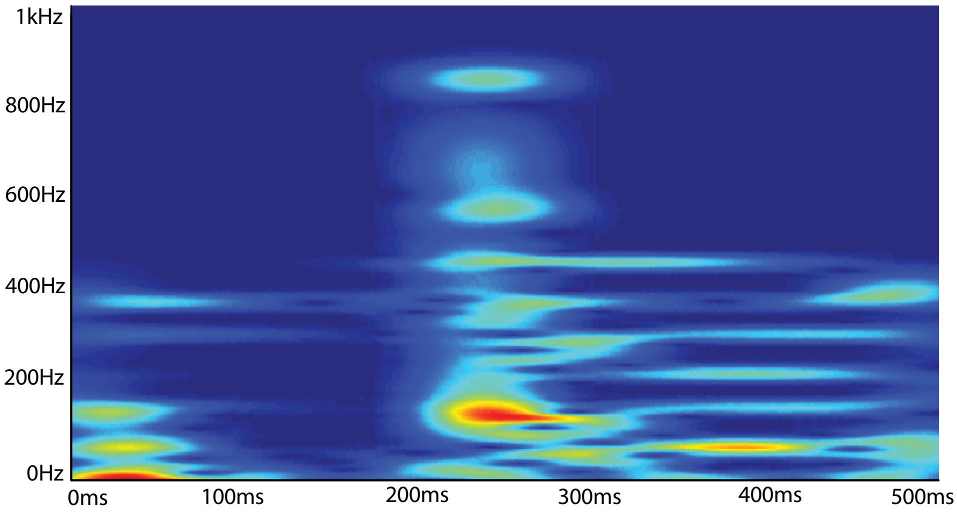

Figure 3.22: The MPD-TFR of 3.20

ing active power lose and resulting in frequency decrease. As other generators in the grid will compensate the active power lose automatically, the frequency fluctuation only lasts 167 ms, and then there is a positive frequency fluctuation from 380 ms to 400 ms. The MPD feature extraction results indicate that the synthesis signal can recover the original signal very well for both noise-free and noisy signal conditions as in Fig. 3.23 and 3.24. According to the TFR shown in Fig. 3.25, the original signal is decomposed into a few number of Gaussian atoms.

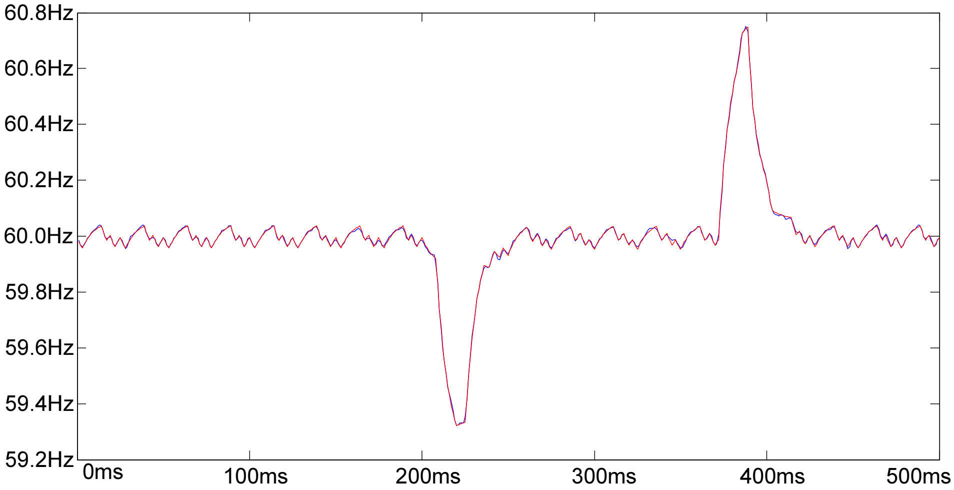

Figure 3.23: The noise-free frequency signal and synthesized signal

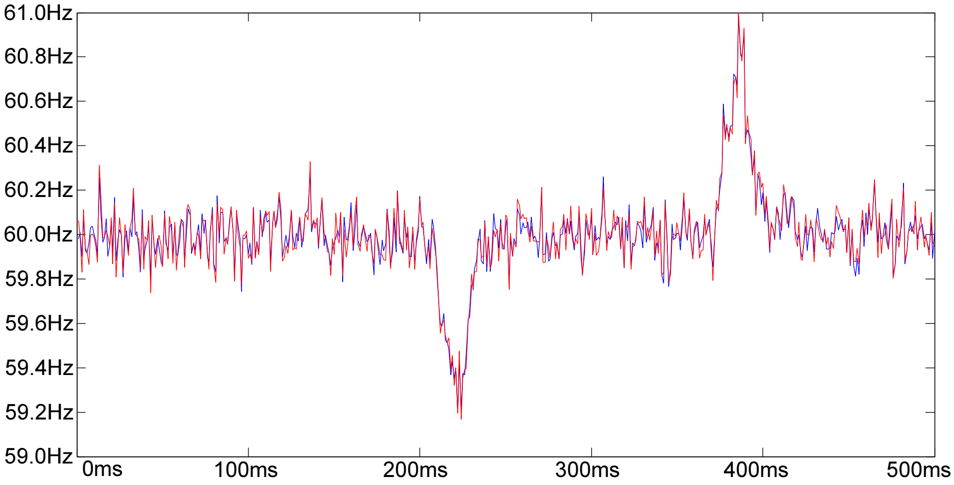

Figure 3.24: The noisy frequency signal with SNR = 5 dB and synthesized signal

Although in Fig. 3.26, the noise-free signal is blurred by the noise, the two major Gaussian atoms, which are the major features of the signal near 200 ms and 400 ms, are extracted similarly to the noisy case. This also illustrates the MPD is able to extract the features in both noise-free and noisy signals. This method can also be used in different power systems.

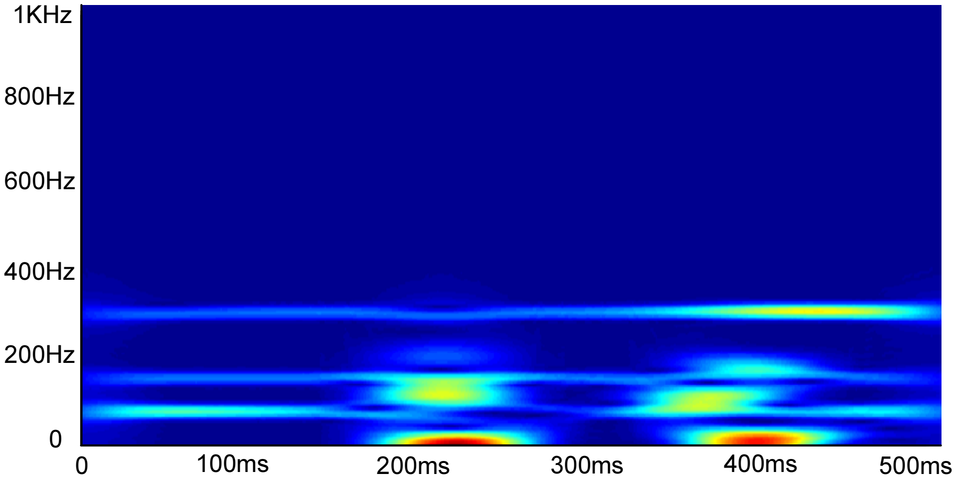

Figure 3.25: The MPD-TFR of 3.23

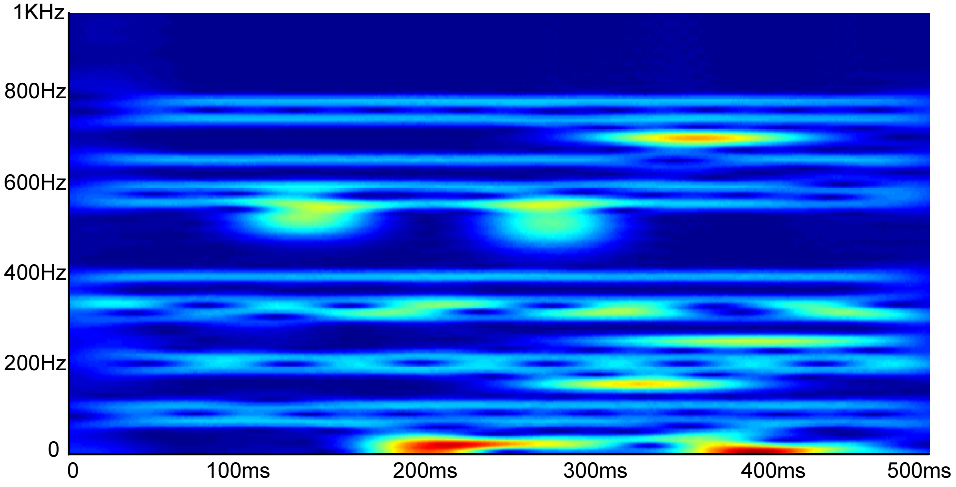

Figure 3.26: The MPD-TFR of 3.24

Load disconnection

We also conduct the experiment of load disconnection. The load disconnection happens on bus 24 and the PMU for data acquisition is also located on bus 24.

There are a positive and then a negative fluctuation in Fig. 3.27 and 3.28 due to the load disconnection which causes the active power to increase in a short time and then the system will balance it automatically.

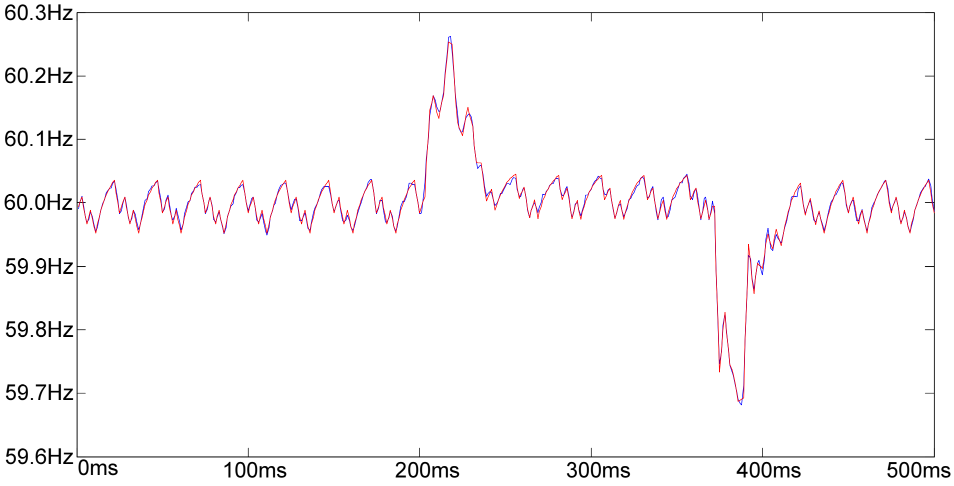

Figure 3.27: The noise-free frequency signal and synthesized signal

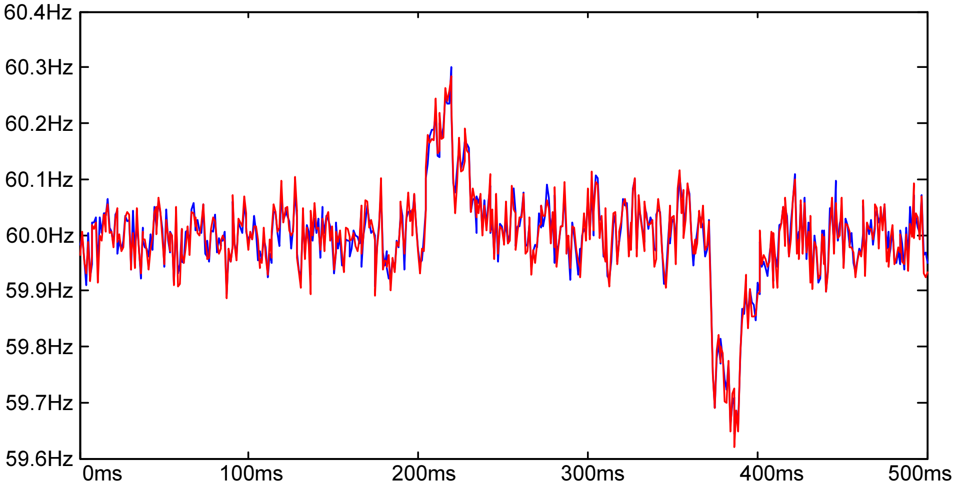

Figure 3.28: The noisy frequency signal with SNR = 5 dB and synthesized signal

The MPD-TFR in Fig. 3.29 illustrates the major Gaussian atoms for decomposing noise-free signal. Although in Fig. 3.30, the signals are blurred by noise, the major Gaussian atoms chosen by MPD below 200 Hz are almost the same as Fig.3.29. The different colors from red to dark indicates the different amplitude of the Gaussian atoms and also indicates the different components of the original signal.

This provides an effective way to analyze the frequency signals in different fault scenarios.

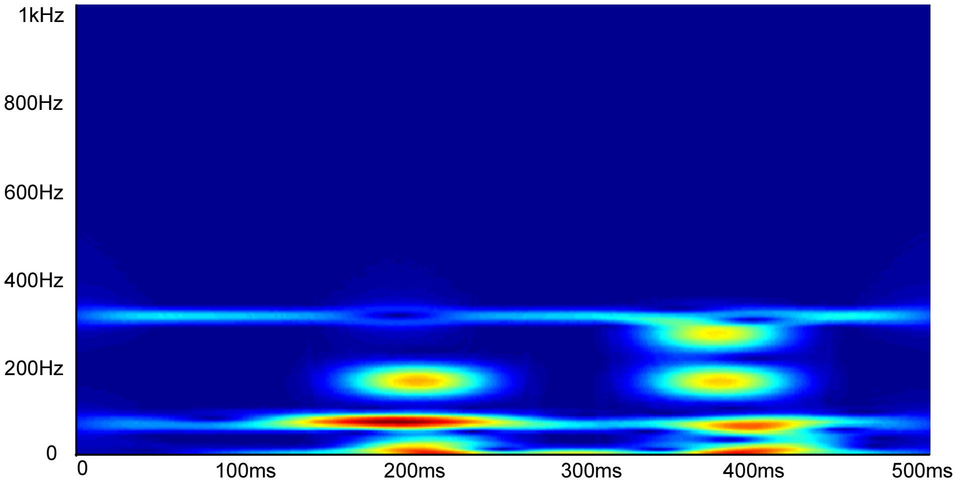

Figure 3.29: The MPD-TFR of 3.27

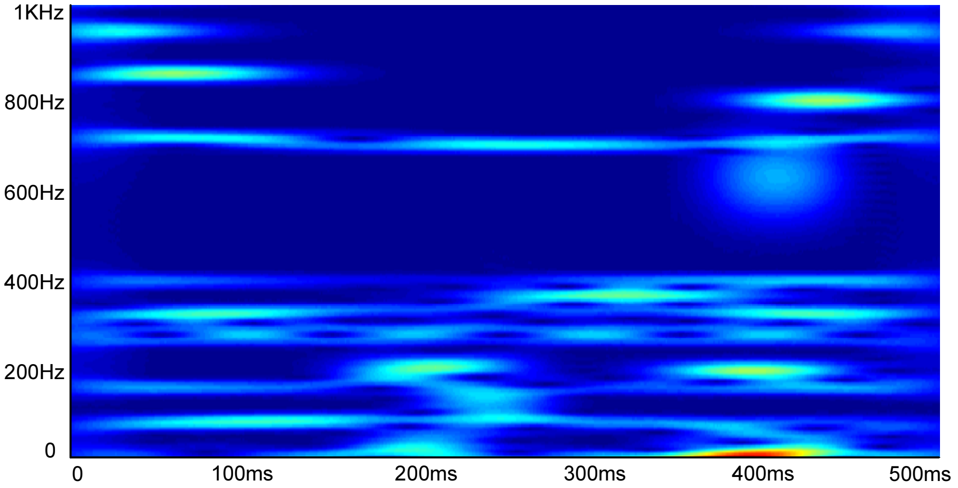

Figure 3.30: The MPD-TFR of 3.28

Generator grounding

We assume a generator grounding fault takes place on bus 35 for generator 6. And the data acquisition PMU is located on bus 22. From Fig. 3.31 and 3.32, we notice that there is a negative impact on the frequency, which is due to the active power loss after the generator grounding.

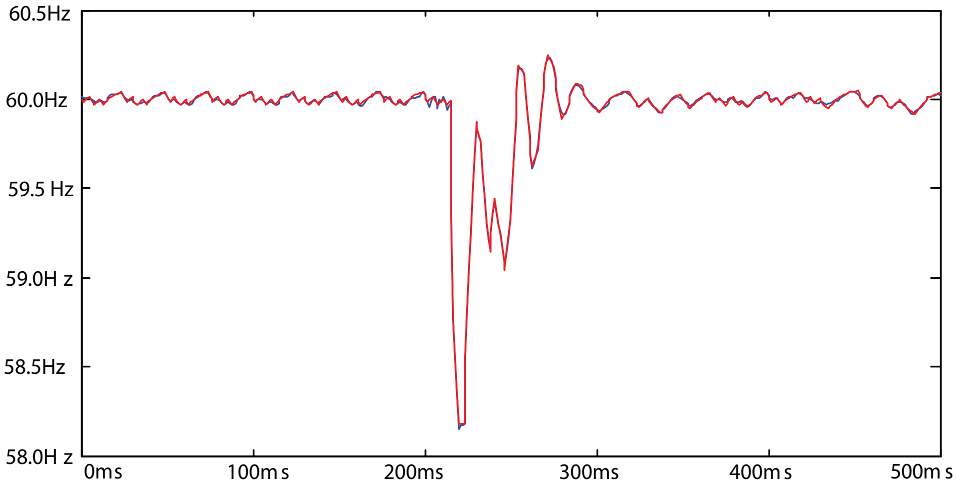

Figure 3.31: The noise-free frequency signal and synthesized signal

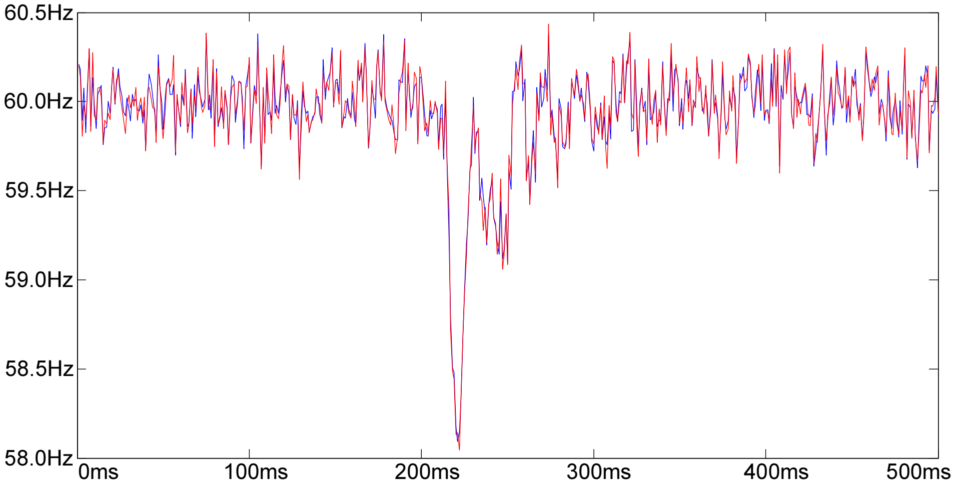

Figure 3.32: The noisy frequency signal with SNR = 5 dB and synthesized signal

In Fig. 3.33 and 3.34, the major Gaussian atoms in both MPD-TFRs, which are below 200 Hz near 200 ms, are almost identical. This indicates that the data features of the generator ground fault are extracted by the MPD for both noise-free and noisy conditions.

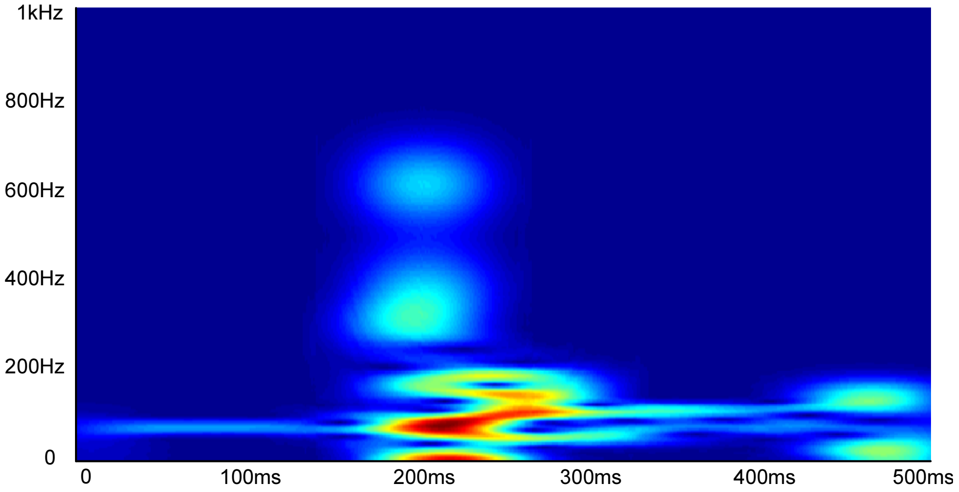

Figure 3.33: The MPD-TFR of 3.31

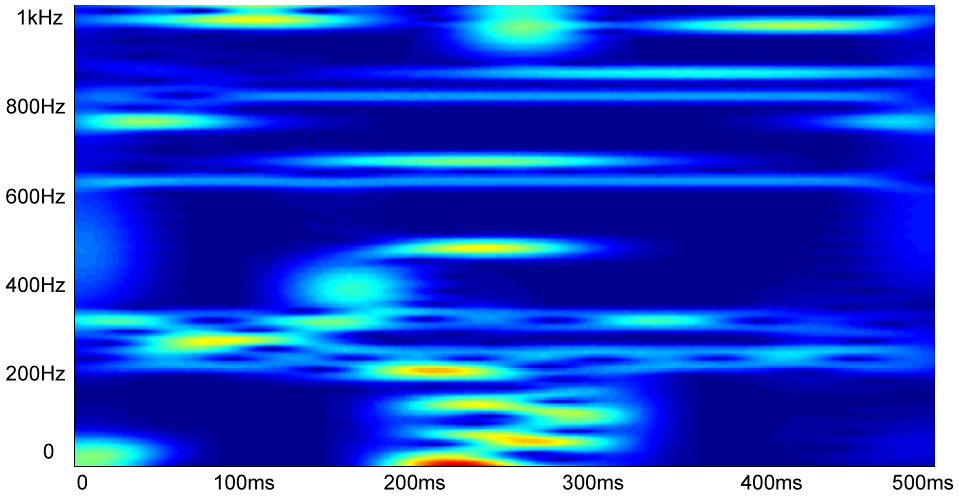

Figure 3.34: The MPD-TFR of 3.32

3.3.3 Hybrid clustering algorithm design

After the feature vectors are extracted from the FDR signals, the frequency signal feature vectors $\Phi_{i,l,p}^{(m_l)} = [\alpha_{i,l,p}^{(m_l)} \tau_{i,l,p}^{(m_l)} \nu_{i,l,p}^{(m_l)} \sigma_{i,l,p}^{(m_l)}]^T$ in the set $\boldsymbol{\Phi}_{i,l}^{(m_l)}$ are clustered into different subsets, and the voltage signals $\boldsymbol{\Theta}_{i,l}^{(m_l)}$ are also going to be clustered in a similar way. Combining the k-means clustering algorithm with the k-nearest neighbour (k-NN) algorithm, a novel hybrid algorithm is proposed for clustering the feature vectors with reduced computational load.

k-NN and k-means clustering algorithms

The k-NN algorithm can be summarized as following. First, a data set is given, which is pre-clustered into a number of groups. With a new-coming data point ξ_p, k data points in the data set are selected, which are the nearest neighbors to the new-coming data point ξ_p. The group which contains the most of these neighbors is the one that the new-coming data point ξ_p belongs to [35, 85].

For example, when a new-coming data point ξ_{18} is generate from the signals collected on Bus 18. ξ_{18} need to be classified among the 5 impact level groups $\{\mathit{\Omega}_1, \mathit{\Omega}_2, \cdots \mathit{\Omega}_5\}$. If k-NN algorithm is used, k nearest neighbors of ξ_{18} will be selected from the 5 groups. And the new-coming data point ξ_{18} will be assigned to into the group, which contains the most of the nearest neighbors.

k-means is an algorithm which uses an iterative refinement technique. Firstly, an initial set of k means $\{\eta_1, \eta_2, \eta_3, \cdots, \eta_k\}$ of k corresponding clusters is given. Then, each observation in the observation set $\{\xi_p, p = 1, 2, 3, \cdots, N\}$ is assigned to the cluster which yields the least distance between its mean to the observation among all clusters as following.

$$\mathit{\Omega}_i^{(t)} = \{\xi_p : \boldsymbol{d}(\xi_p, \eta_i^{(t)}) \leq \boldsymbol{d}(\xi_p, \eta_j^{(t)}) \ \forall j, 1 \leq j \leq k\} \tag{3.3.17}$$

where t is the iteration number, $p = 1, 2, 3, ..., N$, N is the size of the observation data set and $\mathbf{d}(\cdot)$ represents the distance function. The new means of each cluster is updated as in (7) and the data set is re-clustered until the means converge[86, 85].

$$\eta_i^{(t+1)} = \frac{1}{|\Omega_i^{(t)}|} \sum_{\xi_j \in \Omega_i^{(t)}} \xi_j \tag{3.3.18}$$

For example, when a new-coming data set $\{\xi_1, \xi_2, \xi_3, \cdots, \xi_N\}$ is generated from the SG and need to be classified into 5 groups, an initial set of 5 means is generated. Then, as in (6), the set is clustered with k-means algorithm iteratively until the means converge.

Compared with the k-NN algorithm, the k-means algorithm calculates the mean value η_i for different clustering hypotheses at every iteration. As a result, the computational complexity of the k-NN algorithm, $O(k \times N \times d)$, is much lower with respect to that of the k-means algorithm, $O(N \times k \times I \times d)$, where N is the number of observations; k is the number of clusters; I is the number of iterations; and d is the dimensions of the observation [37, 85, 86].

The hybrid clustering algorithm

In this section, our proposed hybrid clustering algorithm is explained based on the k-NN algorithm and k-means algorithm. The Euclidean distance $\mathbf{d}(\cdot)$ is used for the algorithm.

The proposed hybrid clustering algorithm is expected to provide reduced computational complexity and aims to enable real-time data processing for signal feature clustering. In the frequency signal processing channel, the hybrid clustering is used to cluster the frequency features and map them into a symbol set. In the voltage signal processing channel, the hybrid clustering is used to cluster the coefficient amplitudes of the feature Gaussian atoms. The two clustering blocks in Fig. 3.16

work independently with a similar processing architecture, which is illustrated in Fig. 3.35. The proposed hybrid clustering algorithm is explained as following using the frequency signal feature clustering as an example. After the FDR signals are processed by the MPD, the feature vector set $\left\{\Phi_{i,l,p}^{(m_l)}\right\}$ is generated and ready for clustering.

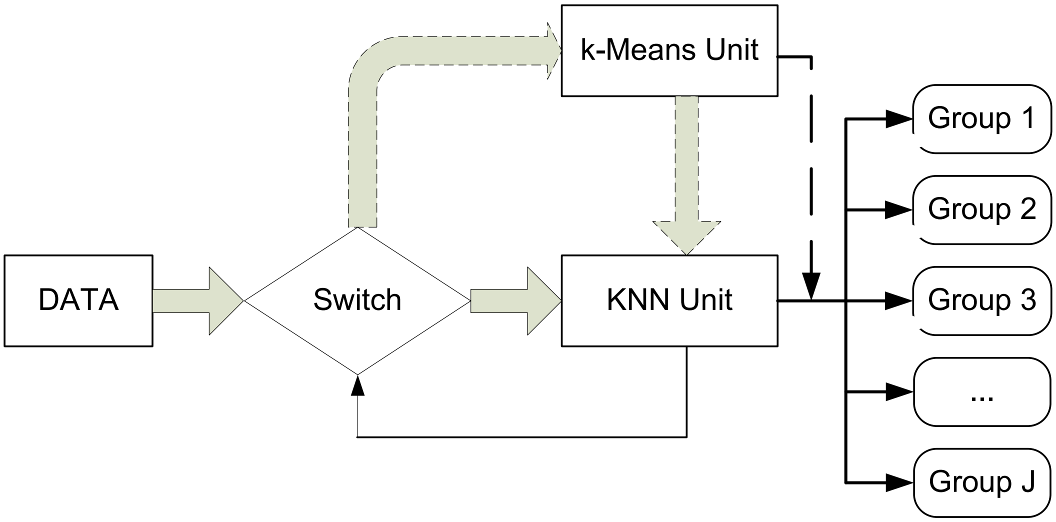

Figure 3.35: Architecture of the hybrid clustering algorithm.

As shown in Fig. 3.35, firstly, only part of the feature vector set $\left\{\Phi_{i,l,p}^{(m_l)}\right\}$ is fed to k-means algorithm. The k-means algorithm clusters the data set $\left\{\Phi_{i,l,p}^{(m_l)}\right\}$ into several subsets $\{\Omega_{g,l}^{(m_l)}\}$, where g is the subset index. After the clusters are generated, the data are clustered by the k-NN algorithm, which uses the generated subsets $\{\Omega_{g,l}^{(m_l)}\}$ for clustering the rest of the feature vectors in set $\left\{\Phi_{i,l,p}^{(m_l)}\right\}$. The number of feature vectors that are used for generating $\{\Omega_{g,l}^{(m_l)}\}$ depends on whether the k-means can generate satisfactory clustering result. For example, in a training process of our experiments, 1200 out of 8000 feature vectors are used for k-means algorithm, and the rest of the data are clustered by k-NN, which saves a large amount of computational loads. In addition, the hybrid clustering in the voltage signal processing channel works similarly and clusters the coefficients of the feature

Gaussian atoms into several groups for generating the fault contour maps. This provides an effective way to reduce the computation load and increase the clustering speed.

3.3.4 Hidden Markov models for fault detection and identification

The feature symbols $\{\boldsymbol{\beta}_{i,l,p}^{(m_l)}\}$ are used as the observation symbol to train different HMMs for detecting and identifying faults. As Fig. 3.16 illustrates, two HMMs, Λ^0 and $\boldsymbol{\Lambda}^{\phi}$ are trained and used to detect faults and distinguish between the normal condition and abnormal conditions of the SG. Also for each fault type, a HMM, $\Lambda^{(m)}$, is trained to identify the m_lth fault type after the fault occurs.

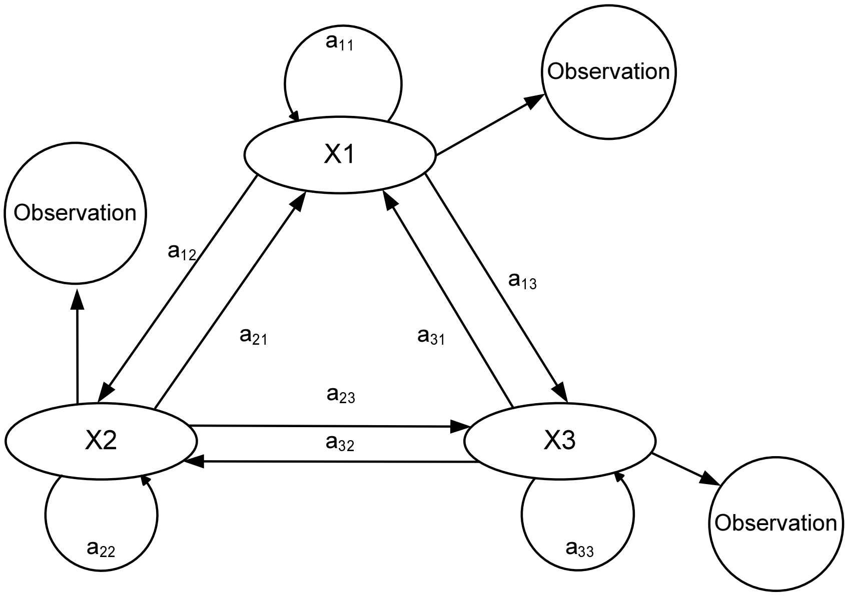

Figure 3.36: Architecture of an HMM with 3 hidden states.

In $\Lambda^{(m)}$, the parameters $\lambda^{(m)}=\{\pi^{(m)}, A^{(m)}, B^{(m)}\}$ represent the initial states distribution vector, the hidden state transition matrix, and the state-dependent observation density matrix, respectively [107, 106]. The example of a 3-states HMM is in Fig. 3.36 where a_{ij} is the transition probability between state i to j. The HMM

Λ^0 and $\mathbf{\Lambda}^{\phi}$ for the SG in normal and abnormal operating condition is trained with the frequency signals.

Using the Baum-Welch algorithm [107, 27], the maximum-likelihood estimate for λ is given by:

$$\lambda_{ML} = \arg\max_{\lambda} \log P(\boldsymbol{\beta}|\lambda, \Lambda)\,, \tag{3.3.19}$$

where $\boldsymbol{\beta}$ is the observation data; λ is the parameter set of the HMM Λ. And at the ith iteration:

$$\lambda^{(i+1)} = \underset{\lambda}{\operatorname{argmax}} \sum_{\mathbf{H}} P(\mathbf{H}|\boldsymbol{\beta}, \lambda, \Lambda) \log P(\mathbf{H}, \boldsymbol{\beta}|\lambda^{(i)}, \Lambda)\,, \tag{3.3.20}$$

where $\mathbf{H}$ is the hidden states and the sum is the overall possible state sequences in the hidden Markov model.

The probability of $P(\boldsymbol{\beta}|\lambda, \Lambda)$ is calculated as

$$\begin{aligned} P(\boldsymbol{\beta}|\lambda, \Lambda) &= \sum_{\mathbf{H}} P(\mathbf{H}, \boldsymbol{\beta}|\lambda, \Lambda) \\ &= \sum_{\mathbf{H}} \pi_{H_1} \prod_{n=1}^{N_{A_{obs}}} a_{H_n, H_{n+1}} \prod_{n=1}^{N_{A_{obs}}} b_{H_n}(\beta_n)\,, \end{aligned} \tag{3.3.21}$$

where π_{H_1} is the initial state probability of state H_1, $a_{H_n,H_{n+1}}$ is the state transition probability from state H_n to H_{n+1}, and $b_{H_n}(\beta_n)$ is the probability from observation β_n to state b_{H_n}.

The application of the CHMMs is also investigated, which uses Gaussian mixture models (GMM) with M_G components to model the observation probability given by a certain state[106, 107, 27], which is given by

$$b_j(\beta) = \sum_{k=1}^{M_G} p_{jk} \mathcal{N}(\beta; \mu_{jk}, \sigma_{jk})\,, 1 \le j \le A_{obs}, \tag{3.3.22}$$

where $\mathcal{N}(\cdot)$ denotes the Gaussian distribution, p_{kj} is the GMM coefficient with $\sum_{k=1}^{M_G} p_{jk}$=1, $p_{jk} \geq 0$, μ_{jk} is the mean value of the kth component and σ_{jk} is the corresponding covariance for the Gaussian components.

The HMM procedure in the scenario of a generator ground fault is investigated in the IEEE 39-bus system. The training data set are generated with random fault in generators 3, 4, 5, 6, 7, 9. A_{obs} is set to 32 and 3 hidden states are used to calculate the parameters of the DHMM for generator ground fault.

$$\pi = \{0.2899, 0.2808, 0.4293\},$$

$$A = \begin{bmatrix} 0.7512 & 0.2483 & 5.8712 \times 10^{-4} \\ 0.7195 & 0.2788 & 0.0017 \\ 0.3151 & 0.3192 & 0.3657 \end{bmatrix},$$

where π is the initial probability distribution of the three hidden states; $A = [a_{ij}]$ is the hidden state transfer matrix, while a_{ij} is the probability from hidden state i to hidden state j. And $B = [b_{ij}]$ is a 3×32 matrix, where b_{ij} is the emission probability from hidden state i to observation j [107].

We also investigate the application of the continuous HMMs, which uses Gaussian mixture models (GMM) with M_G components to model the observation probability given by a certain state[1, 107, 27], which is given by

$$b_j(\beta) = \sum_{k=1}^{M_G} p_{jk} \mathcal{N}(\beta; \mu_{jk}, \Sigma_{jk}), 1 \leq j \leq A_{obs}, \qquad (3.3.23)$$

where $\mathcal{N}(\cdot)$ denotes the Gaussian distribution, p_{kj} is the GMM coefficient with $\sum_{k=1}^{M_G} p_{jk}$=1, $p_{jk} \geq 0$, μ_{jk} is the mean value of the kth component and Σ_{jk} is the corresponding covariance for the Gaussian components.

The continuous HMM training results are demonstrated as below, we use $M_G = 6$ components for each observation pdf, and we treat the feature symbol as continuous values. We calculate the mean and the covariance of the Gaussian components as following,

$$\mu = \begin{bmatrix} 19.567 & 12.000 & 17.461 & 30.855 & 23.000 & 22.000 \\ 1.2772 & 21.000 & 7.5131 & 5.2861 & 3.0751 & 14.000 \\ 24.513 & 11.000 & 13.000 & 15.310 & 9.8515 & 27.027 \end{bmatrix},$$

$$\Sigma = \begin{bmatrix} 0.2456 & 1.0000 & 0.2485 & 1.3349 & 1.0000 & 1.0000 \\ 0.2004 & 1.0000 & 0.2498 & 0.2042 & 0.0696 & 1.0000 \\ 0.2498 & 1.0000 & 1.0000 & 0.2140 & 0.1265 & 0.5963 \end{bmatrix},$$

where μ_{ij}, the (i, j)th element of μ denotes the mean value of the jth Gaussian component of the ith state for the generator grounding fault, and Σ_{ij} denotes the corresponding covariance. Following a similar procedure, for different abnormally scenarios, different HMMs are trained.

Base on the HMM method, the fault detection and identification is carried out as follows. First, we model the normal operation HMMs Λ^0 for SG in normal conditions. Also we build different HMMs corresponding to the different kinds of faults: $m_l = 1$ for generator grounding, $m_l = 2$ for load grounding, $m_l = 3$ for generator disconnection , and $m_l = 4$ for load disconnection.

After all the HMMs are built, they are used to detect and classify faults. First the HMM Λ^0 will be used to determine if the SG is operating normally. If a fault is detected, the fault contour map will be generated. Four different HMMs, $\Lambda^{(m_l)}$, $m_l = 1, 2, 3, 4$ are used to identify the fault type. We use the confusion matrices to demonstrate the performance of the algorithm in the next section.

3.3.5 Fault contour map for fault location

In addition to fault detection and identification, as shown in Fig. 3.16, the fault location can also be inferred from power system signals. In the voltage signal processing channel, the coefficient amplitude of the feature Gaussian atom in the MPD results is used to represent the impact of the power system fault on the corresponding bus where the signal is recorded. The 39 buses are classified into several different impact levels by the clustering algorithm. Combined with the topology information of the SG, the fault contour map can be generated and the fault can be located.

The fault location approach is demonstrated as following using the same example of ground fault of load bus as before. In the voltage signal processing channel, the clustering algorithm is used to cluster the coefficients of feature Gaussian atoms and the corresponding 39 buses into 5 different impact levels as shown in Table 3.2. Combined with the topology information of the IEEE 39 bus system, it is noticed that bus 4 has the greatest amplitude of the feature Gaussian atom. In Table 3.2, bus 4 belongs to the 1st level, which also illustrates the probable location of the fault. Level 2 to 5 indicate different impact levels, which also implies electrical distance. The impact on bus 12 is small in level 5, because there is a transformer linking the high voltage buses 11, 13 and the low voltage bus 12. Combined with the topology information of the smart grid with Table 3.2, the fault contour map can be generated as in Fig. 3.37, which can be used to locate the fault and indicate different impact areas of the fault. For another example, if there is a transmission line outage at 15% distance between bus 4 and bus 14, this method can locate the fault between these two buses and indicate that the outage is near bus 4 for it has the greatest amplitude of the feature Gaussian atom.

Table 3.2: Impact level of ground fault of load bus

Impact level	Bus number
1st (nearest to fault)	4
2nd	3,5,6,7,11,13,14,15,18
3rd	2,8,9,10,16,17,21,24,26,27
4th	1,19,22,23,25,28
5th	12,20,29,30,31,32,33,34,35,36,37,38,39

3.4 Wide area monitoring with optimal synchrophasor sensor placement

Early work on the optimal PMU placement (OPP) problem was investigated based on generalized integer linear programming (ILP) formulation [50]. Contingency conditions of line outage or PMU loss are considered with OPP in [3]. In this paper, aiming to provide the full network observability, an optimal synchrophasor sensor placement (OSSP) approach is investigated to determine the minimal number and optimal location of synchrophasor sensors.

3.4.1 Optimal synchrophasor sensor placement

The objectives of OSSP are to minimize the number of synchrophasor sensors, while to maximize the measurement redundancy for ensuring full system observability. In this section, the concept of topological observability is adopted and the following rules are applied [58] for OSSP.

- If the voltage phasor and current phasor at one end of a branch are known, the voltage phasor at other end of that branch can be obtained using Ohm's law.
- If the voltage phasors at both ends of a branch are known, the current phasor through this branch can be calculated.

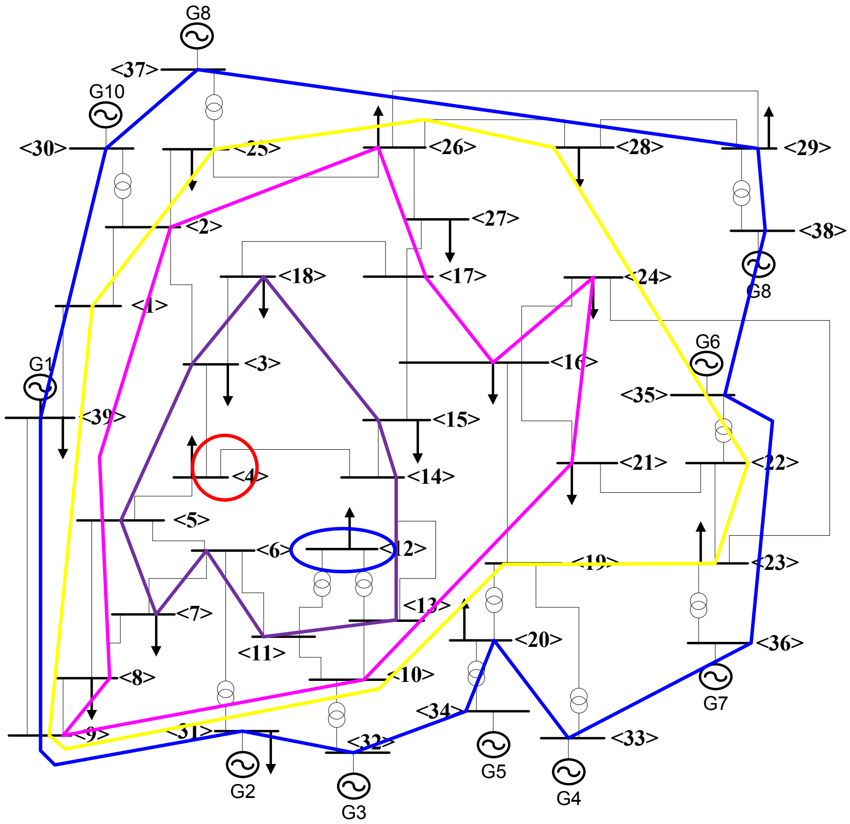

Figure 3.37: The fault contour map for ground load at bus 4.

The measurements such as bus voltage phasors and branch current phasors, directly obtained from the synchrophasor sensors, are referred to as direct measurements. Measurements derived by employing the above two rules are referred to as indirect measurements, or pseudo measurements. In an observable network, each and every bus must be observed at least once by using direct or indirect measurement.

The OSSP placement at a bus can be seen as a binary decision variable defined as

$$u_i = \begin{cases} 1 & \text{if synchrophasor sensor is placed at bus } i \\ 0 & \text{otherwise} \end{cases} \tag{3.4.1}$$

For a system with n buses, the optimal sensor placement problem can be formulated as an integer linear programming problem as follows,

$$\min F = \sum_{i=1}^{n} c_i u_i$$

subject to constraints: $f_i = \sum_{j=1}^{n} a_{i,j} u_j \ \geq 1, \ i = 1, 2, 3, ..., n$, where c_i is the cost of installing a synchrophasor sensor at bus i. The cost of synchrophasor sensor installation at each bus is assumed to be equal to 1 per unit in the present study. f_i refers to the number of times that the ith bus is observed through synchrophasor measurements. $a_{i,j}$ is the (i, j)th entry of system connectivity matrix defined as

$$a_{i,j} = \begin{cases} 1 & \text{if } i = j \text{ or if } i \text{ and } j \text{ are connected} \\ 0 & \text{otherwise} \end{cases} \tag{3.4.2}$$

OSSP considering the effect of zero-injection buses

If the effect of ZIBs is considered, the total number of synchrophasor sensors in OSSP problem will be futher reduced due to the following rules

- In a zero injection cluster (ZIC), if the zero-injection bus is observable and its adjacent buses are all observable except one, then the unobservable bus will be identified as observable by applying Kirchhoff's Current Law (KCL) at ZIB.
- In a ZIC, if all the buses are observable except the zero-injection one, then the zero-injection bus can be also identified as observable by using nodal equations.

Combining these two cases can lead to the conclusion that a ZIC is observable when it has at most one unobservable bus.

OSSP considering single sensor outage

Outage of a sensor at bus h, can be considered into the previous OSSP by setting the corresponding decision variable u_h to zero. To facilitate the formulation of the optimization problem, a parameter, $p_{i,j}$ is defined as follows:

$$p_{i,j} = \begin{cases} 0 & \text{if } h{=}j \\ 1 & \text{otherwise} \end{cases} \tag{3.4.3}$$

then, the associated constraints to OSSP problem considering single sensor outage are as

$$f_i = \sum_{j=1}^{n} p_{i,j} a_{i,j} u_j \geq 1, \ \forall i, \forall h \tag{3.4.4}$$

OSSP considering single line outage

Outage of a line may cause loss of observability for one of its terminal buses, which would otherwise be observable using the current phasor of that line. For a power network with M lines, M single line contingencies can be defined. Thus the constraints of single line outage can be presented as:

$$f_i = \sum_{j=1}^{n} a^l_{i,j} u_j \ \geq 1, \ \forall i, \forall l, \tag{3.4.5}$$

where the parameter $a^l_{i,j} = 0$ if the lth line connects buses i and j, and $a^l_{i,j} = a_{i,j}$ otherwise.

In summary, combining the aforementioned constraints corresponding to different scenarios, the OSSP problem can be formulated and solved for full spatial characterization of synchrophasor measurements in a SG.

3.4.2 Numerical result of IEEE 14-bus system

The IEEE 14-bus system is used as a test bench for investigating our proposed OSSP problem. From the computed resulted of OSSP shown in Table 3.3, without considering ZIB, only 4 sensors are required to observe the whole power system. If considering ZIB, only 3 sensors are required. However, if considering single line outage and single sensor outage, 9 and 10 sensors are needed, respectively. Considering both single line outage and single sensor outage, 11 sensors are needed. The effect of ZIB is considered in the simulations in the scenarios of single line outage, single sensor outage, and single sensor/line outage.

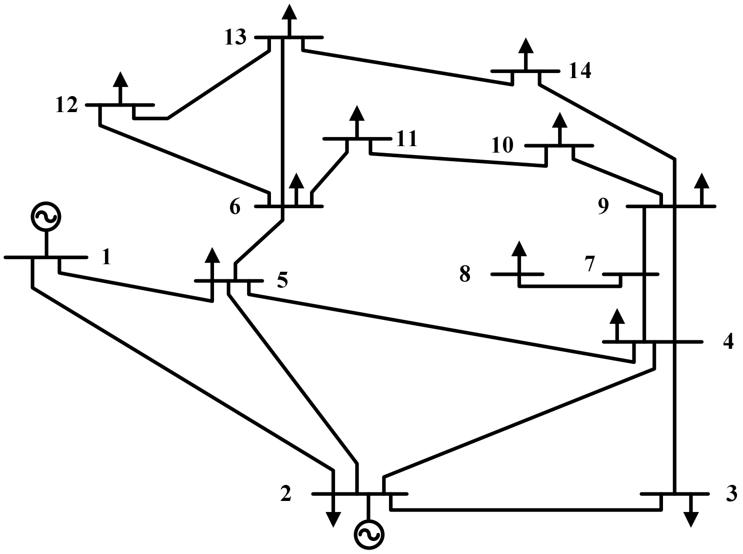

Figure 3.38: The IEEE 14 bus system.

Table 3.3: Comparison of OSSP results in IEEE 14-bus system

Scenario Type	Number	Location of Sensors	Rate
Ignoring the effect of ZIB	4	1-2, 4, 6, 8, 10-11, 13-14	28.6
Considering the effect of ZIB	3	2, 6, 9	21.4
Single Line Outage	9	1-2, 4, 6, 8, 10-11, 13-14	64.3
Single Sensor Outage	10	1-2, 4-6, 9-11, 13-14	71.4
Single Sensor/Line Outage	11	1-2, 4-6, 8-11, 13-14	78.6

3.5 A fast voltage security assessment approach for a wind power plant

With the increasing technology of wind turbines, the penetration level of wind power is rising and wind power has become competitive with other types of generation. Because of the low penetration levels of wind power during the early decades, the loss of a wind power plant was not considered a critical threat to power system security. During these decades, when a fault caused the voltage deviation at the interconnection bus of a wind power plant, the wind power plant was disconnected and reconnected when the fault was cleared and the voltage returned to normal [98, 63, 62]. In the modern power systems, because the size of wind power plant have increased (up to 1,000 MW), wind power is an indispensable resource in generation, and the simple disconnection-reconnection approach cannot be adopted for voltage deviation scenarios. Therefore, it is imperative to develop an effective and efficient voltage assessment approach to enhance voltage security for wind power plants.

3.5.1 Admittance matrix based voltage security assessment

As discussed above, a fast voltage security assessment approach is proposed in this paper for power systems that have a wind power plant. The objective of voltage security assessment is to identify system locations that will have the greatest impact on the voltage at the wind power plant's point of interconnection.

Considering that a three-phase symmetrical fault on a bus causes the highest fault current, it is necessary to study it to better protect the wind power plant in the system. Thus, this paper studies the three-phase symmetrical fault to illustrate the proposed approach. It is assumed that the PMUs are located on all the buses in the power system. Traditionally, the element $[Y_{i,j}]$ in admittance matrix $\mathbf{Y}$ indicates the admittance between bus i and bus j [98]. In this paper, the impedance matrix is calculated by the inverse of the admittance matrix $\mathbf{Y}$; then the information on the impact is generated, which indicates the changes in current injection at one bus have on the others.

Because there is a wind power plant in the power system, this approach can be used to generate for the critical bus set $\mathbf{B}$, which has the greatest impact on the voltage stability at the wind power plant's point of interconnection. It's also provides an effective way to study the robustness and resilience of a power system under a short-circuit current injection. The impedance equivalent matrix can be expressed as

$$Z = \begin{bmatrix} Z_{11} & \cdots & Z_{1i} & \cdots & Z_{1n} \\ \cdots & \cdots & \cdots & \cdots & \cdots \\ Z_{i1} & \cdots & Z_{ii} & \cdots & Z_{in} \\ \cdots & \cdots & \cdots & \cdots & \cdots \\ Z_{n1} & \cdots & Z_{ni} & \cdots & Z_{nn} \end{bmatrix},$$

It is assumed that the three-phase symmetrical fault occurs at bus i and the wind power plant is connected at bus j. The short-circuit current at bus i can be calculated as

$$I_i^{SC} = V_i^0 / Z_{ii}, \tag{3.5.1}$$

where:

V_i^0 is the bus voltage pre-fault condition measured by PMUs

Z_{ii} is the Thevenin equivalent impedance of bus i

I_i^{SC} is the short-circuit current at bus i.

Table 3.4: The impedance matrix of IEEE 14-bus system

Bus No.	*1*	*2*	*3*	*4*	*5*	*6*	*7*
1	-0.26 - 2.22i	-0.27 - 2.26i	-0.28 - 2.28i	-0.28 - 2.29i	-0.28 - 2.28i	-0.29 - 2.45i	-0.29 - 2.41i
2	-0.27 - 2.26i	-0.27 - 2.25i	-0.28 - 2.28i	-0.28 - 2.29i	-0.28 - 2.28i	-0.29 - 2.45i	-0.29 - 2.41i
3	-0.28 - 2.28i	-0.28 - 2.28i	-0.25 - 2.19i	-0.28 - 2.29i	-0.28 - 2.29i	-0.29 - 2.45i	-0.29 - 2.41i
4	-0.28 - 2.29i	-0.28 - 2.29i	-0.28 - 2.29i	-0.28 - 2.27i	-0.28 - 2.28i	-0.29 - 2.44i	-0.29 - 2.39i
5	-0.28 - 2.28i	-0.28 - 2.28i	-0.28 - 2.29i	-0.28 - 2.28i	-0.27 - 2.25i	-0.28 - 2.42i	-0.29 - 2.39i
6	-0.29 - 2.45i	-0.29 - 2.45i	-0.29 - 2.45i	-0.29 - 2.44i	-0.28 - 2.42i	-0.28 - 2.43i	-0.31 - 2.52i
7	-0.30 - 2.41i	-0.30 - 2.41i	-0.29 - 2.41i	-0.29 - 2.39i	-0.29 - 2.40i	-0.31 - 2.52i	-0.30 - 2.38i
8	-0.30 - 2.41i	-0.30 - 2.41i	-0.29 - 2.41i	-0.29 - 2.39i	-0.29 - 2.40i	-0.31 - 2.52i	-0.30 - 2.38i
9	-0.30 - 2.45i	-0.30 - 2.45i	-0.30 - 2.45i	-0.29 - 2.43i	-0.29 - 2.43i	-0.32 - 2.53i	-0.30 - 2.46i
10	-0.30 - 2.45i	-0.30 - 2.45i	-0.30 - 2.44i	-0.29 - 2.43i	-0.29 - 2.43i	-0.31 - 2.51i	-0.30 - 2.47i
11	-0.29 - 2.44i	-0.29 - 2.44i	-0.29 - 2.44i	-0.29 - 2.43i	-0.28 - 2.42i	-0.29 - 2.47i	-0.30 - 2.49i
12	-0.28 - 2.45i	-0.28 - 2.45i	-0.29 - 2.45i	-0.28 - 2.44i	-0.28 - 2.42i	-0.27 - 2.44i	-0.30 - 2.52i
13	-0.29 - 2.45i	-0.29 - 2.45i	-0.29 - 2.45i	-0.28 - 2.44i	-0.28 - 2.42i	-0.28 - 2.44i	-0.30 - 2.51i
14	-0.29 - 2.45i	-0.29 - 2.45i	-0.29 - 2.45i	-0.29 - 2.43i	-0.29 - 2.43i	-0.30 - 2.49i	-0.30 - 2.48i

Bus No.	*8*	*9*	*10*	*11*	*12*	*13*	*14*
1	-0.26 - 2.22i	-0.27 - 2.26i	-0.28 - 2.28i	-0.28 - 2.29i	-0.28 - 2.28i	-0.29 - 2.45i	-0.30 - 2.41i
2	-0.27 - 2.26i	-0.27 - 2.25i	-0.28 - 2.28i	-0.28 - 2.29i	-0.28 - 2.28i	-0.29 - 2.45i	-0.30 - 2.41i
3	-0.28 - 2.28i	-0.28 - 2.28i	-0.25 - 2.20i	-0.28 - 2.29i	-0.28 - 2.29i	-0.29 - 2.45i	-0.29 - 2.41i
4	-0.28 - 2.29i	-0.28 - 2.29i	-0.28 - 2.29i	-0.28 - 2.27i	-0.28 - 2.28i	-0.29 - 2.44i	-0.29 - 2.39i
5	-0.28 - 2.28i	-0.28 - 2.28i	-0.28 - 2.29i	-0.28 - 2.28i	-0.27 - 2.25i	-0.28 - 2.42i	-0.29 - 2.40i
6	-0.29 - 2.45i	-0.29 - 2.45i	-0.29 - 2.45i	-0.29 - 2.44i	-0.28 - 2.42i	-0.28 - 2.43i	-0.31 - 2.52i
7	-0.30 - 2.41i	-0.30 - 2.41i	-0.29 - 2.41i	-0.29 - 2.40i	-0.29 - 2.40i	-0.31 - 2.52i	-0.30 - 2.38i
8	-0.29 - 2.41i	-0.30 - 2.41i	-0.29 - 2.41i	-0.29 - 2.39i	-0.29 - 2.40i	-0.31 - 2.52i	-0.30 - 2.38i
9	-0.30 - 2.45i	-0.30 - 2.45i	-0.30 - 2.45i	-0.29 - 2.43i	-0.29 - 2.43i	-0.32 - 2.53i	-0.30 - 2.46i
10	-0.30 - 2.45i	-0.30 - 2.45i	-0.30 - 2.44i	-0.29 - 2.43i	-0.29 - 2.43i	-0.31 - 2.51i	-0.30 - 2.47i
11	-0.29 - 2.44i	-0.29 - 2.44i	-0.29 - 2.44i	-0.29 - 2.43i	-0.28 - 2.42i	-0.29 - 2.47i	-0.30 - 2.49i
12	-0.28 - 2.45i	-0.28 - 2.45i	-0.29 - 2.45i	-0.28 - 2.44i	-0.28 - 2.42i	-0.27 - 2.44i	-0.30 - 2.52i
13	-0.29 - 2.45i	-0.29 - 2.45i	-0.29 - 2.45i	-0.28 - 2.44i	-0.28 - 2.42i	-0.28 - 2.44i	-0.30 - 2.51i
14	-0.29 - 2.45i	-0.29 - 2.45i	-0.29 - 2.45i	-0.29 - 2.43i	-0.9 - 2.43i	-0.30 - 2.49i	-0.30 - 2.48i

Then the impact of the fault on bus j can be calculated as

$$\Delta V_j = I_i^{SC} Z_{ij}, \tag{3.5.2}$$

where

ΔV_j is the fault impact on bus j

Z_{ij} is the Thevenin equivalent impedance between bus i and j

Therefore, all the buses $i = 1, 2, 3, \cdots, n$ can be calculated, and the critical bus set $\mathbf{B}$ can be determined according to the voltage impacts.

3.5.2 A study example of IEEE 14-bus system

The IEEE 14-bus system is illustrated in Fig. 3.38. The impedance matrix can be calculated in Table 3.4. Considering the nature hazards, such as typhoon and earthquake, the parameters and the topology of power systems will change. For this IEEE 14-bus power system, it is assumed that the transmission lines between bus

Table 3.5: The impedance matrix of IEEE 14-bus system with a fault

Bus No.	*1*	*2*	*3*	*4*	*5*	*6*	*7*
1	-0.18 - 2.12i	-0.19 - 2.16i	-0.20 - 2.18i	-0.20 - 2.19i	-0.20 - 2.18i	-0.20 - 2.34i	-0.22 - 2.31i
2	-0.20 - 2.16i	-0.19 - 2.15i	-0.19 - 2.18i	-0.20 - 2.19i	-0.20 - 2.18i	-0.20 - 2.34i	-0.22 - 2.31i
3	-0.19 - 2.18i	-0.19 - 2.18i	-0.17 - 2.10i	-0.20 - 2.19i	-0.20 - 2.19i	-0.20 - 2.35i	-0.22 - 2.30i
4	-0.20 - 2.19i	-0.20 - 2.19i	-0.20 - 2.19i	-0.20 - 2.17i	-0.20 - 2.18i	-0.20 - 2.34i	-0.21 - 2.29i
5	-0.20 - 2.18i	-0.20 - 2.18i	-0.20 - 2.18i	-0.20 - 2.18i	-0.19 - 2.15i	-0.19 - 2.31i	-0.21 - 2.30i
6	-0.20 - 2.34i	-0.20 - 2.34i	-0.20 - 2.35i	-0.20 - 2.34i	-0.19 - 2.31i	-0.19 - 2.23i	-0.22 - 2.47i
7	-0.22 - 2.31i	-0.22 - 2.31i	-0.22 - 2.30i	-0.21 - 2.29i	-0.21 - 2.30i	-0.22 - 2.47i	-0.23 - 2.25i
8	-0.22 - 2.31i	-0.22 - 2.31i	-0.22 - 2.30i	-0.21 - 2.29i	-0.21 - 2.30i	-0.22 - 2.47i	-0.23 - 2.25i
9	-0.22 - 2.35i	-0.22 - 2.35i	-0.22 - 2.34i	-0.22 - 2.32i	-0.22 - 2.33i	-0.22 - 2.50i	-0.23 - 2.31i
10	-0.22 - 2.35i	-0.22 - 2.35i	-0.22 - 2.34i	-0.22 - 2.32i	-0.22 - 2.33i	-0.22 - 2.50i	-0.23 - 2.31i
11	-0.20 - 2.34i	-0.20 - 2.34i	-0.20 - 2.35i	-0.20 - 2.34i	-0.19 - 2.31i	-0.19 - 2.23i	-0.22 - 2.47i
12	-0.20 - 2.34i	-0.20 - 2.35i	-0.20 - 2.35i	-0.20 - 2.34i	-0.19 - 2.32i	-0.19 - 2.23i	-0.21 - 2.47i
13	-0.20 - 2.34i	-0.20 - 2.34i	-0.20 - 2.35i	-0.20 - 2.34i	-0.19 - 2.31i	-0.19 - 2.23i	-0.22 - 2.47i
14	-0.22 - 2.35i	-0.22 - 2.35i	-0.22 - 2.34i	-0.22 - 2.32i	-0.22 - 2.33i	-0.22 - 2.50i	-0.23 - 2.31i

Bus No.	*8*	*9*	*10*	*11*	*12*	*13*	*14*
1	-0.22 - 2.31i	-0.22 - 2.35i	-0.22 - 2.35i	-0.20 - 2.34i	-0.20 - 2.34i	-0.20 - 2.34i	-0.22 - 2.35i
2	-0.22 - 2.31i	-0.22 - 2.35i	-0.22 - 2.35i	-0.20 - 2.34i	-0.20 - 2.35i	-0.20 - 2.34i	-0.22 - 2.35i
3	-0.22 - 2.31i	-0.22 - 2.34i	-0.22 - 2.34i	-0.20 - 2.35i	-0.20 - 2.35i	-0.20 - 2.35i	-0.22 - 2.34i
4	-0.21 - 2.29i	-0.22 - 2.32i	-0.22 - 2.32i	-0.20 - 2.34i	-0.20 - 2.34i	-0.20 - 2.34i	-0.22 - 2.32i
5	-0.21 - 2.30i	-0.22 - 2.33i	-0.22 - 2.33i	-0.19 - 2.31i	-0.19 - 2.32i	-0.19 - 2.31i	-0.22 - 2.33i
6	-0.22 - 2.47i	-0.22 - 2.50i	-0.22 - 2.50i	-0.19 - 2.23i	-0.19 - 2.23i	-0.19 - 2.23i	-0.22 - 2.50i
7	-0.23 - 2.25i	-0.23 - 2.31i	-0.23 - 2.31i	-0.22 - 2.47i	-0.21 - 2.47i	-0.22 - 2.47i	-0.23 - 2.31i
8	-0.23 - 2.07i	-0.23 - 2.31i	-0.23 - 2.31i	-0.22 - 2.47i	-0.21 - 2.47i	-0.22 - 2.47i	-0.23 - 2.31i
9	-0.23 - 2.31i	-0.24 - 2.27i	-0.24 - 2.27i	-0.22 - 2.50i	-0.22 - 2.51i	-0.22 - 2.51i	-0.24 - 2.27i
10	-0.23 - 2.31i	-0.24 - 2.27i	-0.20 - 2.19i	-0.22 - 2.50i	-0.22 - 2.51i	-0.22 - 2.51i	-0.24 - 2.27i
11	-0.22 - 2.47i	-0.22 - 2.50i	-0.22 - 2.50i	-0.10 - 2.03i	-0.19 - 2.23i	-0.19 - 2.23i	-0.22 - 2.50i
12	-0.21 - 2.47i	-0.22 - 2.51i	-0.22 - 2.51i	-0.19 - 2.23i	-0.10 - 2.09i	-0.17 - 2.18i	-0.22 - 2.51i
13	-0.22 - 2.47i	-0.22 - 2.51i	-0.22 - 2.51i	-0.19 - 2.23i	-0.17 - 2.18i	-0.14 - 2.13i	-0.22 - 2.51i
14	-0.23 - 2.31i	-0.24 - 2.27i	-0.24 - 2.27i	-0.22 - 2.50i	-0.22 - 2.51i	-0.22 - 2.51i	-0.11 - 2.00i

13 and 14, and bus 11 and 10 are outaged. The impedance matrix can be calculated as shown in Table 3.5.

As illustrated before, it is assumed that a wind power plant is located as Bus 10. The voltage impact from large to small is $\{9, 7, 6, 11, 13, 4, 14, 5, 2, 12, 1, 3, 8\}$. Because the IEEE 14-bus system is relatively small, if there is a three-phase symmetrical fault occurs at Bus 10, the whole power system will be impacted heavily. This is the reason that the impedance elements in Table 3.4 and Table 3.5 are greater than 2 p.u.. So considering the greatest voltage impact, the first 30% voltage deviation impact buses are chosen, and the critical bus set is determined as $\{9, 7, 6, 11\}$. Considering the nature hazards, the transmission lines between Bus 13 and 14, and Bus 11 and 10 are outage. As above, the voltage impact from large to small is $\{9, 7, 4, 5, 2, 1, 8, 3, 6, 14, 13, 12, 11\}$. The critical bus set can be determined as $\{9, 7, 4, 5\}$.

Chapter 4

Synchrophasor measurement based renewable energy integration

In this chapter, an auxiliary control strategy with low computational load is proposed and studied for voltage stability enhancement. It is designed for both distribution system and transmission system under high penetration renewable energy. The distribution system and transmission system are modeled as a nonlinear MIMO dynamic system. This auxiliary controller will augment the existing control variables within the two systems.

In order to reduce computational complexity, the proposed control strategy is only triggered after the SVM controller predicts the voltage sag after disturbance event. In [73], voltage stability are classified into large-disturbance and small-disturbance voltage stability. Based on this, there are two different types of post-fault scenarios considered in this paper. Type I post-fault scenarios are with the condition that the equilibrium point is not changed. The linear time-invariant (LTI) control strategy is proposed for the Type I post-fault scenarios. Type II post-fault scenarios are with the condition where there is a significant change in the equilibrium point of the system. For the Type *II* post-fault, the linear time-variant (LTV) control strategy is utilized.

4.1 Formulation of the proposed fault analysis approach

4.1.1 Proposed approach for distribution system

As discussed in the before, an auxiliary coordinated control method focusing on voltage stability is proposed. The flowchart shown in Fig. 4.1 illustrates the strategies of the control system.

The voltage measured by PMUs at each bus, and wind speed measurements are used as the input of the SVM predictor. The SVM predicts a large voltage sag after a disturbance, which will be caused by two types of faults. Type *I* is the fault that do not change the equilibrium point of the system operating on. An example of this type of fault is wind speed fluctuation in a small range. Type *II* faults change the equilibrium point. An example of this type of fault load switching. If the predicted fault belongs to Type *I*, the LTI MPC is used.

On the other hand, if the fault belongs to Type *II*, the LTV MPC is used. In this paper, the control objective is to maximize the system voltage stability margin. The observed variables used by the MPC controller are the bus voltages on the critical buses in the distribution system [70, 75].

Considering the characteristic of the variable nature of the renewable energy generation, if the output power of wind turbine generators are not sufficient to cover the loads, the voltage will deviation. The proposed control strategy will be used to quickly stabilize the system voltage instantaneously.

A test system based on the IEEE 13-bus distribution system [6, 42] is shown in Fig. 4.2. Two Type III wind turbine generators (WTGs) W_1 and W_2 are connected

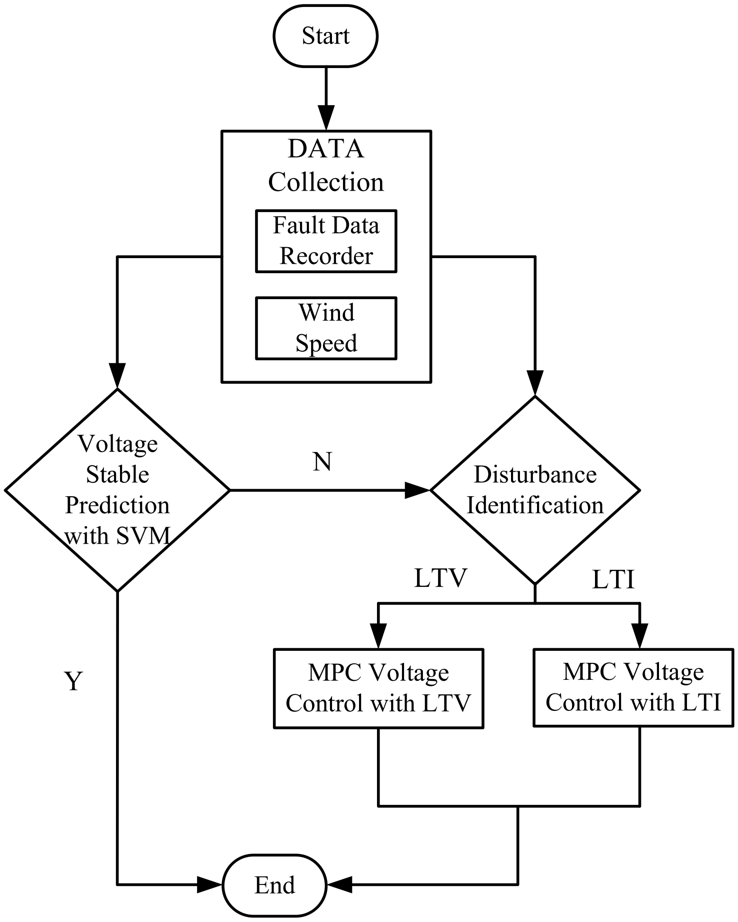

Figure 4.1: The data processing flowchart of the proposed method.

to bus 9 and 12, respectively. Both of them are doubly fed induction generators rated at 1.0 MW each with nominal frequency of 60 Hz [34].

There is a switch gear Sw connected load 14 to bus 6. The controlled vectors used for each WTG are pitch angle $\boldsymbol{\beta}_W = [\beta_1 \ \beta_2]^T$ and excitation voltage $\mathbf{E}_W = [E_{W_1} \ E_{W_2}]^T$, where T is matrix transpose. Wind speed are monitored for each wind turbine generator denoted as $\boldsymbol{\nu}=[\nu_1 \ \nu_2]^T$.

In addition to the WTGs, there is a traditional generator (TG), G_1 at 10 MW, 60Hz, which is connected to bus 1 as the Thevenin equivalent motor. $\mathbf{V}_{out} = [V_6 \ V_9 \ V_{12}]^T$ are selected as the observation variables [70, 75, 28, 125]. The controller adjusts the multiple input variables to stabilize the voltage on bus 6, 9, 12. This provides an efficient way to reduce the calculation burden and improve the feasibility.

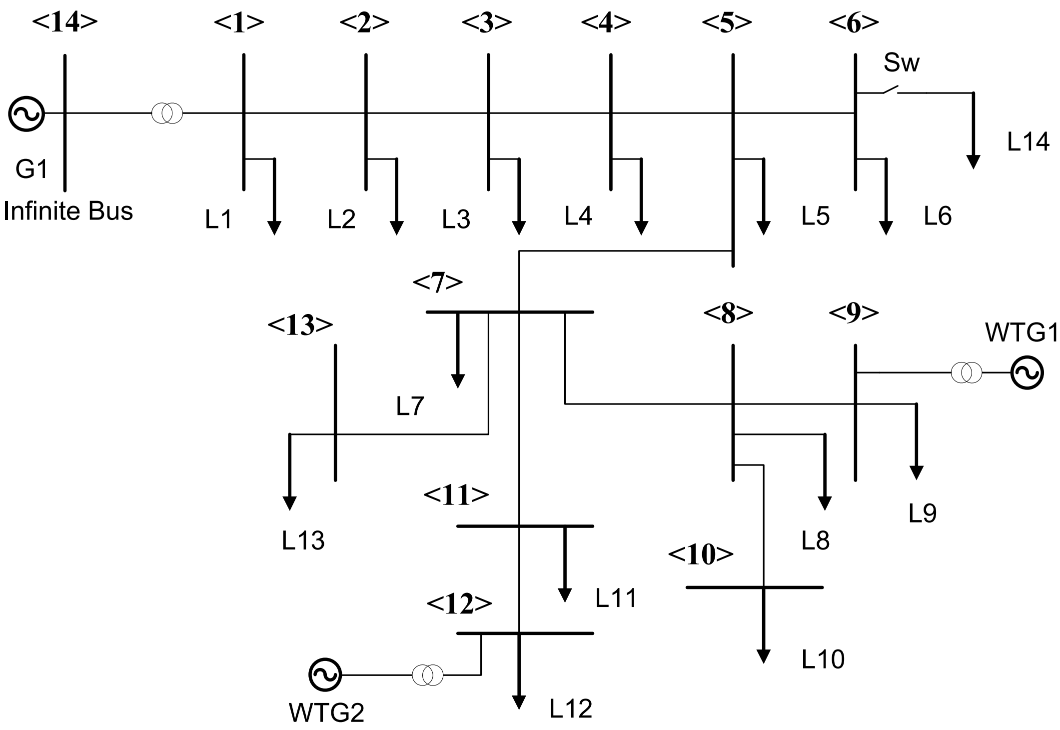

Figure 4.2: The test distribution system.

4.1.2 Proposed approach for transmission system

The flowchart is the same as Fig. 4.1. And the test system is shown in Fig. 4.3. A WPP consisting of two type III wind turbine generators (WTGs) W_1 and W_2 and a voltage condenser are connected to bus 15 through a 15 km transmission line. The WTG is a doubly fed induction generator rated at 1.5 MW each with nominal frequency of 60 Hz [34]. The controlled vectors used for each WTG are pitch angle $\boldsymbol{\beta}_W = [\beta_1 \ \beta_2]^T$ and excitation voltage $\mathbf{E}_W = [E_{W_1} \ E_{W_2}]^T$, where T is matrix transpose. Wind speed are monitored for each wind turbine generator denoted as $\boldsymbol{\nu}$=$[\nu_1\ \nu_2]^T$. In addition to the WPP, there are 2 TGs, G_1 and G_2; both of them are 4.5 MW, 60Hz. The transmission lines between bus 17 to bus 14, bus 16 to bus 14 are 8 and 12 km, respectively. G_3 is a 1.5 MW TG, connected through a switch gear Sw to bus 14.

The penetration level of wind energy is above 20%. The controlled vectors of the TGs are excitation voltage $\mathbf{E}_G = [E_1\ E_2]^T$ and mechanical power $\mathbf{M}_G = [M_1\ M_2]^T$. $\mathbf{V}_{out} = [V_1\ V_6\ V_9\ V_{12}]^T$ are selected as the observation variables [70, 75, 28, 125]. The controller adjusts the multiple input variables to stabilize the voltage on bus 1, 6, 9, 12 during the transient.

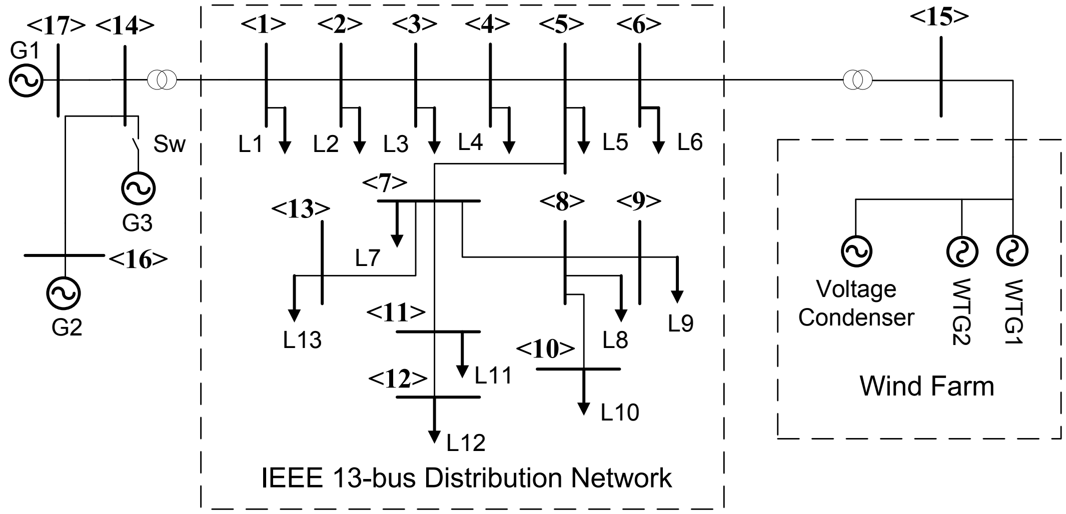

Figure 4.3: The test distribution system.

4.2 Voltage stability status prediction in distribution system

4.2.1 Basic concept of support vector machine

The SVM is a supervised learning method used for classification, regression and estimation problems. It is suitable to solve non-linear problems [21, 47]. The trajectory of the voltage stability status during transient is predicted using the SVM based predictor. The decision function $f(x)$, which is trained by historical data, classifies the new data into different classes and minimizes the classification error The basic SVM formulation is demonstrated as following, a set of training data $(x_1, y_1), ..., (x_N, y_N)$ is given. $x_i \in \mathbf{R}^D$ are the input vectors and illustrated as dots, y_i are the corresponding class labels, where $i = 1, 2, 3 \cdots N$. A hyperplane is built and separates the input vectors into two groups with the maximum margin of separability. N is the number of observations, and D is the dimension of the input vectors.

$$f(x) = \text{sign}\left\{ \sum_{j=1}^{N^{sv}} \alpha_j y_j^{sv} \Big(\Phi(\mathbf{x}) \Phi(\mathbf{x}_j^{sv}) \Big) + b \right\} \tag{4.2.1}$$

where $\mathbf{x}_j^{sv}$ are the support vectors, $\Phi(\cdot)$ is a non-linear vector function that maps the input vector onto a higher dimensional feature space, y_j^{sv} is the label corresponding to the jth support vector, N^{sv} is the number of support vectors, b is a bias term, and α_j are the Lagrangian multiples obtained from solving the dual optimization problem that minimizes the objective function defined in [21, 47].

$$\min \left\{ \frac{1}{2} \|\mathbf{w}\|^2 + C \sum_{i=1}^{N} \xi_i \right\} \tag{4.2.2}$$

subject to

$$\xi_i \geq 0 \quad \forall\ i = 1, ..., N \tag{4.2.3}$$

$$y_i(\mathbf{w} \cdot \mathbf{x}_i + b) \geq 1 - \xi_i \quad \forall\ i = 1, ..., N \tag{4.2.4}$$

This optimization is the process that trains the SVM by selecting the support vectors from the training data set. The parameter C ($C > 0$) in the objective function given in (2) is a factor that controls the trade-off between the separation margin and training errors, $\|w\|$ is the norm of a vector perpendicular to the separation hyperplane, and ξ_i are the slack variable which measure degree of misclassification. The inner product $\Phi(\mathbf{x})\cdot\Phi(\mathbf{x}_j^{sv})$ is called the kernel function and denoted by $K(\mathbf{x},\mathbf{x}_j^{sv})$. The kernel function used in this paper is the radial basis function:

$$K(\mathbf{x},\mathbf{x}_j^{sv}) = \exp(-\|\mathbf{x}-\mathbf{x_j^{sv}}\|/2\sigma^2) \tag{4.2.5}$$

where σ is the width of the Gaussian. This was selected because it gave the most satisfactory results when compared to the other alternative such as linear and polynomial functions [47].

4.2.2 SVM designed for distribution system and transmission system

In this approach, for the distribution system, the observation inputs used by the SVM predictor includes the voltage of every bus $\mathbf{V} = [V_1, V_2, V_3, \ ...\ V_{14}]^T$ of the system. Considering that wind speed varies with time, the wind speed $\boldsymbol{\nu}$=$[\nu_1\ \nu_2]^T$ is also used as the input to the SVM. So the observation vector is defined as $\mathbf{x} = [\boldsymbol{\nu}^T\ \mathbf{V}^T]^T$.

Similarly, for the transmission system, the observation inputs used by the SVM predictor includes the generator angle of the two TGs $\boldsymbol{\alpha}_G = [\alpha_{G1}\ \alpha_{G2}]^T$, the generator rotor speed $\boldsymbol{\omega}_G = [\omega_{G1}\ \omega_{G2}]^T$ and the voltage of every bus $\mathbf{V} = [V_1 ... V_{16}]^T$ of the system. Considering that wind speed varies with time, the wind speed $\boldsymbol{\nu}$=$[\nu_1\ \nu_2]^T$ is also used as the input to the SVM. So the observation vector is defined as $\mathbf{x} = [\boldsymbol{\alpha}_G^T\ \boldsymbol{\omega}_G^T\ \boldsymbol{\nu}^T\ \mathbf{V}^T]^T$.

The numerical simulated on both systems separately. Both normal operations and different types of disturbances are simulated for numerical experiments during the training sessions. For the distribution and transmission line faults, single-line to ground, line-to-line, and line-to-line to ground as well as three-phase-to-ground faults are simulated for all lines at different locations (at 5%, 10%, 25%, 50%, 60% and 80% of the length). The fault durations as 5, 10, 15, 20, 30 and 60 cycles as well as permanent faults with different starting times are simulated. Load increasing and decreasing at 1%, 2%, 3%, 5%, 10%, 15%, 17.5%, 20% and loads switching are simulated on the loads. The WTGs are simulated at different wind turbulence levels, respectively.

Both the opening and closing of the switch are also simulated. According to the rule presented in reference [47], the generated training data are labeled into classes, one is the normal condition and labeled as “1”; the other is disturbance condition and labeled as “-1”. The K-fold [66] cross-validation is used to separate the generated data into the training set and testing set. In this paper, 10 fold cross validation are selected; i.e., 90% of the generated data are used as the training data and 10% are used as the testing data.

To maintain the voltage stability, the controller is required to make a quick corrective action, to predict the status, and to deliver the control decisions [104, 47]. The overall control process is usually expected to take less than 1 second. In the proposed method, the observation time is set to 100 ms. The prediction algorithm is executed in a computer with Intel i7 3.0 GHz CPU and 12 GB RAM, and the resulting average computation time for prediction is only 14.93 ms.

4.2.3 SVM prediction results

Voltage stability with PMUs fully placed

For the distribution system, assuming that every bus in the system is equipped with a PMU, Table 4.1 illustrates that the prediction rate with such configuration is 100%, which demonstrates that the proposed method has higher successful prediction rates than the method in reference [47] whose results are shown in Table 4.2.

The performance improvement is due to the higher dimensional input vectors and longer observation time in the proposed approach, thus, allowing more information used in training of the SVM algorithm in the nonlinear system.

Table 4.1: Classification confusion matrix on distribution systems

	Normal	Disturbance
Normal	**1(150/150)**	0(0/150)
Disturbance	0(0/70)	**1(70/70)**

Table 4.2: Classification confusion matrix from reference[47]

	Normal	Disturbance
Normal	**0.973(146/150)**	0.027(4/150)
Disturbance	0.057(4/70)	**0.943(66/70)**

For the transmission system, assuming that every bus in the system is equipped with a PMU, Table 4.3 illustrates that the prediction rate with such configuration is 100%, which demonstrates that the proposed method has higher successful prediction rates than the method in reference [47] whose results are shown in Table 4.4.

Voltage stability with PMU optimally placed on selected buses

In real-world applications, the number of PMU is limited due to its cost. It is imperative to optimally place PMUs in the distribution system. For the distribution system, if PMUs are placed on buses 1, 3, 5, 8, 12, 13 the installation percentage is 42.8% of the total buses. The system is observable and the voltage on every bus of

Table 4.3: Classification confusion matrix on transmission systems

	Stable	Unstable
Stable	**1(140/140)**	0(0/140)
Unstable	0(0/60)	**1(60/60)**

Table 4.4: Classification confusion matrix from reference[47]

	Stable	Unstable
Stable	**0.978(137/140)**	0.022(3/140)
Unstable	0.050(4/60)	**0.950(56/60)**

Table 4.5: Confusion matrix with limited PMUs on distribution systems

	Normal	Disturbance
Normal	**1(150/150)**	0(0/150)
Disturbance	0(0/70)	**1(70/70)**

the system can be calculated [89, 58]. The prediction result shown in Table 4.5 is very good as well. Thus, the level of accuracy is not compromised. This provides a way to predict the voltage stability with reduced number of but optimally placed PMUs.

For the transmission system, if PMUs are placed on buses 2, 4, 6, 7, 8, 12, 14 the installation percentage is 41.2% of the total buses. The system is observable and the voltage on every bus of the system can be calculated [89, 58]. The prediction result shown in Table 4.6 is very good as well. Thus, the level of accuracy is not compromised. This provides a way to predict the transient voltage stability with reduced number of but optimally placed PMUs.

4.3 Auxiliary control strategy based on model predictive control

MPC has been successfully used in many industrial applications due to its ability to handle the nonlinear MIMO control problems with constraints on the system

Table 4.6: Confusion matrix with limited PMUs on transmission systems

	Normal	Disturbance
Normal	**1(140/140)**	0(0/140)
Disturbance	0(0/60)	**1(60/60)**

variables [84, 131]. In this paper, different types of faults in the power system with renewable energy generation is considered and a flexible control strategy based on MPC is proposed for the distribution system.

4.3.1 General control system formulation

The principle of MPC is illustrated in Fig. 4.4. Given the system state space model and the constraints of the variables, at the current time t, the MPC solves an constrained optimization problem over a finite prediction period $[t, t+T_p]$ aiming to minimize the predetermined objective function, where T_p is defined as the finite prediction horizon. For example, in Fig. 4.4, the finite prediction horizon is $T_p = 7$. The control variable is computed over the control horizon $[t, t+T_c]$, where $(T_p \geq T_c)$.

It is assumed that the discrete time state space model of the MPC is given by

$$X(t+1) = A(t)X(t) + B(t)U(t) + D_1(t)d_1(t) \tag{4.3.1}$$

$$Y(t) = C(t)X(t) + D_2(t)d_2(t) \tag{4.3.2}$$

where $X(t) \in \mathbf{R}^n$ is the system states at time t. $A(t) \in \mathbf{R}^{n\times n}$, $B(t) \in \mathbf{R}^{n\times m}$ and $C(t) \in \mathbf{R}^{l\times n}$ are the system control coefficient matrices, $U(t) \in \mathbf{R}^m$ is the control vector of the system; $Y(t) \in \mathbf{R}^l$ is the output vector of the system; $d_1(t)$ and $d_2(t)$ are the system state uncertainty and measurement noise, respectively, and their coefficient matrices are $D_1(t)$ and $D_2(t)$.

4.3.2 Auxiliary control for different generators

Different from traditional MPC strategies [76, 71], the proposed control strategy operates as an auxiliary controller and revises the control vector along the way. As Fig. 4.5 illustrates, the control loop in black is the existing control loop for the TG, which controls excitation voltage and mechanical power.

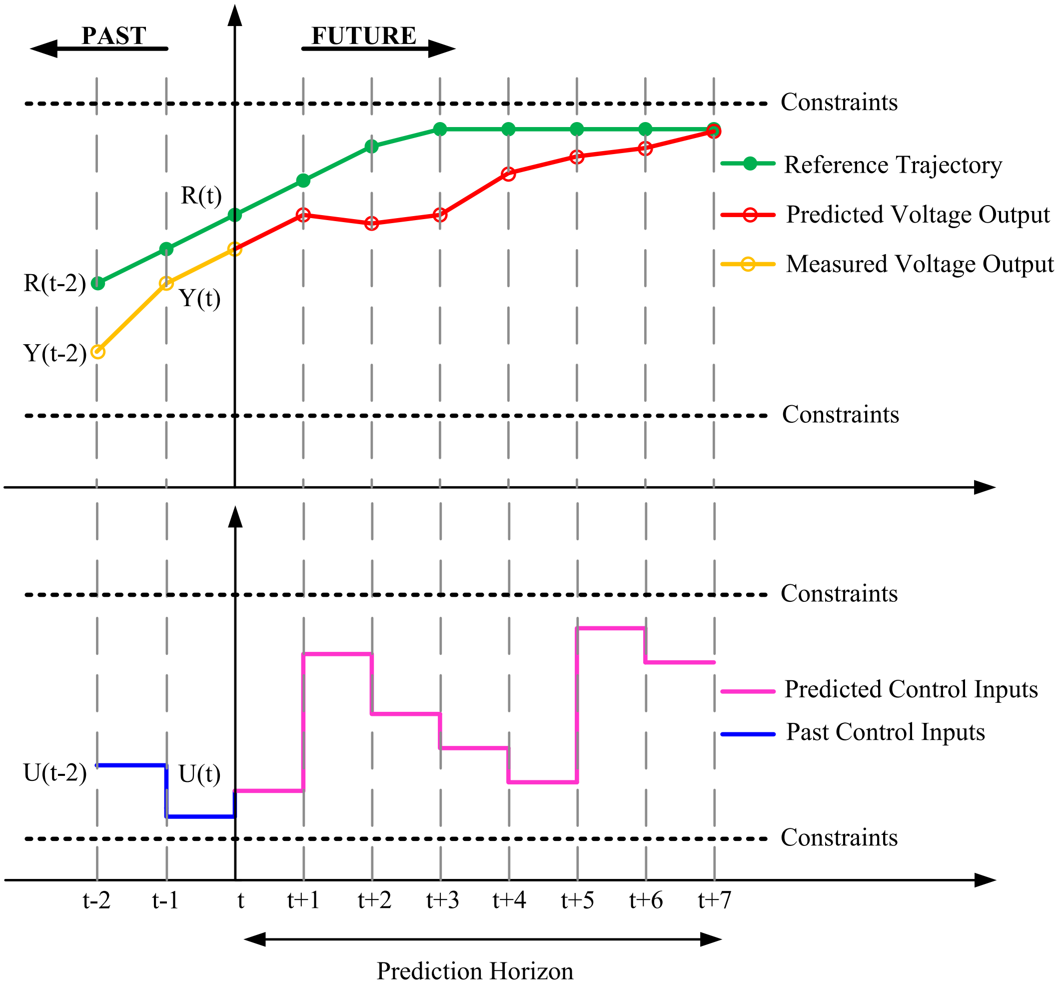

Figure 4.4: Model predictive control concept

The proposed control strategy uses the two adder blocks in red dashed line, the MPC controlled excitation voltage and MPC controlled mechanical power are two auxiliary control variables that revise the excitation voltage and mechanical power of the existing control loop. As shown in Fig. 4.6, the WTG controller controls the pitch angles of the wind turbine and excitation voltage variables. Auxiliary MPC blocks revise the pitch angle and excitation voltage variables in the existing control loops.

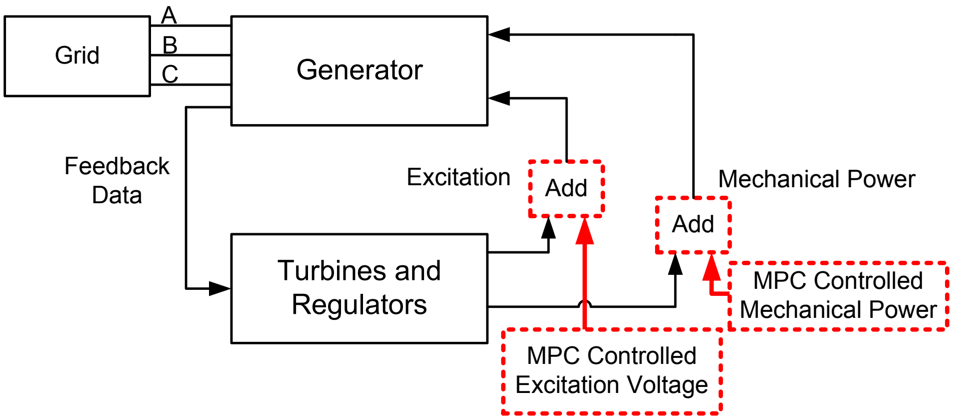

Figure 4.5: Designed model predictive control on traditional generator

4.3.3 Optimization strategy for MIMO control

To achieve the objective of voltage stability control, the control strategy considers both active power control and reactive power control. For the distribution system, the auxiliary MPC controlled variables contain excitation voltage $\mathbf{E}_{AW} = [E_{AW1}\ E_{AW2}]^T$ and pitch angle $\boldsymbol{\beta}_{AW} = [\beta_{AW1}\ \beta_{AW2}]^T$ for the WTGs. For the transmission system, the auxiliary MPC controlled variables contain excitation $\mathbf{E}_{AG} = [E_{AG1}\ E_{AG2}]^T$ and mechanical power $\mathbf{M}_{AG} = [M_{A1}\ M_{A2}]^T$ for the TGs; excitation voltage $\mathbf{E}_{AW} = [E_{AW1}\ E_{AW2}]^T$ and pitch angle $\boldsymbol{\beta}_{AW} = [\beta_{AW1}\ \beta_{AW2}]^T$ for the WTGs.

The optimization problems of both distribution system and transmission system are very similar. In this part, the distribution system is taken as an example to illustrate the optimization strategy on MIMO control.

The control vector U is the combination of the auxiliary MPC control vector $U_{MPC} = [\mathbf{E}_{AW}^T\ \boldsymbol{\beta}_{AW}^T]^T$ and existing control vector $U_{EX} = [\mathbf{E}_W^T\ \boldsymbol{\beta}_W^T]^T$. So U is given by

$$U = U_{MPC} + U_{EX}. \tag{4.3.3}$$

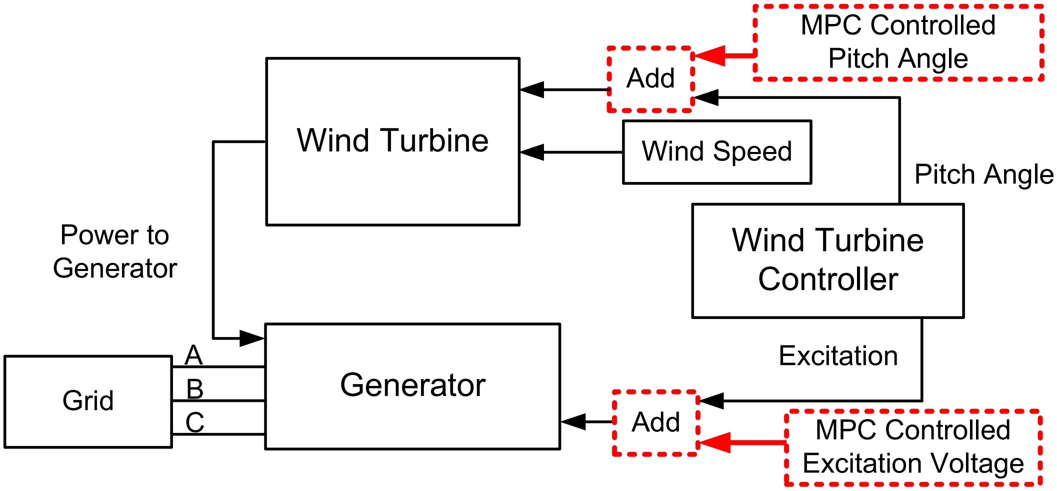

Figure 4.6: Designed model predictive control on wind turbine generator

The observation vector is the voltage measurements on bus 6, 9, 12, 13 denoted as $\mathbf{V}_{obs} = [V_6 \ V_9 \ V_{12}]^T$. According to the discussion above, based on the state space model, the optimization function can be defined as

$$\begin{aligned} J = &\sum_{j=N_1}^{N_1+T_p} \big[\hat{Y}(t+j|t) - R(t+j)\big]^T O \big[\hat{Y}(t+j|t) - R(t+j)\big] \\ &+ \sum_{j=1}^{1+T_c} \Delta U^T(t+j-1) Q \Delta U(t+j-1) \\ = &\sum_{j=N_1}^{N_1+T_p} \xi^T(t+j) O \xi(t+j) \\ &+ \sum_{j=1}^{1+T_c} \Delta U^T(t+j-1) Q \Delta U(t+j-1). \end{aligned} \tag{4.3.4}$$

Considering the realistic application, the constraints are

$$\begin{aligned} &\underline{y}_i \leq y_i \leq \bar{y}_i, i = 1, 2, 3... \\ &\underline{u}_i \leq u_i \leq \bar{u}_i, i = 1, 2, 3... \end{aligned} \tag{4.3.5}$$

where $\xi(t+j)$ is the error between the observation and the reference at time $t+j$; N_1 is the beginning of prediction horizon; $N_1 + T_p$ is the end of prediction horizon;

$1 + T_c$ is the upper value of the control horizon. $Y(t)$ is the observation vector of the distribution system at time t, which is the voltage measurement defined as before. The $\hat{Y}(t+j|t)$ is the expected observation vector of $Y(t+j)$ with available information at instant t, $R(t)$ is the reference observation vector. Δ is defined as $1 - z^{-1}$, where z^{-1} is the backward shift operator. O is the weighting matrix for predicted errors and Q is the weighting matrix for control moves. y_i and u_i are the elements of the vector Y and U, respectively. $\underline{y}_i$ and $\bar{y}_i$ are the lower and upper limits of y_i; $\underline{u}_i$ and $\bar{u}_i$ are the lower and upper limits of u_i.

Specifically, in this paper, the auxiliary MPC controller is not performed when the distribution system operates in a normal condition. The auxiliary MPC is triggered if the SVM based method predicts that the distribution system voltage will be unstable after a fault. For example, during the wind speed fluctuation or when the level of generation is less than the loads, the voltage may fluctuate, and the auxiliary MPC is triggered. It is assumed that the trigger time from SVM algorithm is t_s. So it is defined in (4) as N_1=t_s and the control horizon also starts at t_s. In order to enhance the control stability of the auxiliary MPC, the control horizon is increased and it is defined that as T_c=T_p=T_{stop}. Therefore, the sensitivity of the proposed control input in (4) can be represented as

$$\begin{aligned}\frac{\partial J}{\partial U_{MPC}} &= \frac{\partial J}{\partial U}\frac{\partial U}{\partial U_{MPC}} \\ &= \sum_{j=t_s}^{t_s+T_{stop}} \frac{\partial(\xi^T(t+j)O\xi(t+j))}{\partial U} \\ &+ \sum_{j=1}^{1+T_{stop}} \frac{\partial(\Delta U^T(t+j-1)Q\Delta U(t+j-1))}{\partial U}\end{aligned} \tag{4.3.6}$$

Since the per-unit system is convenient in distribution systems, the reference vector $R(t)$ can be defined as constant $R(t) = [1,1,1]^T$, where $t \geq N_1$. The control weighting matrices O and Q affect the performance of the MPC controller. For the first item $\sum_{j=t_s}^{t_s+T_{stop}} \frac{\partial(\xi^T(t+j)O\xi(t+j))}{\partial U}$ in (6), aiming to reduce the amplitude of the voltage deviation in a shorter time, the O can be defined as $O(j)$, which is a monotonically decreasing sequence with time index j. So the first errors are penalized more severely than the errors in subsequent periods, thus, provoking a tighter control. This means that the voltage deviations can be smoothed out quickly. On the other hand, the second item $\sum_{j=1}^{1+T_{stop}} \frac{\partial(\Delta U^T(t+j-1)Q\Delta U(t+j-1))}{\partial U}$ in (6) is used to constrain the variance range of the input variables to meet the physical constraints in real-world applications. The weight matrix Q affects the effectiveness of the control variables in the system. If the elements of the Q are set small, the response of the system will be fast. For different control strategies, the elements in Q are set different. For the voltage control, the elements in Q, which correspond to the excitation variables $\mathbf{E}_{AW} = [E_{AW1}\ E_{AW2}]^T$ of WTGs, are set smaller than others. Because these variables play a more important role for reactive power control to smooth out the voltage fluctuation quickly and effectively. Therefore, the optimization goal is to minimize the optimization function (4), which can be written as

$$\begin{aligned} \min J = \min \Big\{ & \sum_{j=t_s}^{t_s+T_{stop}} \xi^T(t+j)O(j)\xi(t+j) \\ & + \sum_{j=1}^{1+T_{stop}} \Delta U^T(t+j-1)Q\Delta U(t+j-1) \Big\} \end{aligned} \tag{4.3.7}$$

with the same constraints as (5).

At each time step, through minimizing the objective function, the MPC predicts the system state in the future time steps and computes the new control variables to stabilize the distribution system.

4.4 Control strategy design for LTI and LTV systems

In this part, the distribution system is taken as an example to illustrate control strategy. The control strategy designed for transmission system is similar.

4.4.1 Linearization of a nonlinear power system

In this part, after the voltage disturbance condition is predicted by the SVM predictor, the fault information including the fault identification and location can be generated by the PMU based methods [65, 136, 43]. According the fault information, the power system can be linearized on different equilibrium points, obtain the state space models and control the system with the optimization functions [82, 73, 74]

If the equilibrium point $\mathcal{X}_e$ meets the requirements in [82], which is a solution of the equilibrium equation of the power system, $\mathcal{X}_e$ is a stable equilibrium point. If the fault caused disturbance is within the control shift Z_0, the system can be controlled on the stable equilibrium point $\mathcal{X}_e$ or very near to $\mathcal{X}_e$. And the coefficient matrices of the state space model can be linearised in the neighbourhood of $\mathcal{X}_e$, the state space model is expressed as

$$X(t+1) = A_e X(t) + B_e U(t) + D_{1e} d_1(t) \tag{4.4.1}$$

$$Y(t) = C_e X(t) + D_{2e} d_2(t) \tag{4.4.2}$$

where A_e, B_e, C_e, D_{1e} and D_{2e} are defined similar to the equations presented in (1) and (2). In this condition, the power system state space model can be represented in linear constant coefficient state space model in (8) and (9).

Since the power system may operate on different equilibrium points in different scenarios, as the pretreatment of the auxiliary MPC, a state space modelling approach is proposed based on stable equilibrium point tracking. The initial stable equilibrium point of the power system is computed and the corresponding state space model is built when the power system operates normally. It is assumed that the fault happens at time t_0, if the stable equilibrium point of the power system does not change after the fault time t_0, the state space model stays the same, and the optimization function of MPC is computed based on this condition. If the stable equilibrium point changes after the fault time t_0, the state space model will be rebuilt, and a new optimization function will be computed to control the system.

4.4.2 Control strategy design for different system models

The voltage stability are classified into two subclasses, large-disturbance and small-disturbance voltage stability [73]. As explained before, the stable equilibrium point tracking is used for determining the two subclasses, and two types of post-fault scenarios are studied in this paper.

Type I faults do not change stable equilibrium point of the distribution system and the fault induced disturbance is smaller than the control shift. It is assumed that the fault happens at time t_0, and the state space model does not change before and after t_0. It is assumed that the equilibrium point is $\mathcal{X}_{eI}$. So the coefficient matrices can be computed and state space model of this process are

$$X(t+1) = A_I X(t) + B_I U(t) + D_{1I} d_1(t) \tag{4.4.3}$$

$$Y(t) = C_I X(t) + D_{2I} d_2(t) \tag{4.4.4}$$

where A_I, B_I, C_I, D_{1I} and D_{2I} are the linearized coefficient matrices of the LTI state space model. The optimization function keeps unchanged and the MPC computes the auxiliary control variables to stabilize the voltage in the distribution system.

Type II faults are defined in Section 4.1. The distribution system operates on the original stable equilibrium point. After the occurrence of fault, the distribution system's operation moves from the original stable equilibrium point to another stable equilibrium point. It is assumed that the fault happens in time t_0 and the original stable equilibrium point before t_0 is $\mathcal{X}_{eI}$. As a result, before t_0, the state space model of the distribution system is the same as (10) and (11).

After t_0, it is assumed that the system is operating on another stable equilibrium point $\mathcal{X}_{eII}$ and the state space model is denoted as

$$X(t+1) = A_{II}X(t) + B_{II}U(t) + D_{1II}d_1(t) \tag{4.4.5}$$

$$Y(t) = C_{II}X(t) + D_{2II}d_2(t) \tag{4.4.6}$$

where $t \geq t_0$, A_{II}, B_{II}, C_{II}, D_{1II} and D_{2II} are the linearized coefficient matrices. The elements and dimensions of the matrices may change in this faulty procedure. And a new optimization function needs to be re-computed based on (12) and (13) for the auxiliary MPC.

Therefore, according to the state space models on different stable equilibrium points of the distribution system operation, the distribution system can be modelled accurately in different fault scenarios, which makes auxiliary LTI MPC and LTV MPC feasible.

4.5 Stochastic scheduling of economic dispatch with renewable energy

4.5.1 Wind turbine modelling

Wind turbine characteristics

In this paper, a regular wind turbine is considered, the power generation P_w as a function of wind speed and wind turbine characteristics is given by [38]

$$P_w = \frac{1}{2}Cmv^2 = \frac{1}{2}C(vS\rho)(v^2) = \frac{1}{2}CS\rho v^3 = 0.6CSv^3 \tag{4.5.1}$$

where ρ is the air density, here is 1.2928 kg/m^3, S (m^2) is the swept area of the wind turbine, v (m/s) is the wind velocity, and C is the coefficient of the wind turbine 4.5.1.

Stochastic wind power modelling

The stochastic wind power generation can be modelled as following.

- The IEEE 24-bus Reliability Testing System (IEEE-RTS) is used as test bench. 4 wind farms are used to substitute the 4 conventional power plant in the IEEE-RTS. The 4 wind farms with nominal generation capacity of 150 MW, 250 MW, 400 MW and 600 MW, respectively.
- Each wind farm consists of a number of wind turbines, each with installed capacity of 2 MW
- The wind speed data is acquired from NREL's Western Wind Resource Database. The wind speed information of each generator is chose randomly from database 9 times per day for 50 days.
- A sample of the output power of the wind farm with 400 MW nominal generation capacity is computed by (4.5.1). The output power results are fitted into both Weibull distribution and Gaussian distribution in Fig. 4.7. The comparison is shown as following.

The probability density function of a Gaussian random variable is

$$f\left(x,\mu,\sigma\right)=\frac{1}{\sigma\sqrt{2\pi}}e^{-\frac{\left(x-\mu\right)^2}{2\sigma^2}} \tag{4.5.2}$$

where the parameter μ is the mean, the parameter σ is its standard deviation; and its variance is therefore σ^2 [64, 20].

The probability density function of a Weibull random variable is and $k > 0$ is the shape parameter and $\lambda > 0$ is the scale parameter of the distribution. If $k = 1$, it is exponential distribution and if $k = 2$, it is the Rayleigh distribution [64, 117, 26].

$$f(x; \lambda, k) = \begin{cases} \dfrac{k}{\lambda}\left(\dfrac{x}{\lambda}\right)^{k-1} \exp - (x/\lambda)^k & x \geq 0, \\ 0 & x < 0 \end{cases} \tag{4.5.3}$$

As it illustrated in Fig. 4.7, the red line is the fitting Weibull distribution with scale parameter $\lambda = 13.5$ and shape parameter $k = 2$; the pink dashed line is the fitting Gaussian distribution with $\mu = 12.09$ and $\sigma = 6.1534$. The fitness error can be calculate as in [69]. It is obviously that the Weibull distribution performs better than the Gaussian distribution, especially for the negative part. The Gaussian distribution fitting line has a negative part, but the Weibull distribution barely has the negative part [64].

In addition, because the $k = 2$ here, the Weibull distribution can be seemed as Rayleigh distribution in this scenario.

4.5.2 Formulation of joint economic dispatch and energy reserves

$$\underset{C_i, C_{W_j}, C_{R_j}, P_{G_i}, P_{W_j}, P_{R_j}}{\arg\ \min} \left\{ \sum_{i=1}^{M} C_i P_{G_i} + \sum_{j=1}^{N} C_{W_j} P_{W_j} + \sum_{j=1}^{N} C_{R_j} P_{R_j} \right\} \tag{4.5.4}$$

subject to (4.5.5),(4.5.6), (4.5.7), (4.5.8), (4.5.9).

$$C_{low} \leqslant C_i, C_{W_j}, C_{R_j} \leqslant C_{high} \tag{4.5.5}$$

$$P_{low} \leqslant P_{G_i}, P_{W_j}, P_{R_j} \leqslant P_{high} \tag{4.5.6}$$

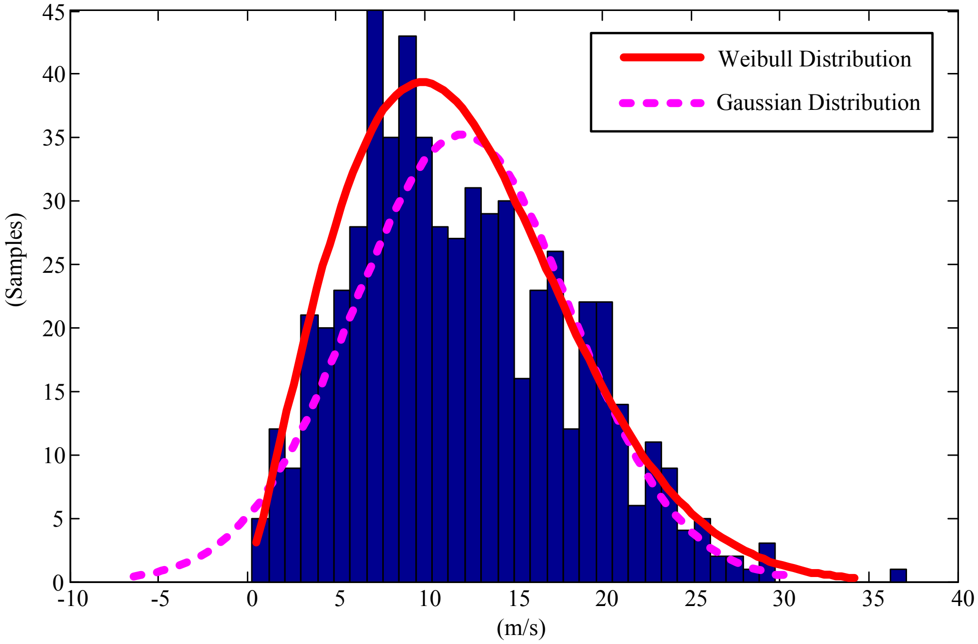

Figure 4.7: Wind speed fitting with Gaussian distribution and Weibull distribution

The hybrid economic dispatch problem is formulated as a optimization problem aiming to find the lowest power operating cost while keep the reliability of the power system. As shown in Fig. 4.8, the IEEE 24-bus Reliability Testing System (IEEE-RTS) is used as the test bench for the study. It is assumed that 6 generators in the power system are conventional energy generators and the rest are wind turbine generators. The optimization formulation including a objective function and constrains is described as following.

$$P_{G_i} + (P_{W_j} + P_{R_j}) = P_{load} \tag{4.5.7}$$

$$\sum_{i=1}^{M} P_{G_i} \leqslant P_{load} \times \gamma \tag{4.5.8}$$

$$P_{W_j} + P_{R_j} \leqslant P_{high}(W_j) + P_{high}(R_j) \tag{4.5.9}$$

$$Pr\Big\{ \sum_{j=1}^{n} (P_{W_j} C_{W_j} + P_{R_j} C_{R_j}) \leqslant b \Big\} \geqslant \alpha \tag{4.5.10}$$

where P_G is used to define the output power generated by the set of the conventional generators. All wind turbine are operating as deloaded. P_W and P_R are denoted the supplied power, respectively. $P_W = \{P_{W_1}, \cdots, P_{W_N}\}$ denotes the output power of the wind turbine generators, where P_{W_n} indicates the nth wind turbine generator output. The output power of wind turbine generators is defined as $P_R = \{P_{R_1}, \cdots, P_{R_N}\}$, where P_{R_n} denotes the power which can be supplied by the nth wind turbine generator in the reserve market. C_i is the power operating cost of conventional generators. C_{W_j} and C_{R_j} are used to represent the power operating cost of wind turbine generators in spot market and reserve market, respectively. C_{low} and C_{high} are used to define the upper and lower price limit for the power operating cost. The upper and lower power output limit of each generator are denoted by P_{low} and P_{high}. The power demand is described as P_{load}. γ is a ratio which represents the ratio of the conventional power with respect to P_{load}. $P_{high}(W_j) + P_{high}(R_j)$ is the maximum output for the jth wind turbine generator. In real application, the actual output power of each wind turbine generator must be less than its maximum power generation.

4.5.3 Derivation and transformation of chance constraint

The "chance constraint" is used to describe that the probability of a random event should be larger or smaller than a threshold. In this paper, the probability

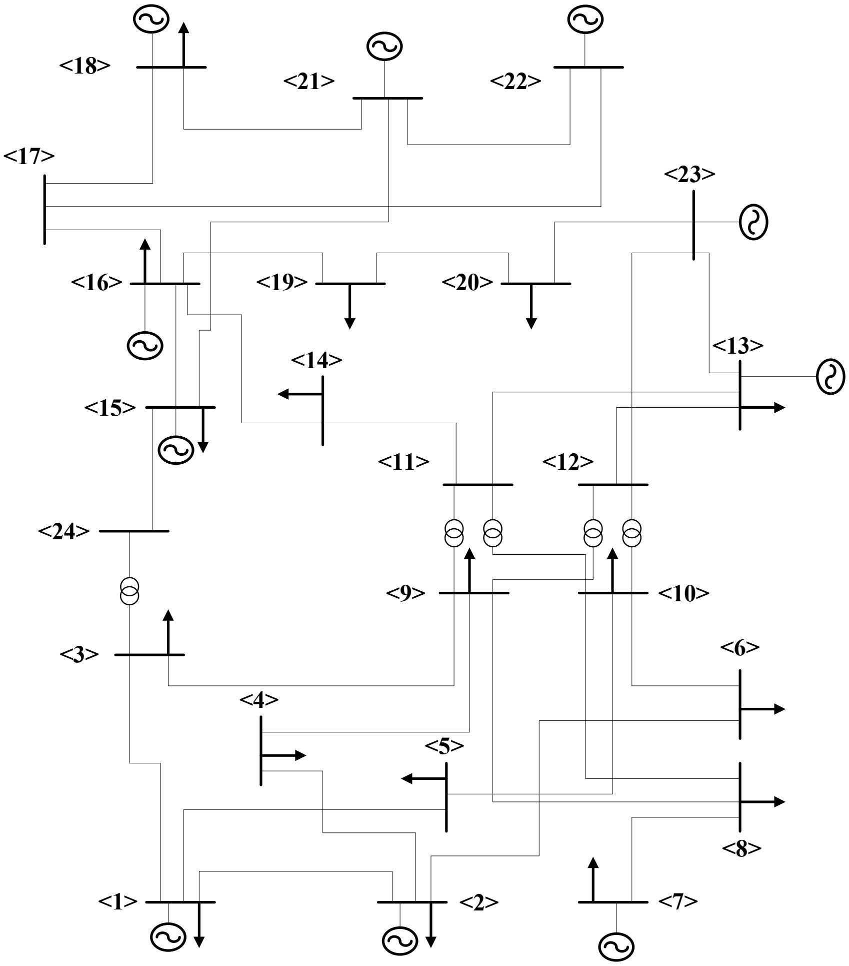

Figure 4.8: IEEE 24-bus RTS

larger than the threshold is take as an example.

$$Pr\{\sum_{i=1}^{n} a_i x_i \leqslant b\} \geqslant \alpha, \tag{4.5.11}$$

where the event is $\sum_{i=1}^{n} a_i x_i \leqslant b$, a_i and x_i are random variables, and b and α are two variables that determines the constraints.

In detail, the formula 4.5.11 can be wrote as following. This is a probability form and cannot be calculated by existed optimization programming language. This provide a new issue to solve. Furthermore, the probability constrain needs to be transformed into a mathematical form that can be directly used by computational algorithms, the transformation is derived as following

$$Pr\Big\{\sum_{j=1}^{n}(P_{W_j}C_{W_j}+P_{R_j}C_{R_j})\leqslant b\Big\}\geqslant\alpha. \tag{4.5.12}$$

$$y(C_{W_j},C_{W_j})=\sum_{i=j}^{n}(P_{W_j}C_{W_j}+P_{R_j}C_{R_j})-b. \tag{4.5.13}$$

The expectation and variance of $y(C_{W_j},C_{W_j})$ are:

$$E\big(y(C_{W_j},C_{W_j})\big)=\sum_{j=1}^{n}\{E[P_{W_j}]C_{W_j}+E[P_{R_j}]C_{R_j}\}-E[b] \tag{4.5.14}$$

$$V\big(y(C_{W_j},C_{W_j})\big)=\sum_{j=1}^{n}\{V[P_{W_j}]C_{W_j}^2+V[P_{R_j}]C_{R_j}^2\}+V[b] \tag{4.5.15}$$

Because each wind turbine generator has its controller, it is assumed that every wind turbine generator in the wind farm is independent in this paper. Therefore, each wind turbine generator is modeled independently.

Here, the Weibull distribution is used to forecast the wind speed and the output power of a wind turbine generator can be calculated with formula 4.5.1.

According to the Lyapunov Central Limit Theorem [44], the formula can be derived as

$$\frac{\sum_{i=1}^{n}(P_{W_j}C_{W_j}+P_{R_j}C_{R_j})-b-\big\{\sum_{i=1}^{n}\{E[P_{W_j}]C_{W_j}+E[P_{R_j}]C_{R_j}\}-E[b]\big\}}{\sqrt{\sum_{i=1}^{n}\{V[P_{W_j}]C_{W_j}^2+V[P_{R_j}]C_{R_j}^2\}+V[b]}}\sim N(0,1) \tag{4.5.16}$$

Finally, as the formulas above, the chance constrain can be derived into a feasible convex problem, which is a function and contains the mean and variance of the original probability function.

$$\begin{aligned} & \sum_{j=1}^{n}\{E[P_{W_j}]C_{W_j} + E[P_{R_j}]C_{R_j}\}+ \\ \phi^{-1}(\alpha) & \sqrt{\sum_{j=1}^{n}\{V[P_{W_j}]C_{W_j}^2 + V[P_{R_j}]C_{R_j}^2\} + V[b]} \leqslant E(b) \end{aligned} \tag{4.5.17}$$

where ϕ function is the cumulative distribution function of normal distribution [44]. In [56, 60, 138], the mean and variance of Weibull distribution are researched. The mean of the Weibull distribution is

$$\mu = c\Gamma\left(1 + k^{-1}\right) \tag{4.5.18}$$

The variance of the Weibull distribution is

$$\sigma^2 = c^2\Gamma\left(1 + k^{-1}\right) - \mu^2 \tag{4.5.19}$$

where the gamma function is defined as

$$\Gamma\left(x\right) = \int_0^\infty y^{x-1}e^{-y}dy,\ y > 0 \tag{4.5.20}$$

In the condition $k = 2$, it is Rayleigh distribution and $\mu = \dfrac{\sqrt{\pi}}{2}$ and $\sigma^2 = C^2(1 - \pi/4)$. The formula 4.5.17 can be solved.

4.5.4 Optimization solution algorithm

Generally, there are several optimization tools such as CPLEX, CVX, and genetic algorithm. CPLEX is an optimization tool, which is developed by IBM and usually be used in linear programming problems. The economic dispatch problem is a nonlinear optimization problem in this paper, so the CPLEX cannot meet the requirement. CVX is developed by Standford University, which cannot solve the problem more complex than the Quadratic problem and it also cannot met the requirement [91, 36]. The genetic algorithm (GA) is an artificial intelligence algorithm to simulate natural evolutionary processes, through retaining a population of candidate solutions to search for the optimal one. Some techniques are used to create candidate, which is inspired by crossover and selection. Compared with CPLEX and CVX, GA provides a flexible and robust way to find the global optimum solution for the optimization problem with the chance constraints. In [55, 54], a parallel computation method is provided to reduce the computation load of GA. As a result, the GA is chosen to solve the proposed optimization problem with the chance constraint.

4.5.5 Other algorithms

In real application, the wind turbine generator has a cut-in speed and a cut-out speed, which is design to avoid exceeding safe electrical and mechanical load limits [103]. This means that the wind turbine generator will not generate electrical power when the wind speed is lower than the cut-in speed or higher than the cut-out speed. Because of this, the formula 4.5.1 has some limitations. This characteristic also causes that the output electrical power of the wind turbine generator is not a continuous function, which means the traditional analytic methods have limitations to solve this problem. Therefore, in [130, 128], the Monte Carlo sampling and Latin Hypercube sample is used to solve this stochastic problems. Meanwhile, if combined with the wind forecast information, such as Bayesian network and Kalman filtering the energy scheduling strategy will be more effective and efficient [78, 16, 81].

4.6 Unbalanced three-phase power flow calculation for distribution system

Generally, there are four major methods to calculate power flow of distribution systems. The backward/forward sweep algorithm is an effective and efficient method, which utilizes the radial topology feature of distribution system. In distribution systems, usually there is only one path from a leaf bus to the slack bus. Based on this fact, the backward/forward sweep algorithm calculates the current and voltage along the path [29, 132, 17]. In [140, 142], the revised Newton-Raphson method is introduced, which linearises the revised power flow equations, then generates the power flow results. In [118, 30], the Z-bus method is introduced, which is mainly based on the injection current of each bus, the bus voltage, and the admittance matrix. Based on the KVL, a loop current equation is built to calculate the power flow of distribution system [49]. In this section, considering the feature of distribution system, the method based on backward/forward sweep algorithm is used to calculate the power flow of distribution systems. A 12-bus is used as test bench.

4.6.1 Formulation of distribution system power flow

As shown in Fig. 4.9, there are three major components in the proposed method. After the power system information is collected in the Data Input block. In the Basic Data Analysis block, the branch information is analyzed, and the topology information is collected. Then the adjacency matrix is built, which is a connectivity matrix and contains the topology information of the distribution system. The second major component is topology analysis, the depth-first search is used to collect all the leaf buses in the distribution system. And the breadth-first search is used to search different layers of the power system. In the third major component, the

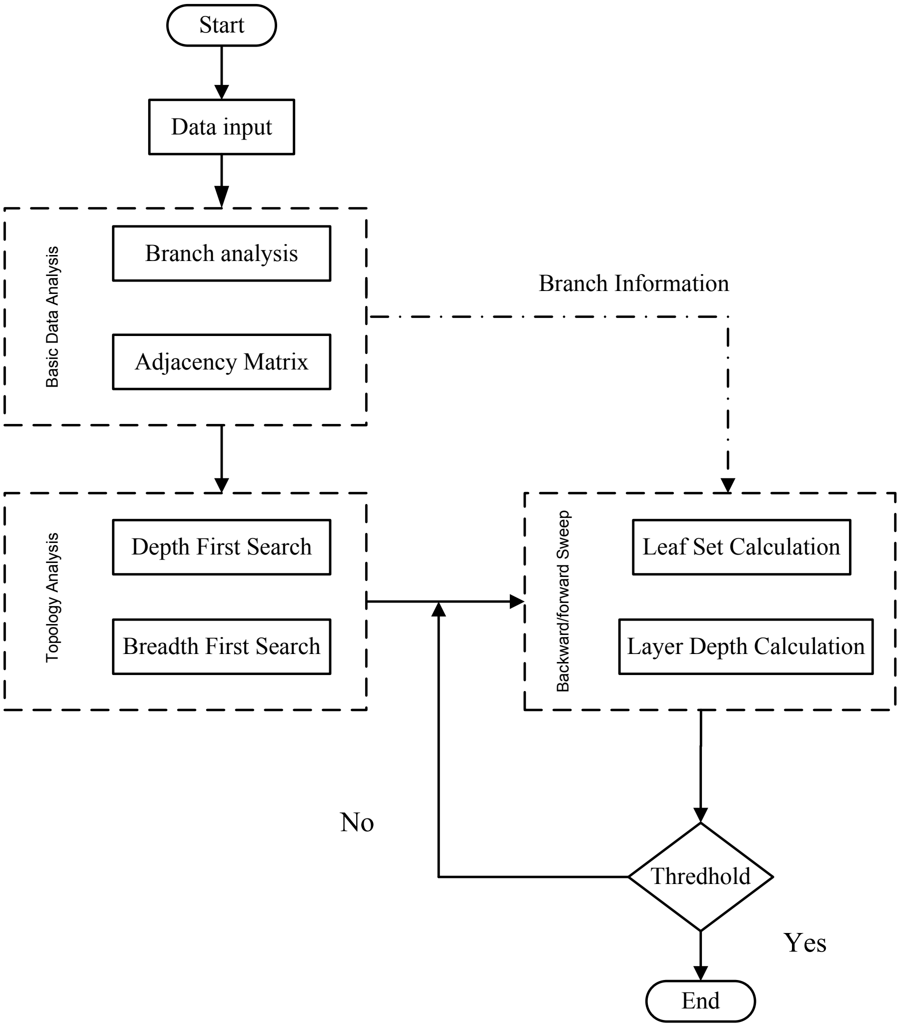

Figure 4.9: Flowchart of proposed power flow calculation in distribution system.

forward/backward sweep algorithm is used to calculate the power flow of the distribution system. When the voltage error between two iterations is smaller than a preset threshold, the algorithm will stop and generate the result.

4.6.2 Depth-first search and breadth-first search

For the second component of the proposed method, the depth-first search (DFS) and breadth-first search (BFS) is used to generate the leaf bus set and layers. In the distribution system, it is assumed that the direction of power flow is from the slack bus to the leaf buses. Because of the radial topology characteristic of the distribution system, each leaf bus has only one path to the slack bus. Therefore, in the first step, the DFS is used to generate the leaf bus set. Based on the results of DFS, the BFS is used to generate different layers, and then the backward/forward sweep algorithm is implement to calculate the power flow.

The DFS is a traversal searching algorithm, which can be used to searching the tree or graph data structures. At the beginning, the slack bus is set as the start point or root for the DFS. Then the algorithm searches all the edges or branches of the slack bus and chooses one of them. Through the selected branch, the new bus is added into the path. The DFS algorithm repeats this action until it finds the leaf bus. After the first path is generated, the DFS backtracks until all the buses are traversed in the distribution system. Finally, the leaf bus set can be generated by the DFS.

Based the leaf bus set generated by the DFS, the BFS is used to generate different layers. At the beginning, the slack bus is also set as the start point or root for the BFS, and indicates it as the first layer bus set. Then the algorithm explore all the edges or branches of the slack bus and selects the buses connected to them as the second layer bus set. Based on the second layer, the algorithm explore all the branches started from the second layer bus set and selects the buses connected to them as the third layer bus set. The stop condition of BFS algorithm is that all the buses in the distribution system are explored. According to this algorithm, different bus layer sets are generated, and the backward/forward sweep algorithm can be implemented.

As shown in Fig. 4.10, the 12-bus distribution is analyzed with DFS and BFS. The leaf bus set is $\{5, 6, 8, 10, 11, 12\}$. Through the BFS, the 12-bus distribution system can be divided into 5 different layer sets, the first bus layer set is $\{1\}$,

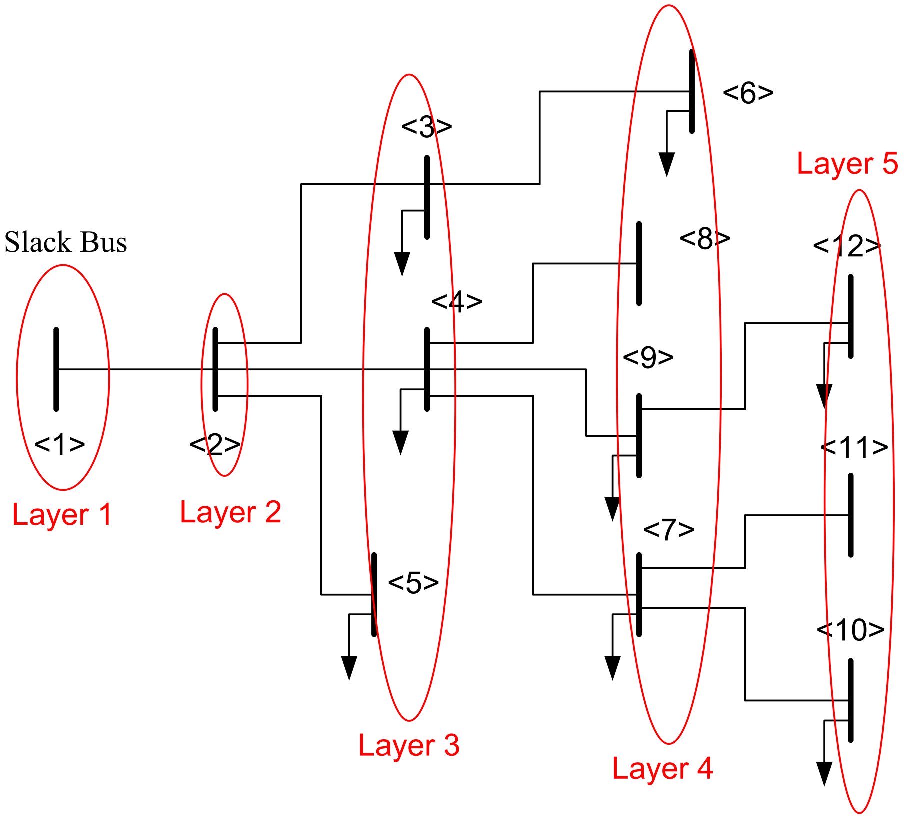

Figure 4.10: Topology analysis for the 12-bus distribution system.

the second is $\{2\}$, the third is $\{3,4,5\}$, the fourth is $\{6,7,8,9\}$ and the fifth is $\{10,11,12\}$.

4.6.3 Backward/forward sweep algorithm

Based on the topology analysis results, the backward/forward sweep algorithm is used to calculate the power flow of the distribution system. This algorithm has two major parts, backward sweep and forward sweep.

In this section, the backward sweep is used to calculate the current of each branch. At the beginning, the algorithm explore all the buses in the deepest layer set, for example, the deepest layer set is the fifth layer set in the 12-bus distribution system. The currents of the branches, whose terminal buses belong to the leaf bus set, can be directly calculate. Then for the fourth layer set, the algorithm finds out the leaf buses in this layer set, and calculate the current. For other buses, the KCL is used to calculate their currents. Finally, all the currents can be calculated in the backward sweep algorithm.

Table 4.7: The power flow results of the 12-bus distribution system

Bus No.	*A P.U.*	*A Angle*	*B P.U.*	*B Angle*	*C P.U.*	*C Angle*
1	1.0000	0.0000	1.0000	-120.0000	1.0000	120.0000
2	0.9747	0.2544	0.9711	-119.5238	0.9672	120.3589
3	0.9746	0.2818	0.9690	-119.5111	0.9677	120.3479
4	0.9746	0.3091	0.9669	-119.4983	0.9681	120.3369
5	0.9746	0.2818	0.9690	-119.5111	0.9677	120.3479
6	0.9709	0.3049	0.9659	-119.4445	0.9625	120.4094
7	0.9745	0.3089	0.9669	-119.4986	0.9681	120.3379
8	0.9744	0.3087	0.9669	-119.4988	0.9681	120.3386
9	0.9745	0.3089	0.9669	-119.4986	0.9681	120.3379
10	0.9745	0.3089	0.9669	-119.4986	0.9681	120.3379
11	0.9745	0.3089	0.9669	-119.4986	0.9681	120.3379
12	0.9746	0.3064	0.9669	-119.4905	0.9675	120.3380

In the forward sweep, with the current results of all the branches, the voltage can be updated with the KVL. The stop condition is that the voltage magnitude error between two iterations are smaller than a threshold, the algorithm can be deemed as converged. In this section, the threshold is set to be 1^{-10}.

The power flow calculation results of the 12-bus system are illustrated in Table 4.7. It is noted that the voltage magnitudes and angles of the three phase are unbalanced.

Chapter 5

Numerical results

5.1 Numerical results of wavelet based fault location

We demonstrate our fault localization results using the IEEE 39-bus system and suppose that every bus in the system is equipped with a PMU for real-time data acquisition with a sampling rate of 1 kHz. The simulation duration is 2 s and all the simulated faults start at 0.5 s. The short-term faults are set to last 10 cycles, about 0.167 s, and the long-term faults last to the end of simulation. We use the hybrid clustering algorithm to cluster the feature WTCs into 5 subsets. And we note the indexes of the feature WTC subsets is positively related with the distance from the fault. For example, buses in subset 1 are closest to the fault location and buses in subset 5 are the farthest ones. Using to the clustering results, the fault contour map are drawn to locate the fault in the IEEE New England 39-bus system.

5.1.1 Transmission line fault

A three-phase short fault is set between Bus 4 to Bus 14 in the system. The feature WTCs are clustered into 5 subset as in Table 5.1. The fault can be successfully located using the fault contour map as in Fig. 5.1. The blue circle which is near the boundary of the system corresponds to the subset 5 of the feature WTC set $C_l^{(m_l,n_l)}$, and represents the lowest impact level. In this subset, the buses are either directly connected to the generators or near them, as a result, these buses have the smallest fluctuations in the system as the generators can compensate the voltage fluctuation in power systems.

Table 5.1: Impact level of transmission line fault

Level	Bus number
1st (nearest to fault)	4,14
2nd	3,5,6,7,11,13,15,18
3rd	2,8,9,10,16,17,21,24,26,27
4th	1,19,22,23,25,28
5th	12,20,29,30,31,32,33,34,35,36,37, 38,39

There is another smaller blue circle in the middle of the map, as there are two transformers linking the buses in this area, which can also reduce voltage fluctuation. The yellow, orange and pink circles represent the subsets 4, 3 and 2, respectively. The voltage fluctuation gradually increases in these bus subsets. The subset 1 is denoted with a red ellipse, and bus 4 is denoted with a red circle as it is with the largest feature WTC value. The red ellipse and circle illustrate that the fault is approximately located in this area and bus 4 is with the highest probability. Also, the pink circle indicates the area where the electronic equipments would be damaged if the fault exist for a long time.

5.1.2 Generator fault

Generator disconnection is a type of indispensable fault in generator fault. In this paper, a generator disconnection at Generator 3 is investigated with the proposed wavelet-based fault location approach in this section.

According to Table 5.2, the fault contour map is determined as in Fig. 5.2. The colors of the circles from blue to red indicate different fault impact levels from light

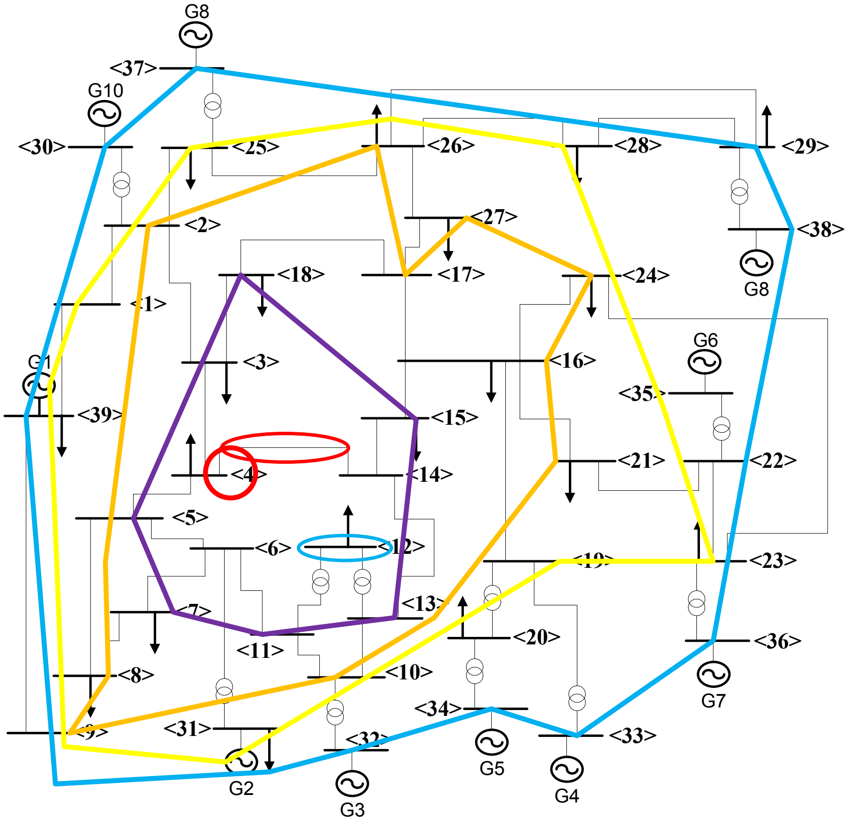

Figure 5.1: Fault contour map for transmission line

to heavy. The generator fault is localized at Generator 3 on Bus 32 using the pink and red circles. Bus 10, the nearest bus to generator 3, has the second largest fault impact, which is indicated by a red ellipse.

Table 5.2: Impact level of generator disconnection fault

Level	Bus number
1st (nearest to fault)	10,32
2nd	11,13,14
3rd	4,5,6,7,8,15
4th	2,3,16,17,18,21,24,27,
5th	1,9,12,19,20,22,23,25,26,28,29,30, 31,33,34,35,36,37,38,39

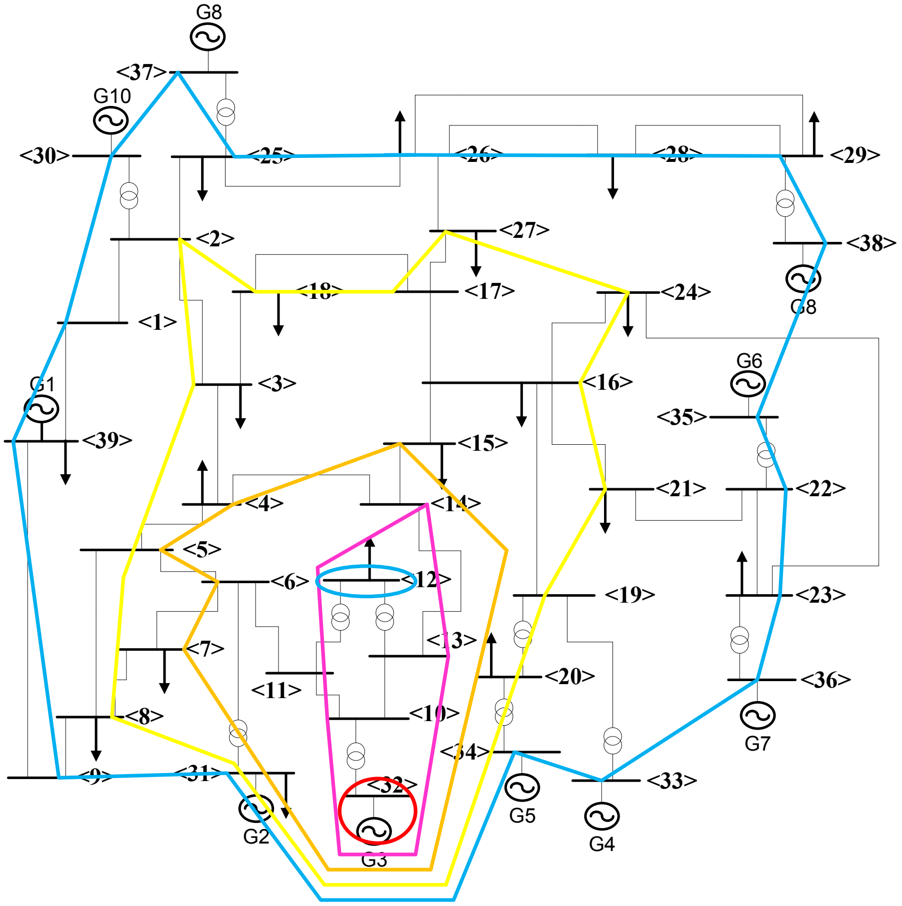

Figure 5.2: Fault contour map for generator disconnection

5.1.3 Load fault

The transformer fault, transmission line fault, and generator fault are discussed as above. In this paper, a load grounding at Bus 15 is investigated as load fault in this paper.

According to Table 5.3, the fault contour map is determined as in Fig. 5.3. As we can see, Bus 15 has the largest fault impact which is circled with red. The blue circle and yellow circle cross at Bus 38 where Generator 9 is located and compensates the power loss.

Table 5.3: Impact level of load fault

Level	Bus number
1st (nearest to fault)	15
2nd	13,14,16,17,24
3rd	3,4,11,18,21,27
4th	2,5,6,7,8,9,19
5th	1,10,12,20,22,23,25,26,28,29,30, 31,32,33,34,35,36,37,38,39

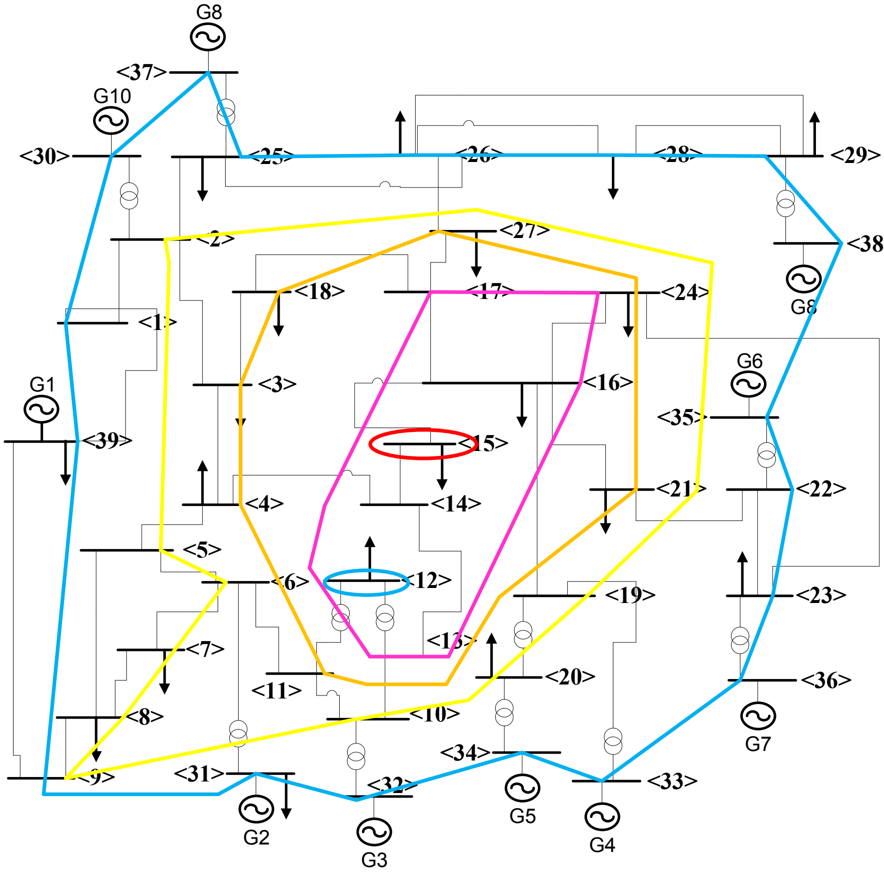

Figure 5.3: Fault contour map for load ground

5.2 Numerical results of data-driven fault diagnosis approach

The proposed fault detection, identification and location approach is demonstrated with the IEEE New England 39-Bus System simulated in PSCAD. It is assumed that a FDR is equipped at every bus, which performs real-time data acquisition. The sampling rate of the FDRs is 1 kHz.

Four fault types are investigated in our numerical simulation, which are generator ground fault I, transmission line outage II, generator outage III and load loss IV. The simulation lasts 5 s and the fault randomly occurs at 2, 2.5, 3, 3.5, 4 s with duration of 5 or 10 cycles. For each fault simulation, the power system component from all generators, loads and transmission lines in the 39-bus system are randomly chosen, and different types of faults are simulated to obtain sufficient training data. For the transmission line outage, the faults are created randomly at 5%, 50%, 75%, and 90% of the line distance between the two connecting buses. For the MPD feature extraction, a Gaussian atom dictionary with 1,800,000 normalized Gaussian atoms is built. Considering the trade-off between residual signal energy and computation load, the iteration number is set as 30 for frequency signal feature extraction and 10 for voltage signal feature extraction. The number of symbols is $A_{obs} = 256$ for frequency signal processing. The DHMMs with hidden state number of 3, 4, and 5 are modelled to compare the recognition performance. The SNR of FDR measurements is usually larger than 72 dB as shown in [137, 141]. To evaluate the performance of the proposed approach in much worse noise scenarios, our approach is evaluated using the signals with 10 dB SNR.

All simulations are executed in a laptop with Intel i7 3.0 GHz CPU and 8 GB RAM, and the proposed detection, identification and location algorithms are implemented in Matlab. The computation time for frequency signal feature extraction and classification is 0.9 s and for voltage signal processing is 0.5 s. Because the frequency and voltage signal processing channels work in parallel, the total computation time is less than 1 s.

5.2.1 Feature extraction results

For a simulation period of 5 s, 5000 data samples are collected for analysis. After the 10 MPD iterations for feature extraction, the 5000 data samples are extracted into 10 four-dimensional feature vectors $[\alpha, \tau, \nu, \sigma]^T$, with each representing the amplitude, time-shifting, frequency-shifting and variance of the Gaussian atoms. The total data number is $10 \times 4 = 40$, and the data compression rate is 125.

5.2.2 HMM based fault detection and identification results

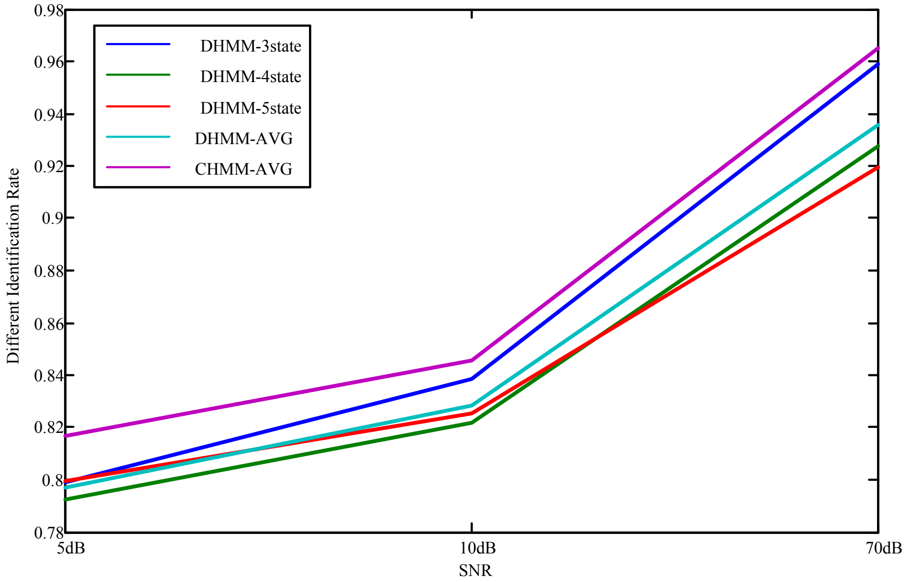

Figure 5.4: Fault identification rate comparison

1) From the confusion matrices and Fig. 5.4, we notice that compared with discrete HMMs, the continuous HMMs perform better in fault identification. Although in some scenarios, the identification rates are almost the same between discrete and continuous HMMs, such as the discrete HMM with 3 states and the continuous HMM with 6 Gaussian components. The average identification rate using continuous HMMs, 0.876, is higher than the result from discrete HMMs, 0.855. Considering

the cases of signals with additive white Gaussian noise (AWGN), the HMMs without noise have higher identification rate for all the Discrete HMMs and Continuous HMMs.

2) For the performance under different SNRs, the identification rate increases when the SNR increases. For example, compared with SNR 5 dB of the identification, 10 dB identification rate, the average fault identification rate increases from 79.6% to 83.6%. Actually, it can be explained that with the energy of noise decreasing, the margin between different fault types are becoming wider and the identification rate is increasing. When SNR = 5 dB, both the discrete and continuous HMM based classifiers have the lowest identification rate, but they are still above 75%, which meets the requirement of real-world applications. For noise-free cases, both the discrete and continuous HMM based classifiers have the highest identification rate, which are above 90%.

3) For different numbers of hidden states in Discrete HMMs, the HMMs with 4 or 5 hidden states perform better than 3-state HMMs in some conditions, such as 10 dB SNR, the load grounding fault identification rate with 4 and 5 hidden states is higher than 3 hidden states. But in average, according to the identification rate in confuse matrices, the HMMs with 3 hidden states are more robust with respect to different SNRs.

4) The identification rate in fault detection: the identification rate between abnormal and normal SG states is 100%, which implied that the identification margin between abnormal and normal states is large enough for clear identification in all the experiment scenarios.

According to these results, the HMM based method performs very well in fault detection and identification, which provides a novel way to detect and identify the faults based on PMU data in real time.

Table 5.4: Confusion matrix of fault detection between different conditions

	Normal	Abnormal
Normal	**100%**	0
Abnormal	0	**100%**

Table 5.5: Confusion matrix of fault diagnosis, SNR = 70 dB

	Discrete HMM with 3 States				Discrete HMM with 4 States			
	I	II	III	IV	I	II	III	IV
I	**0.951**	0	0	0.049	**0.923**	0	0.035	0.042
II	0.027	**0.962**	0	0.011	0.038	**0.962**	0	0
III	0	0	**0.958**	0.042	0	0.066	**0.918**	0.016
IV	0.019	0	0.016	**0.965**	0	0.063	0.030	**0.907**

	Discrete HMM with 5 States				Continuous HMM			
	I	II	III	IV	I	II	III	IV
I	**0.928**	0	0.020	0.042	**0.961**	0	0.010	0.029
II	0.075	**0.903**	0	0.022	0	**0.971**	0.029	0
III	0	0.046	**0.933**	0.021	0	0.026	**0.953**	0.021
IV	0.036	0.013	0.038	**0.913**	0.013	0	0.012	**0.975**

Table 5.6: Confusion matrix of fault diagnosis, SNR = 5 dB

	Discrete HMM with 3 States				Discrete HMM with 4 States			
	I	II	III	IV	I	II	III	IV
I	**0.826**	0.044	0.081	0.049	**0.810**	0.058	0.076	0.056
II	0.087	**0.802**	0.088	0.023	0.051	**0.821**	0.064	0.064
III	0.034	0.103	**0.781**	0.082	0.074	0.067	**0.769**	0.090
IV	0.079	0.048	0.086	**0.787**	0.080	0.101	0.049	**0.770**

	Discrete HMM with 5 States				Continuous HMM			
	I	II	III	IV	I	II	III	IV
I	**0.812**	0.087	0.059	0.042	**0.826**	0.054	0.103	0.017
II	0.055	**0.820**	0.074	0.051	0.075	**0.823**	0.053	0.049
III	0.089	0.090	**0.775**	0.046	0.062	0.074	**0.811**	0.053
IV	0.067	0.099	0.042	**0.792**	0.077	0.043	0.073	**0.807**

5.2.3 Results with limited distributed synchrophasor sensors

In real-world applications, the number of the FDRs is limited and cannot be placed in every bus due to installation and operation costs. It is assumed that the

Table 5.7: Confusion matrix of fault diagnosis, SNR = 10 dB

	Discrete HMM with 3 States				Discrete HMM with 4 States				Discrete HMM with 5 States				Continuous HMM			
	I	*II*	*III*	*IV*	*I*	*II*	*III*	*IV*	*I*	*II*	*III*	*IV*	*I*	*II*	*III*	*IV*
I	**0.852**	0.035	0.064	0.049	**0.821**	0.081	0.062	0.036	**0.830**	0.024	0.049	0.097	**0.858**	0	0.087	0.055
II	0.058	**0.820**	0.061	0.061	0.070	**0.843**	0.018	0.069	0.063	**0.839**	0.077	0.021	0.066	**0.854**	0.023	0.047
III	0.067	0.023	**0.846**	0.064	0.063	0.049	**0.812**	0.076	0.084	0.021	**0.812**	0.083	0.043	0.011	**0.850**	0.096
IV	0.071	0.030	0.063	**0.836**	0.096	0.063	0.030	**0.811**	0.046	0.022	0.038	**0.821**	0.042	0.032	0.105	**0.821**

FDRs on bus 1, 2, 5, 6, 13, 14, 17, 19, 22 are removed, and our approach is applied on the signals collected from the remaining FDRs. The fault detection rate of 99.1% and the fault identification rate of 91.9% are achieved using CHMM without noise. It is noted that the optimal FDR placement and minimization of the number of FDRs are still open problems for research [58].

5.2.4 Comparison with other methods

In [72, 2, 97, 8], artificial neural network (ANN) and support vector machine (SVM) are studied to detect and diagnose faults in power systems. ANN is a supervised learning model with hidden neurons, which can be used for fault classification and pattern recognition. SVM is also a supervised learning model, which builds a hyperplane for feature classification.

Using the same simulation test bench as described at the beginning of Section 5.1, the fault detection rates and identification rates obtained using ANN, SVM, and our proposed approach are demonstrated. For the proposed method in this paper, the CHMM fault detection and identification rates are used for comparison.

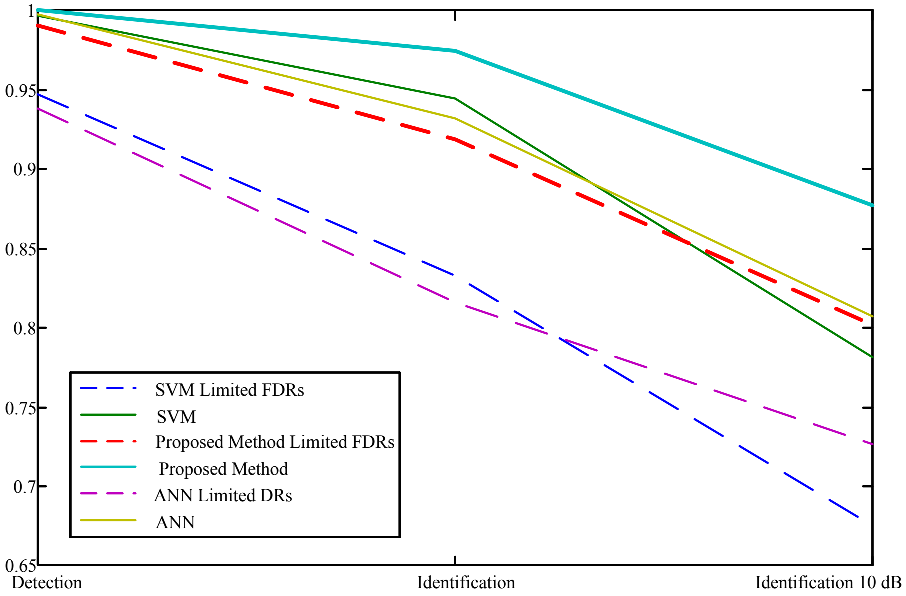

Figure 5.5: Fault detection and identification rate compared with other methods

As shown in Table 5.8, the detection and identification rates achieved by the three methods are all very high. The proposed method performs best among them, especially for fault identification under low SNR scenarios, because the MPD used in the proposed method can preserve signal feature and depress noise.

As shown in Table 5.9, with limited FDRs, the proposed method performs better than the other two methods, especially in low SNR scenarios. The fault detection rate of the proposed approach is still very high, but the fault identification rates are lower compared with the identification results obtained by the proposed approach in Table 5.8. On one hand, this illustrates that, under the condition of a reduced number of FDRs, the proposed approach is more robust than the other two methods. On the other hand, this fact also illustrates that the reduced number of FDRs impacts fault identification greatly due to the loss of useful information.

Table 5.8: Detection and identification rates of different methods

	Detection	Identification	Identification 10 dB
ANN	99.8%	93.2%	80.7%
SVM	99.7%	94.5%	78.2%
Proposed Method	100%	97.5%	87.7%

Table 5.9: Detection and identification rates with limited FDRs

	Detection	Identification	Identification 10 dB
ANN	93.8%	81.6%	72.7%
SVM	94.7%	83.3%	67.5%
Proposed Method	99.1%	91.9%	80.2%

5.2.5 Fault location results

The generator outage at bus 32 is used to demonstrate an example of our fault location results. After being processed by the clustering algorithm, the 39 buses are classified into 5 different levels as in Table 5.10. According to the result of clustering which indicates different fault impact levels, the fault contour map is generated as shown in Fig. 5.6.

Table 5.10: Impact level of generator outage

Impact Level	Bus number
1st (nearest to fault)	32
2nd	10,11,13,
3rd	4,5,6,7,8,14,15
4th	2,3,16,17,18,24,27,
5th	1,9,12,19,20,21,22,23,25,26,28, 29,30,31,33,34,35,36,37,38,39

As in Fig. 5.6, the colours of the circles from dark to light indicate the impact of the fault from heavy to small. The lightest dashed circle outside indicates the smallest impact due to the generator outage. As a power source is connected to bus 39, the fluctuation is smaller due to compensation from this generator. As a result, there are very small fluctuations in bus 39, 1, and 9. The voltage fluctuation in bus 12 is reduced because there is a transformer linking the high voltage buses

11, 13 and the low voltage bus 12. With the colours from light to dark, the circles shrink towards the fault area gradually, which indicates that the impact of the fault increases in these areas. Bus 32 suffers the largest impact, as it is directly connected to generator 3, which is indicated by a black circle. As a result, the fault impact area and location of the fault are determined by the fault contour map.

To evaluate the performance of the fault location method, 80 different random faults, including generator ground faults, transmission line outage, generator outage and load loss, are randomly generated and simulated at different locations in the IEEE New England 39-bus system, to evaluate the fault location method's performance. The success rate of locating a fault is 100%, and it can be concluded that the proposed location approach is robust given the above experimental scenarios and setup.

5.3 Numerical results of WAM with OSSP

In order to demonstrate the proposed spatial-temporal synchrophasor measurement system characterization approach and its application on fault detection and identification, the IEEE 14, 30, 39 bus systems are employed for experiments on numerical simulations. All the simulations are executed using a computer with 3.00 GHz Intel i7 CPU and 12 GB RAM. The resulting binary integer linear programming is solved by CPLEX Toolbox for Matlab, and the overall OSSP is studied with Matlab with Power System Analysis Toolbox (PSAT). The time consumed for each simulation is less than 1 s. Five power system fault scenarios are simulated with *(I)* Ignoring the effect of ZIB, *(II)* Considering the effect of ZIB, *(II)* Single Line Outage, *(IV)* Single Sensor Outage, and *(V)* Single Sensor/Line Outage. The effect of ZIB is considered in scenarios *III*, *IV*, and *V*.

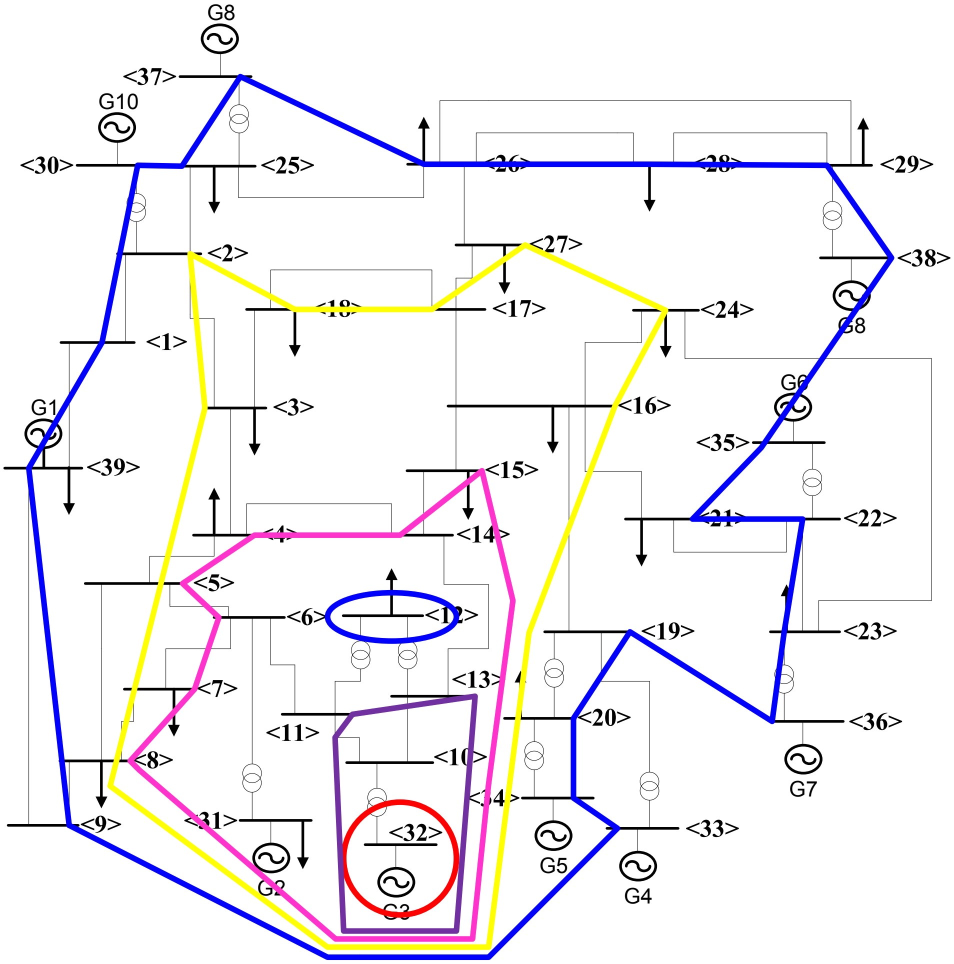

Figure 5.6: The fault contour map for generator outage at bus 32

5.3.1 OSSP and data volume reduction

In Table 5.11 and 5.12, the OSSP results in IEEE 30 and IEEE 39 bus systems are illustrated, respectively. The SG requires less number of sensors if the effect of ZIB is considered. If the scenarios of single sensor outage or single line outage are considered, more sensors are required for full observation of SG. From the OSSP results in Table 3.3 to 5.12, the *synchrophasor sensor installation rate*, which is defined as the ratio of the sensor number to the total number of buses, is 45%. And it can be noticed that, if the power system is larger, the *synchrophasor sensor* *installation rate* will be further decreased. In Fig. 5.7, in scenario II, the installation is the lowest and in scenario V is the highest.

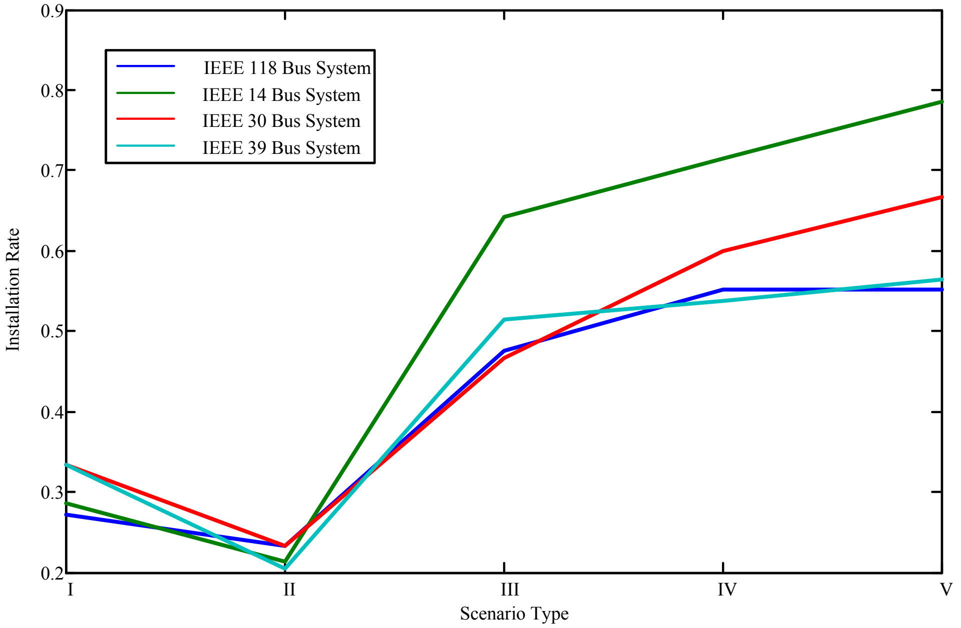

Figure 5.7: Synchrophasor installation rate in different scenarios

For a simulation period of 12 s, 12000 data samples are collected for system analysis [137]. After 30 MPD iterations for feature extraction, the 12000 data samples are extracted into 30 four-dimensional feature vectors $[\alpha, \tau, \nu, \sigma]^T$, with each representing the amplitude, time-shifting, frequency-shifting and variance of the Gaussian atoms. The total data number is $30 \times 4 = 120$, and the data compression rate, which is defined as the data volume generated by the spatial-temporal characterization to the original data volume, is 1.00%. Considering OSSP, for example, in Table 5.12 or in Fig. 5.7, with the IEEE 39-bus system and Scenario I, the sensor installation rate is 33.3%. Therefore, the total data compression rate can reach 0.33%, which substantially reduce the data volume of the synchrophasor measurement system.

Table 5.11: Comparison of OSSP results in IEEE 30-bus system

Type	Number	Location of Sensors	Rate
I	10	2, 4, 6, 9-10, 12, 15, 18, 25, 27	33.3%
II	7	2, 4, 10, 12, 15, 18, 27	23.3%
III	14	1, 4-5, 10-13, 15, 17-18, 20, 24, 26, 30	46.7%
IV	18	2-5, 7, 10, 12-13, 15-17, 19-20, 22-24, 27, 29	60.0%
V	20	2-5, 7, 10-13, 15-17, 19-20, 22-24, 26-27, 29	66.7%

Table 5.12: Comparison of OSSP results in IEEE 39-bus system

Type	Number	Location of Sensors	Rate
I	13	2, 6, 9-10, 13-14, 17, 19-20, 22-23, 25, 29	33.3%
II	8	3, 8, 10, 16, 20, 23, 25, 29	20.5%
III	17	3, 8, 16, 18, 23, 27-28, 30-39	51.5%
IV	21	2-3, 6, 8-10, 13, 16-17, 20, 22-23, 25-27, 29, 34, 36-39	53.8%
V	22	1, 3-4, 8, 16, 18, 20, 23, 25-27, 29-39	56.4%

5.3.2 Fault detection and identification

Six representative fault types are employed for evaluating the proposed characterization approach, which are generator ground, load loss, generator outage, single transmission line ground, and three-phase transmission line ground. The simulation of each fault lasts 5 s and the fault randomly occurs at 2, 2.5, 3, 3.5, and 4 s with duration for 5 and 10 cycles. The Gaussian atom dictionary is built with 1,800,000 Gaussian atoms and the MPD iteration number is 30. The discrete HMM employs an observation symbol set with 256 symbols and 3 hidden states. In this paper, 10 fold cross validation are selected; i.e., 90% of the generated data are used as the training data and 10% are used as the testing data. For evaluating fault detection performance, 240, 260 and 260 random faults are simulated to generate training and testing data in the IEEE 14-bus system, IEEE 30-bus system and IEEE 39-bus system, respectively. Similarly, for fault identification, 270, 350 and 350 random faults are simulated to generate training and testing data for the above three power systems, respectively. Among the aforementioned data, 90% of the data are used for training and 10% are used for testing. An additive white Gaussian noise (AWGN)

Table 5.13: Comparison of OSSP results in IEEE 118-bus system

Scenario Type	Number of Sensors	Location of Sensors	Installation Rate
I	32	3, 5, 9, 12, 15, 17, 21, 23, 28, 30, 34, 37, 40, 45, 49, 53, 56, 62, 64, 68, 71, 75, 77, 80, 85-86, 90, 94, 102, 105, 110, 115	27.1%
II	28	3, 8, 11-12, 17, 21, 27, 31-32, 34, 37, 40, 45, 49, 53, 56, 62, 72, 75, 77, 80, 85-86, 91, 94, 102, 105, 110	23.3%
III	56	1, 7, 10-12, 15, 17, 19, 21, 23-25, 27, 29, 32-34, 36, 40, 42, 44, 46, 49, 51, 53, 56-57, 59, 62, 66, 73-74, 77, 79, 83, 85, 87, 89, 91-92, 94, 96-101, 105-109, 111-112, 114, 116-118	47.5%
IV	65	1, 3, 6, 8-9, 11-12, 15, 17, 19, 21-24, 27, 29, 31-32, 34, 36-37, 40, 42, 44-46, 49-51, 53-54, 56, 59, 62, 66, 69-71, 75, 77-78, 80, 83, 85-87, 89, 91-92, 94, 96-101, 105-106, 109-112, 114, 117-118	55.1%
V	65	2-3, 6, 8, 10-12, 15, 17, 19, 21-22, 24-25, 27-28, 31-34, 36, 40, 42-43, 45-46, 49, 51-52, 54, 56-57, 59, 62, 66, 70, 73, 75-78, 80, 83, 85-87, 89-90, 92, 94, 96-101, 105-106, 109-112, 114, 116-117	55.1%

with SNR 10 dB is used for evaluating the performance with noisy measurements.

With synchrophasor sensors placed on every bus in the IEEE 14, 30, 39 ,and 118 bus systems, the results of the fault detection and identification rates are illustrated in Table 5.14 and Fig. 5.8. The fault identification curves in the same shape illustrates that the proposed method is stable and robust for different power systems in different scenarios. It is obviously that the fault identification rates in the scenarios without noise is higher than the fault identification rates with noise. The average detection rate is 100.0% and the average identification rate is 96.2%. Incorporating the OSSP results, the fault detection and identification rates are illustrated from

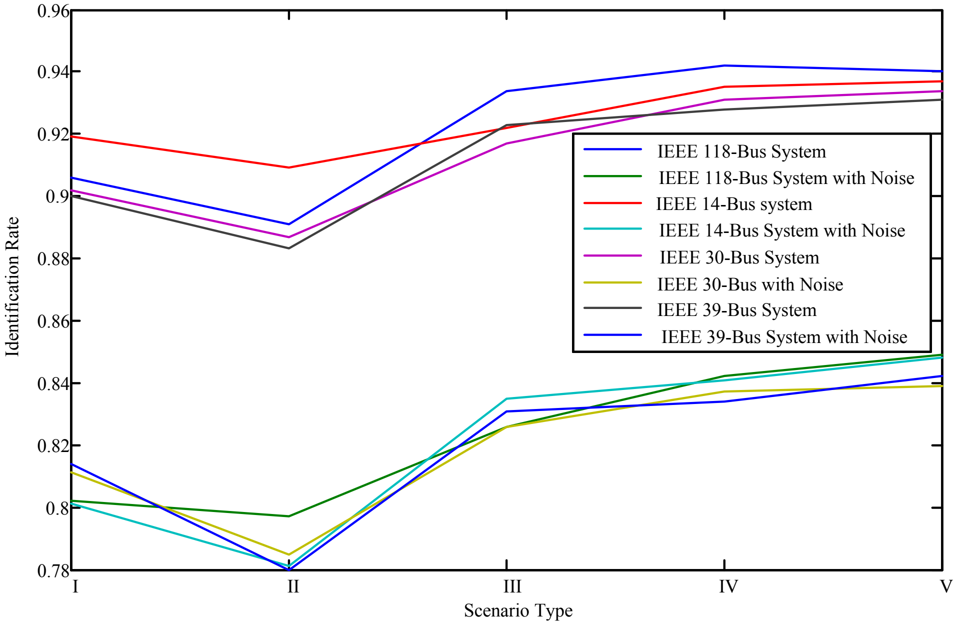

Figure 5.8: Fault identification rate in different systems and different scenarios

Table 5.15 to 5.21. The average detection rate is 100% for noiseless cases, and 99.3% with SNR 10 dB. The average identification rate is 91.9% for noiseless and 82.0% with SNR 10 dB. The noise has greater impact on fault identification rate than detection rate. The highest detection rate with OSSP is 100%, which is the same as the detection rate when the sensors are installed on every bus of the system. The highest identification rate with OSSP is 93.7%, which is close to the identification rate when the sensors are installed on every bus of the system.

Table 5.14: Fault detection and identification rates without OSSP

	Detection Rate	Identification Rate
IEEE 14 Bus System	100%(240/240)	96.3%(260/270)
IEEE 30 Bus System	100%(260/260)	95.7%(335/350)
IEEE 39 Bus System	100%(260/260)	96.6%(338/350)
IEEE 118 Bus System	100%(260/260)	97.1%(340/350)

Table 5.15: Fault detection and identification rates in IEEE 14-bus system

IEEE 14 Bus System	Detection Rate	Identification Rate
I	100%(240/240)	91.9%(245/270)
II	100%(240/240)	90.9%(245/270)
III	100%(240/240)	92.2%(249/270)
IV	100%(240/240)	93.5%(252/270)
V	100%(240/240)	93.7%(253/270)

Table 5.16: Fault detection and identification rates in IEEE 30-bus system

IEEE 30 Bus System	Detection Rate	Identification Rate
I	100%(260/260)	90.2%(316/350)
II	100%(260/260)	88.7%(310/350)
III	100%(260/260)	91.7%(321/350)
IV	100%(260/260)	93.1%(326/350)
V	100%(260/260)	93.4%(327/350)

Table 5.17: Fault detection and identification rates in IEEE 39-bus system

IEEE 39 Bus System	Detection Rate	Identification Rate
I	100%(260/260)	90.0%(315/350)
II	100%(260/260)	88.3%(309/350)
III	100%(260/260)	92.3% (323/350)
IV	100%(260/260)	92.8% (325/350)
V	100%(260/260)	93.1% (326/350)

Table 5.18: Fault detection and identification rates in IEEE 118-bus system

IEEE 118 Bus System	Detection Rate	Identification Rate
I	100%(260/260)	90.6%(317/350)
II	100%(260/260)	89.1%(312/350)
III	100%(260/260)	93.4% (327/350)
IV	100%(260/260)	94.2% (330/350)
V	100%(260/260)	94.0% (329/350)

Table 5.19: Detection and identification rates in IEEE 14-bus system with noise

IEEE 14 Bus System	Detection Rate	Identification Rate
I	98.8%(237/240)	80.1%(216/270)
II	97.5%(234/240)	78.1%(211/270)
III	100%(240/240)	83.5%(225/270)
IV	100%(240/240)	84.1%(227/270)
V	100%(240/240)	84.8% (229/270)

Table 5.20: Detection and identification rates in IEEE 30-bus system with noise

IEEE 30 Bus System	Detection Rate	Identification Rate
I	98.9%(257/260)	81.1%(284/350)
II	97.3%(253/260)	78.5%(275/350)
III	100%(260/260)	82.6%(289/350)
IV	100%(260/260)	83.7%(293/350)
V	100%(260/260)	83.9%(294/350)

Table 5.21: Detection and identification rates in IEEE 39-bus system with noise

IEEE 39 Bus System	Detection Rate	Identification Rate
I	98.9%(257/260)	81.4% (285/350)
II	98.1%(255/260)	78.0%(273/350)
III	100%(260/260)	83.1%(291/350)
IV	100%(260/260)	83.4%(292/350)
V	100%(260/260)	84.2%(295/350)

Table 5.22: Detection and identification rates in IEEE 118-bus system with noise

IEEE 118 Bus System	Detection Rate	Identification Rate
I	97.6%(254/260)	80.2% (281/350)
II	97.3%(253/260)	79.7%(279/350)
III	100%(260/260)	82.6%(289/350)
IV	100%(260/260)	84.2%(295/350)
V	100%(260/260)	84.9%(297/350)

5.3.3 Comparison with other methods

In [2, 8], artificial neural network (ANN) and support vector machine (SVM) are utilized to detect and diagnose faults in power systems. Using the same simulation as described at the beginning of Section 5.1, the fault detection rates and identification rates obtained using ANN, SVM, and our proposed approach are demonstrated in Table 5.23.

The proposed method performs better than the other two methods, especially in low SNR scenarios. On one hand, this illustrates that, under the condition of optimal FDR placement, the proposed approach is more robust than the other two methods. On the other hand, this fact also illustrates that the reduced number of FDRs impacts fault identification greatly due to the loss of useful information.

Table 5.23: Detection and identification rates of different methods with OSSP

	Detection	Identification	Identification 10 dB
ANN	92.7%	82.3%	71.3%
SVM	94.5%	84.2%	69.6%
Proposed Method	99.3%	91.9%	82.0%

5.4 A fast voltage security assessment approach for IEEE-39 Bus System

The IEEE-39 bus system is shown in Fig. 3.1. Because the IEEE 39-bus system is larger than the IEEE 14-bus system, the three-phase symmetrical fault will not heavily impact the whole power system.

In this condition, the criterion of voltage drop of the wind power plant's interconnection as the bus is that the voltage drop is below 80% of normal. Considering the nature hazards, the transmission lines between Bus 16 and 17, and Bus 25 and 26 are outaged. The numerical simulation of the proposed approach is illustrated in Table 5.24. To verify the results, the three-phase symmetrical fault is simulated in PowerWorld. The simulation results are illustrated in Table 5.25.

Comparing the result of the proposed approach to the dynamic simulation, the critical bus sets of the proposed approach contain the critical bus sets of the dynamic simulation in the normal scenario and transmission line outage scenario, respectively. Because the proposed approach does not contain all the elements of the relay protection, it is a conservative, but as additional basic dynamic information about the power system is available, the proposed approach will become more accurate.

Table 5.24: Voltage stability assessment with the proposed approach

Scenario Type	Voltage Impact Size	Critical Bus
Normal Condition	18 16 27 3 15 24 4 14 2 5 6 25 13 26 30 21 22 23 19 10 11 39 12 37 7 8 32 35 31 28 29 20 33 36 1 9 38 34	18 16 27 3 15 24 4 14 2 5 6 25 13 26 30 21 22 23 19 10
Transmission Line Outage	18 27 26 3 28 4 2 5 6 29 8 38 30 7 10 25 1 37 39 15 12 14 9 11 13 32 31 16 24 21 22 23 19 34 36 35 20 33	18 27 26 3 28 4 2 5 6 29 8 38 30 7 10 25 1 37

Table 5.25: Voltage stability assessment with the dynamic simulation

Scenario Type	Voltage Impact Size	Critical Bus
Normal Condition	18 27 16 24 15 3 21 26 22 23 2 19 14 4 25 30 20 33 35 13 12 28 10 11 5 6 37 7 8 34 36 29 31 32 1 9 38 39	18 27 16 24 15 3 21 26 22 23 2 19 14 4 25 30
Transmission Line Outage	27 18 26 28 3 29 2 38 30 25 37 4 1 8 31 5 7 39 6 12 14 9 11 13 10 32 15 16 24 20 21 33 34 23 19 22 35 36	27 18 26 28 3 29 2 38 30 25 37 4 1

5.5 Numerical results of renewable integration on the distribution system

The constraints on the control variables are shown in Table 5.26. All simulations are executed using a computer with an Intel i7 3.0 GHz CPU and 12 GB RAM, and the simulation software for the proposed approach is Matlab Simulink. The data length for the SVM to classify normal and abnormal conditions is 100 ms; the computation time for SVM is 20 ms; the computation time for MPC auxiliary control variables is 35 ms; and extra time consumption such as system delay is 10 ms. The resulting total consumption time is 165 ms.

Table 5.26: Constraints of the model predictive control variables

Lower Limits	Variable	Upper Limits
0.0 P.U.	$E_{AW1}, E_{AW2}, E_{AW3}$	1.2 P.U.
0°	$\beta_{AW1}, \beta_{AW2}, \beta_{AW3}$	30°
0.0 P.U.	V_6, V_9, V_{12}, V_{13}	1.5 P.U.

5.5.1 Model predictive control with LTI model

Wind Power Loss. In this study case, the switch Sw to load $L14$ is open, and the 1.5 MW load does not connect to the distribution system. As Fig. 5.9 illustrates, it is assumed that there are two different profiles of wind speed for the two WTGs, respectively. In order to create power margins for voltage regulation, deloaded WTGs operate at about 80% maximum available power.

As shown in Fig. 5.9, the blue curve and red curve illustrate the wind speed of WTG 1 and 2, which are connected to bus 9 and 12, respectively. At the beginning of the simulation, the wind speed is declining lightly from 1 s to 4 s, which causes the reduction of the output power of the WTGs. As shown in Fig. 5.10, the voltage curves are deviating lightly. Then, during time period 4 s to 7 s, the wind power is further decreasing, especially for the red curve. As a result, in Fig. 5.10, the voltage curve of bus 9 and 12 are deviating dramatically, especially for bus 12. Finally, at 6.7 s the voltage is below 0.4 p.u., thus indicating the failure of the distribution system.

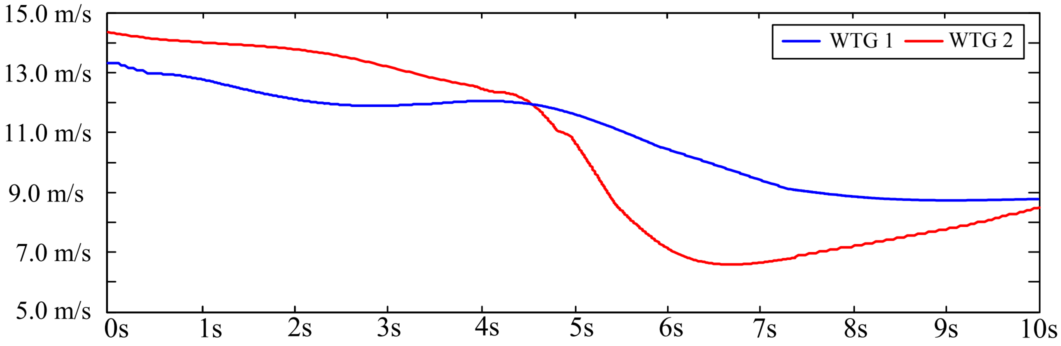

Figure 5.9: Wind speed of the two wind turbines

In order to remedy the situation presented in Fig. 5.10, the proposed approach is employed. At the beginning, the decreasing wind speeds cause the voltage deviation, and the auxiliary MPC is triggered immediately to compensate for voltage

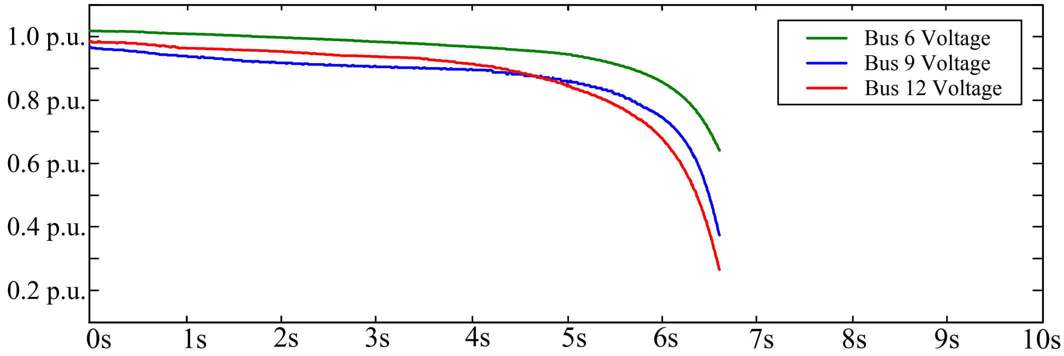

Figure 5.10: Voltage on bus 6, 9, and 12

reduction. The auxiliary MPC controlled pitch angle and excitation voltage variables are illustrated for the WTGs. In Fig. 5.11, the pitch angle curves of the two WTGs change to increase the output active power. As shown in Fig. 5.9, the wind speed of WTG 1 decreases more smoothly than the wind speed of WTG 2. As a result in Fig. 5.11, the MPC control pitch angle of WTG 1 also decreases smoothly than that of WTG 2. From $t = 4$ s, the MPC controlled pitch angles decreases acutely to generate more active power when the wind speed declines at the same time. In Fig. 5.12, the MPC controlled excitation voltage variables varies to generate appropriate reactive power and compensate for the voltage drop. The MPC controlled excitation voltage variable for WTG 2 is larger than WTG 1, which is used to compensate more reactive power for bus 12.

After the proposed method is employed, the improvement to bus voltages are shown in Fig. 5.13, and the voltage collapse is avoided. Since the proposed method is applied at the beginning to compensate the wind power loss, the voltage of the four buses is controlled within the range from 0.97 p.u. to 1.03 p.u. during $t = 1$ s to $t = 4$ s. As shown in Fig. 5.9, from $t = 4$ s to 7 s, the wind power dramatically deceases, as a result, the compensated voltages in Fig. 5.13 decline lightly; and the voltages are controlled within the range from 0.95 p.u. to 1.02 p.u.. It is noticed that the voltages collapsed during $t = 4$ s to 7 s in Fig. 5.10 if the proposed control

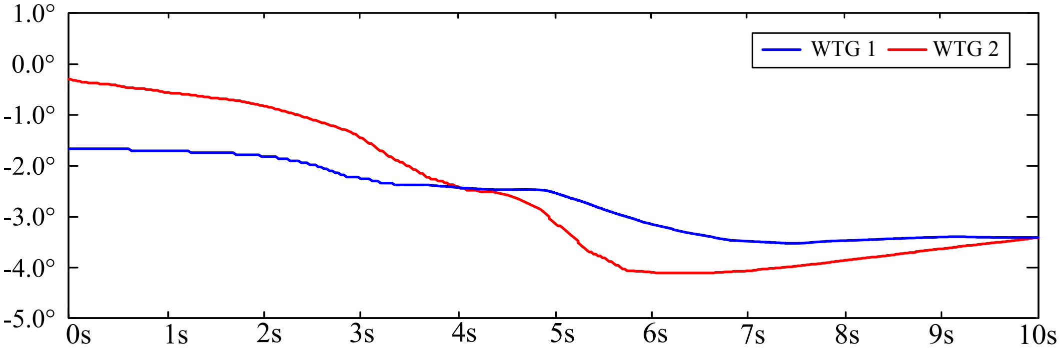

Figure 5.11: Proposed method for the auxiliary pitch angle variables

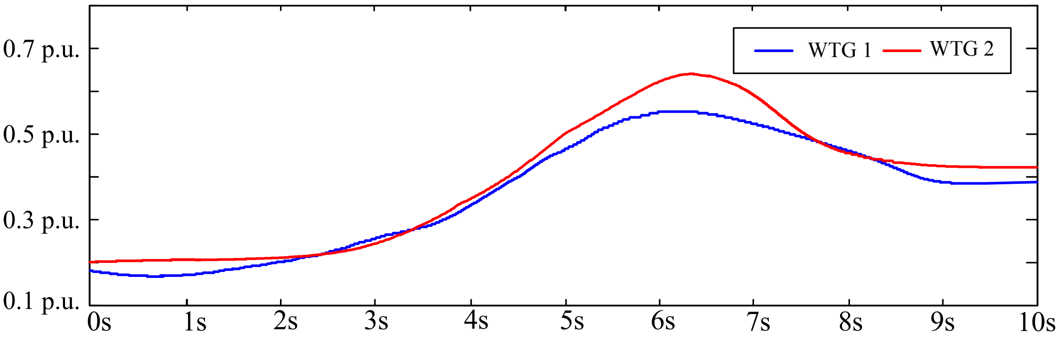

Figure 5.12: Proposed method for the auxiliary excitation voltage variables

strategy is not applied. In addition, the voltage curves of the four selected buses are more consistent with each others, and the voltage deviations are less than 2%.

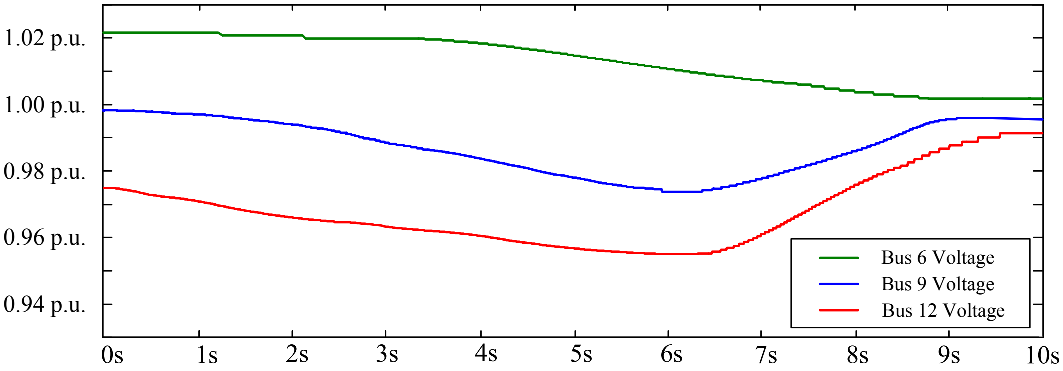

Figure 5.13: Voltage controlled by the proposed method.

5.5.2 Model predictive control with LTV Model

Load Switching. As shown in Fig. 4.2 illustrates, the switch *Sw* is open, and a 1.5 MW load is not connected to bus 6 and the distribution system operates in normal condition. At $t = 1$ s, the switch is closed to simulate the load contingency increased at bus 6. It is assumed that the wind speed is 14 m/s constantly.

As shown in Fig. 5.14, there are large voltage deviations in the three buses at time $t = 1$ s. From $t = 1.6$ s, the two WTGs try to recover the voltage loss caused by the load increasing. However, from $t = 4.5$ s, the voltages begin to decline, especially for the voltage curve of bus 6. This illustrates that the existed control strategy cannot recover the system from this fault condition. Finally, at $t = 7.8$ s, the voltage is below 0.55 p.u. indicating the failure of the system.

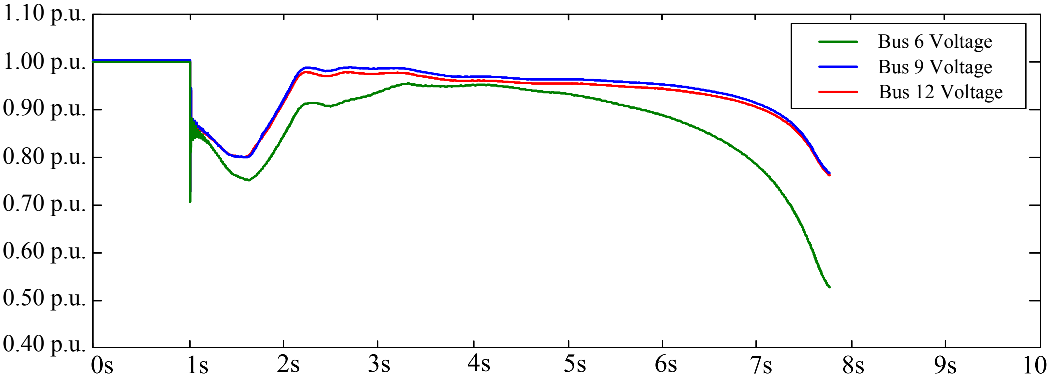

Figure 5.14: Voltage deviation caused by load switching

The proposed approach is employed for voltage stability in this scenario. After the fault occurs, it takes 165 ms for the SVM algorithm to predict the voltage disturbance and trigger the auxiliary MPC. Since the stable equilibrium point of the distribution system is changed, the state space model is rebuilt, and the auxiliary MPC is employed.

The WTGs auxiliary control variables computed by the MPC are illustrated. In Fig. 5.15, the pitch angle curves have a trough at first to generate more active power

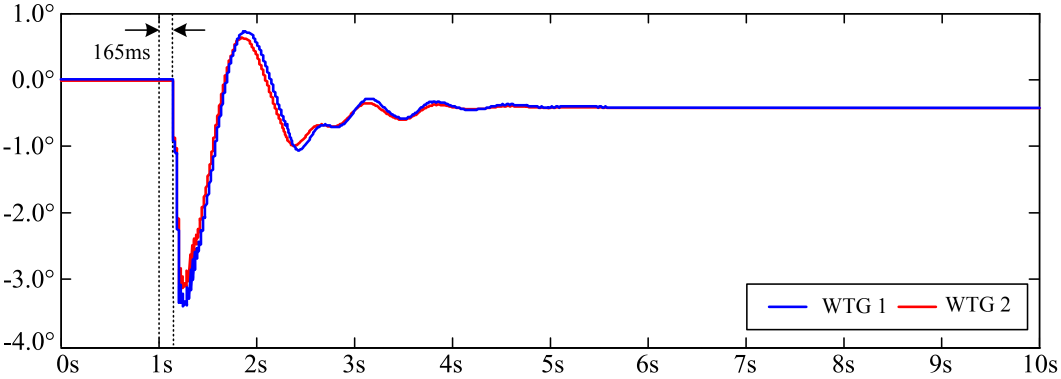

Figure 5.15: Proposed control method for the auxiliary pitch angle variables

to compensate for the increased load caused by the load switching. Meanwhile, in Fig. 5.16, besides the oscillation at the beginning, the excitation voltage curves of WTGs also have crests at first to compensate for the reactive power insufficient. Then both MPC controlled auxiliary pitch angle and excitation voltage variable curves show fast damped responses, which indicates that the auxiliary controller managed to quickly mitigate the voltage deviations.

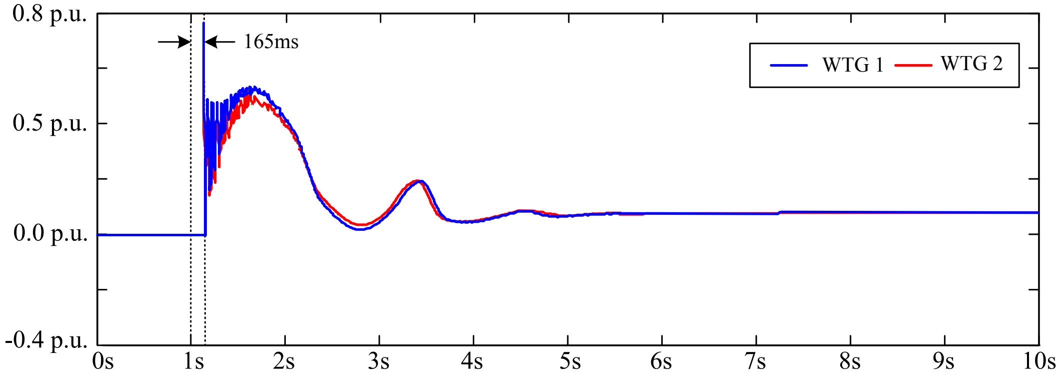

Figure 5.16: Proposed control method for the auxiliary excitation voltage variables

After the proposed method is employed, the voltage curves on selected buses are illustrated in Fig. 5.17. The large voltage deviations are under control in 5 seconds and the magnitude of deviation is reduced to less than 3% from $t = 5.5$ s.

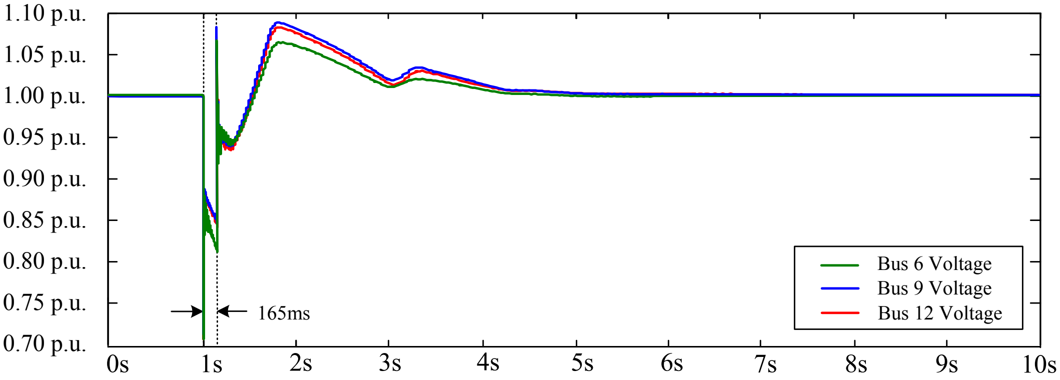

Figure 5.17: Voltage controlled by the proposed method after the load switching.

5.6 Numerical results of renewable integration on the transmission system

The constraints of the parameters are shown in Table 5.27. All simulations are executed using a computer with an Intel i7 3.0 GHz CPU and 12 GB RAM, and the simulation software for the proposed approach is Matlab Simulink. The data length for the SVM to classify normal and abnormal conditions is 100 ms; the computation time for SVM is 20 ms; the computation time for MPC auxiliary control variables is 35 ms; and 10 ms is for extra consumption such as system delay. The resulting total consumption time is 165 ms.

Table 5.27: Constraints of the model predictive control variables

Lower Limits	Variable	Upper Limits
0.0 P.U.	$E_{AG1}, E_{AG2}, E_{AG3}$	2.0 P.U.
0.0 P.U.	M_{A1}, M_{A2}, M_{A3}	1.2 P.U.
0.0 P.U.	$E_{AW1}, E_{AW2}, E_{AW3}$	1.2 P.U.
0°	$\beta_{AW1}, \beta_{AW2}, \beta_{AW3}$	30°
0.0 P.U.	V_1, V_3, V_6, V_{10}	1.5 P.U.

5.6.1 Model predictive control with LTI model

Wind Power Loss. In this study case, the switch Sw to generator G_3 is open, and the 1.5 MW TG does not connect to the hybrid power system. As Fig. 5.18 illustrates, it is assumed that there are two different profiles of wind speed for the two WTGs, respectively. In order to create power margins for voltage regulation, deloaded WPP operate at about 80% maximum available power.

At the beginning of the simulation, since the wind speed for WTG 1 is very low, the output power of the wind farm is insufficient. As Fig. 5.19 illustrates, there are the voltage curves on selected buses without the proposed auxiliary MPC approach. The blue curve illustrates the voltage of bus 6, which is connected to the WPP, is lower than voltages on other buses. Then, during time period 4 s to 7 s, the wind power is further decreased. As a result, in Fig. 5.19, the decrease in output power of the WPP causes the voltage decline of the power system. And at 7 s, the voltage is below 0.4 p.u., thus indicating the failure of the power system.

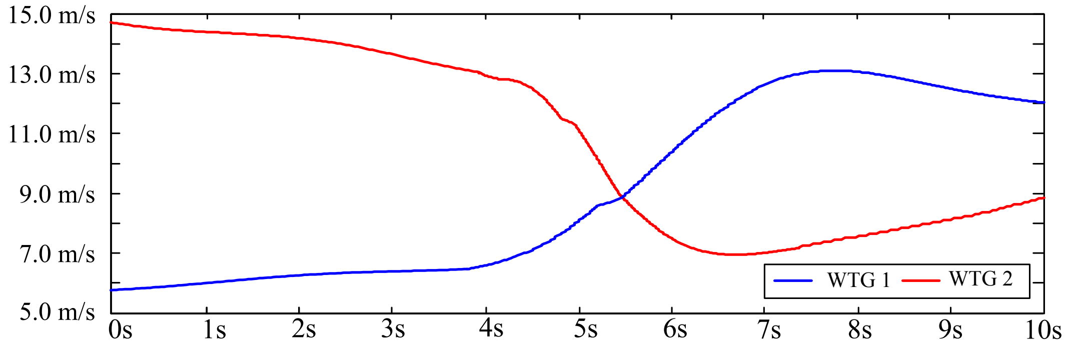

Figure 5.18: Wind speed of the wind turbines

In order to remedy the situation presented in Fig. 5.19, the proposed approach is employed. Since at the beginning, the low wind speed causes the voltage at bus 6 lower than others, the auxiliary MPC is triggered immediately to compensate for voltage reduction caused by the decreasing wind speed. The TG mechanical

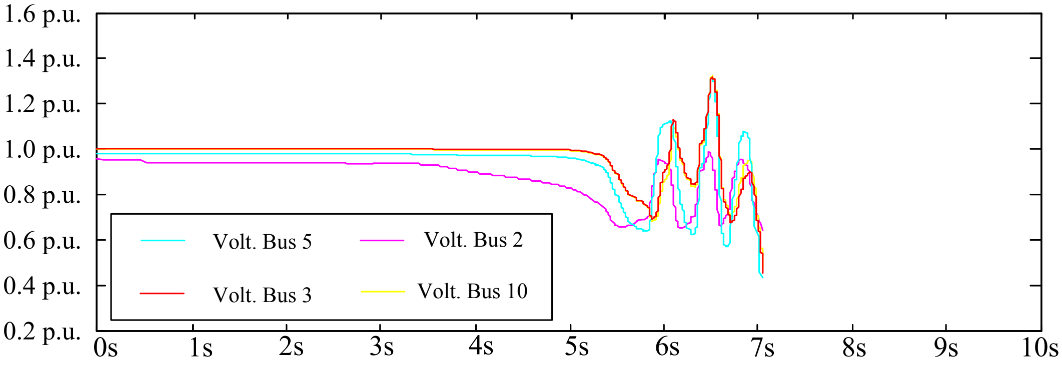

Figure 5.19: Voltage on bus 2, 3, 5, and 10

power increases to compensate the lack of generation as demonstrated in Fig. 5.20. Similarly the excitation voltage increases to provide reactive power support during the under voltage condition as shown in Fig. 5.21. Since TG 1 is located the closest to the IEEE 13-bus distribution grid, it has larger impact to compensate for the distribution grid output power drop. So the additional output of the TG 1 shows larger increase in mechanical and excitation voltage control variables. From t = 1.3 s to t = 9.0 s, there is an increase in the mechanical power and excitation to compensate for the power loss of the WPP.

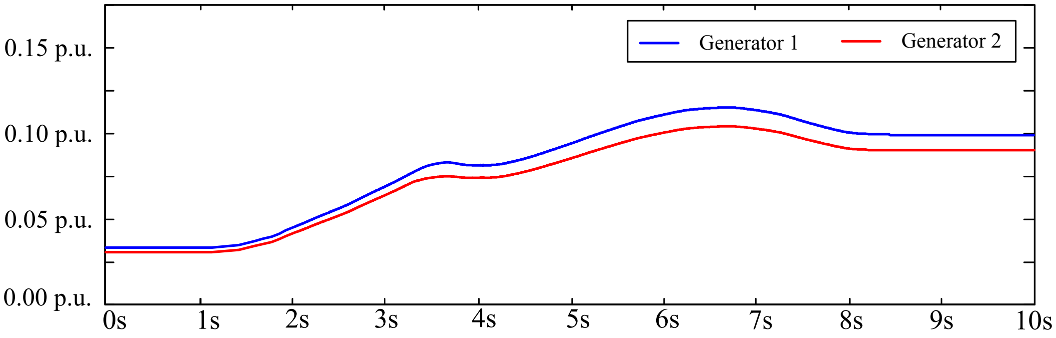

Figure 5.20: Proposed method for the auxiliary mechanical power variables

The auxiliary MPC controlled pitch angle and excitation voltage variables for the WTGs are illustrated as shown. In Fig. 5.22, the pitch angle curves of the two

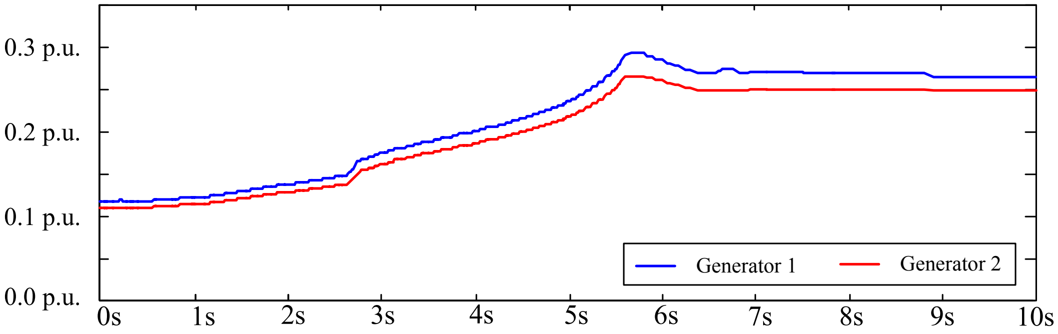

Figure 5.21: Proposed method for the auxiliary excitation voltage variables

WTGs change to increase the output active power. For WTG 1, the wind speed is low at the beginning, the MPC controlled pitch angle is low to generate more active power. For WTG 2, from $t = 4$ s, the MPC controlled pitch angles decreases acutely to generate more active power when the wind speed declines at the same time. In Fig. 5.23, there is a crest in control variables from $t = 1.3$ s to $t = 9.0$ s, the MPC controlled excitation voltage variables also increases to generate more reactive power and compensate for the voltage drop.

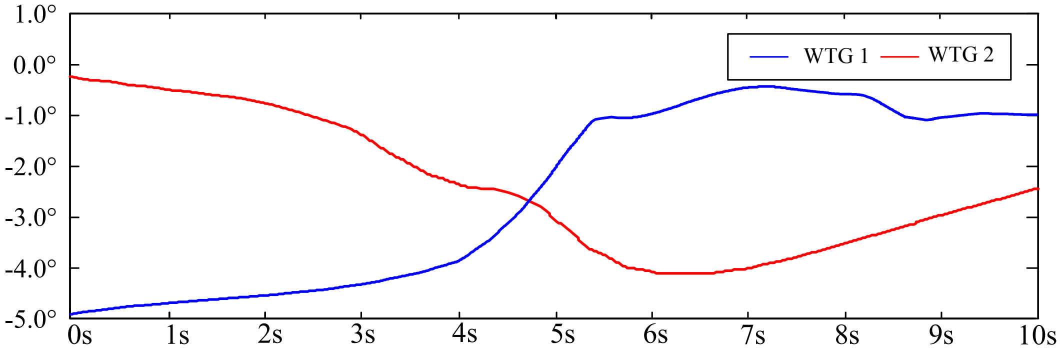

Figure 5.22: Proposed method for the auxiliary pitch angle variables

After the proposed method is employed, the improvement to bus voltages are shown in Fig. 5.24, and the voltage collapse is avoided. Since the proposed method is starting as the beginning to compensate the wind power loss, the voltage of the four

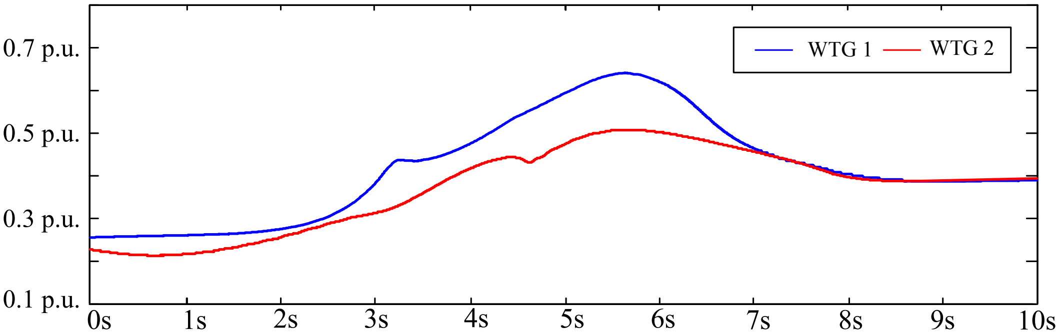

Figure 5.23: Proposed method for the auxiliary excitation voltage variables

buses is controlled in the range from 0.97 p.u. to 1.03 p.u.. As shown in Fig. 5.9, from $t = 4$ s to 7 s, the wind power dramatically deceases, the compensated voltages also decline lightly. But they are controlled in the range from 0.95 p.u. to 1.02 p.u. and beginning to coverage gradually, which is much better than the voltages collapsed in Fig. 5.10 without the proposed control strategy. Finally, the voltage curves of the four selected buses are more consistent with respect to each others, and the amplitude of the transient voltage dips are less than 2%.

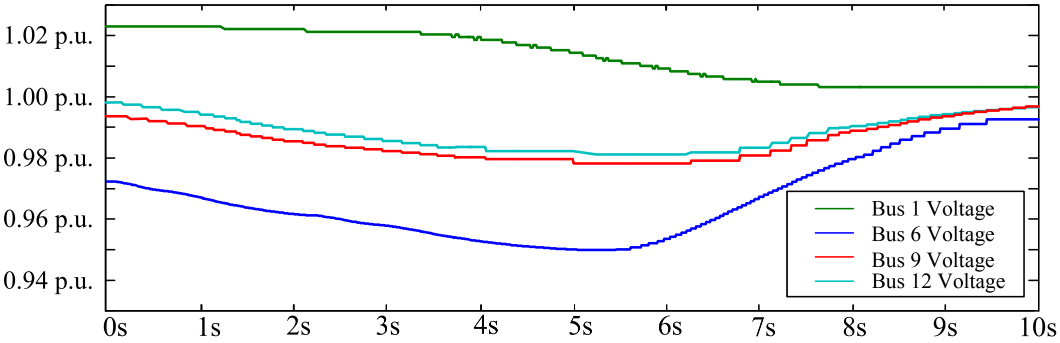

Figure 5.24: Voltage controlled by the proposed method for wind power loss

5.6.2 Model predictive control with LTV model

Generator Loss. As Fig. 4.2 illustrates, after the switch Sw is closed, a 1.5 MW traditional generator is connected at bus 14 and the power system operates in normal condition. At $t = 1$ s, a fault occurs and the switch is opened to simulate the loss of generation fault. It is assumed that the wind speed is 14 m/s constantly.

As shown in Fig. 5.25, there are large voltage oscillations in the four buses at the beginning. From $t = 1.3$ s, the TGs and WTGs try to recover the voltage loss caused by the generator loss. But from $t = 4$ s, the voltage becomes declining, especially for the green curve of bus 1, which is the nearest bus to the fault. This illustrates the existed control strategy cannot recover this fault condition. Finally, at $t = 7$ s, the voltage is below 0.5 p.u., and the simulation stops.

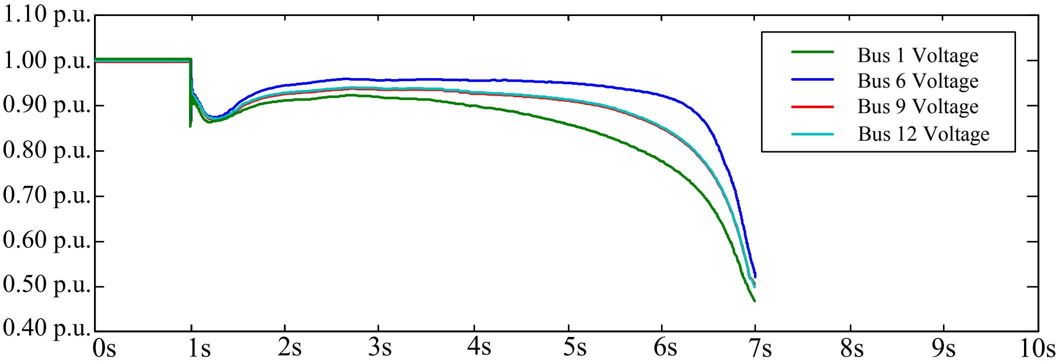

Figure 5.25: Voltage oscillation caused by generator loss

The proposed approach is employed for this scenario. After the fault occurs, it takes 165 ms for the SVM algorithm to predict that the voltage will be unstable and trigger the auxiliary MPC. Since the stable equilibrium point of the power system is changed, the state space model is rebuilt, and the auxiliary MPC is employed.

As illustrated below, the MPC computed TG auxiliary mechanical power variables have crests first to compensate for active power loss caused by the generator loss. In Fig.5.27, the excitation voltage variables have a lot of oscillations at the beginning to compensate for the voltage oscillation and also produce more reactive power to compensate for the reactive power loss. Because TG 1 is located closer with the fault than TG 2, the blue curves, which represent the mechanical power and excitation voltage of TG 1, have larger crests and troughs.

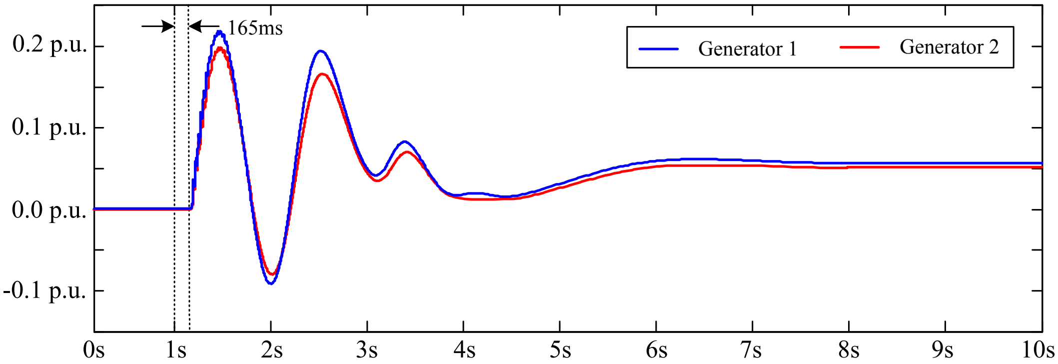

Figure 5.26: Proposed method for the auxiliary mechanical variables

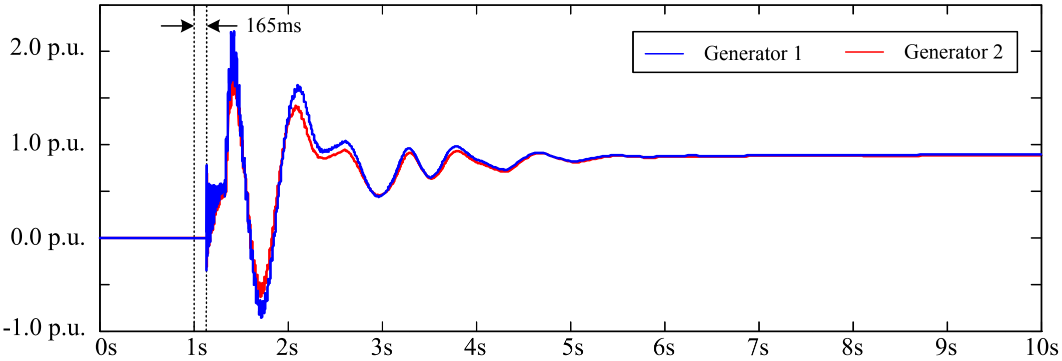

Figure 5.27: Proposed method for the auxiliary excitation voltage variables

The MPC computed auxiliary control variables of WTGs are illustrated as shown. In Fig.5.28, the pitch angle curves have trough at first to generate more active power to compensate for the active power loss caused by the generator loss.

Meanwhile, in Fig.5.29, besides the oscillation at the beginning, the excitation voltage curves of WTGs also have crest first to compensate for the reactive power loss. Then both MPC controlled auxiliary pitch angle and excitation voltage vari-

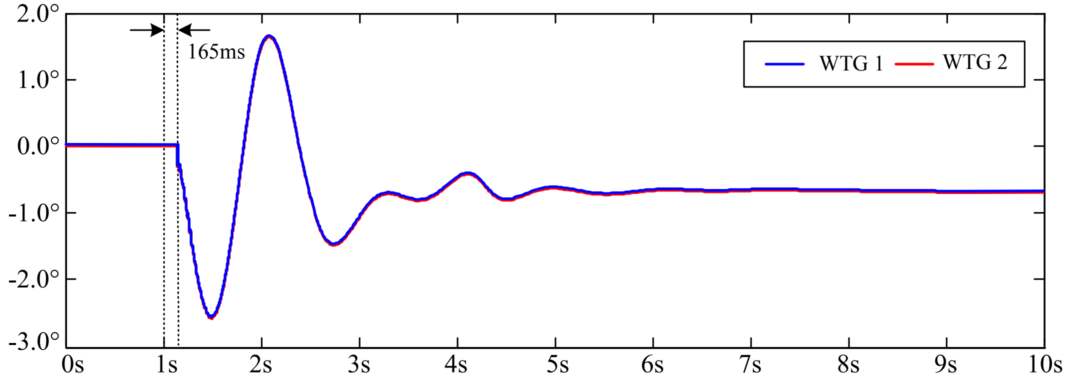

Figure 5.28: Proposed method for the auxiliary pitch angle variables

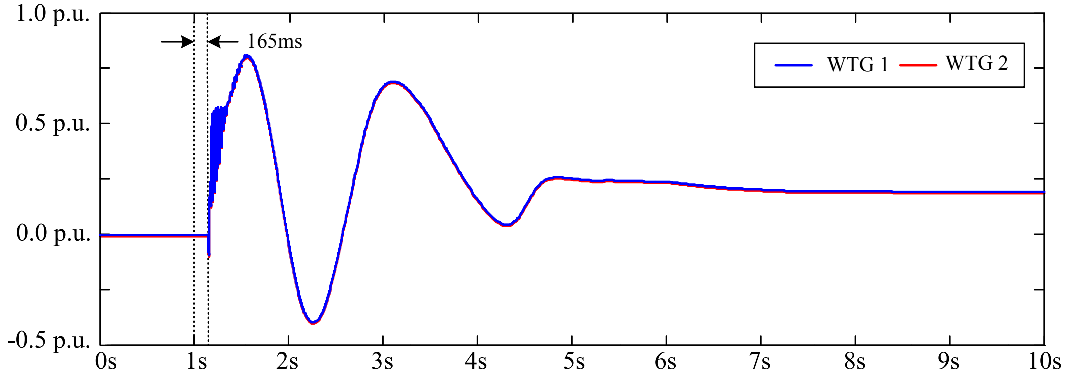

Figure 5.29: Proposed method for the auxiliary excitation voltage variables

able curves show to have fast damped responses, which indicates that the auxiliary controller managed to quickly mitigate the voltage oscillations.

After the proposed method is employed, the voltage curves on selected buses are illustrated as in Fig. 5.30. The large voltage oscillations are controlled in 5 seconds and the magnitude of oscillation is reduced to less than 3% from $t = 6$ s.

In sum, compared to traditional control strategies, distributed wind turbines act as an auxiliary control method to enhance voltage stability of the distribution system. In our proposed control strategy, the SVM classifier provides prediction of voltage stability. From our investigation, the impact of a reduced number of installed PMUs does not affect the accuracy and effectiveness of our proposed method. It

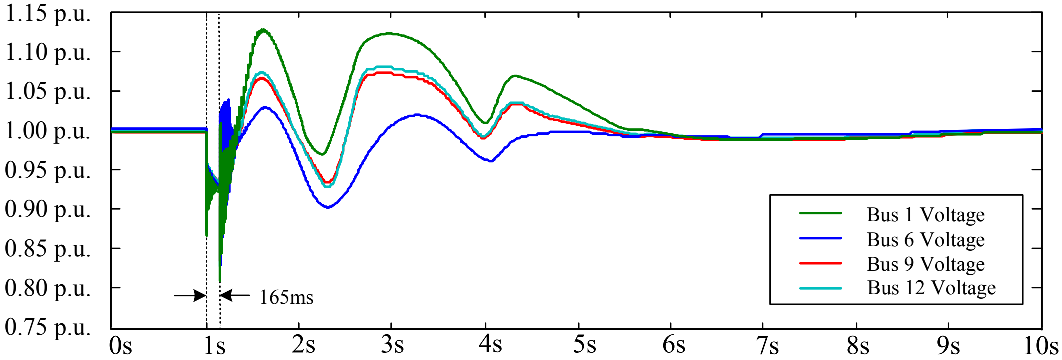

Figure 5.30: Voltage controlled by the proposed method for generator loss

is expected that our proposed auxiliary control strategy can be easily adapted to cooperate with existing voltage control methods and devices such as integrated volt/var control (IVVC) and voltage regulators.

5.7 Numerical results of statistical scheduling of economic dispatch

The numerical results of GA based optimization of the power operating cost are demonstrated. The proposed approach is applied to the IEEE 24-bus RTS, which is a hybrid power system and contains wind turbine generators. All the unit price data for the system, including the conventional energy and the renewable energy are from [33]. Sufficient historic data for training this model are provided by the National Renewable Energy Laboratory (NREL). The load demand range is assumed between 600 MWh to 2800 MWh, which is based on the rated power of each generator. In [135], the average worldwide wind penetration is around 17% in 2013. In this paper,it is assumed three levels in this paper for high wind energy penetration, 30%, 33.3% and 40%.

The objective function contain 28 variables, 14 for price per unit, 6 for conventional generating output power, 4 for wind turbine generator output power in spot market and 4 for wind turbine generator output power in reserve market. The effect of the uncertainty of the wind energy prediction on the power system operation will be studied on the IEEE 24-bus RTS model. Three case studies are conducted on this system.

In Case 1, results on the comparison of different wind penetration ratios are demonstrated. In Case 2, results are provided on three different α's in the chance constraint of (4.5.11). In the end, Monte Carlo simulation is conducted and used to test the reliability of the system.

5.7.1 Results on different wind energy penetrations ratios

A comparison of the effects of different wind energy penetration ratios is demonstrated in this section. The numerical study scenarios include the total operating cost of the power generation for three different wind penetration ratios with increasing load demand. In Fig. 5.31, with chance constraint probability $\alpha = 95\%$, the three different colours denote the results corresponding to three different wind penetration ratios. As we can see, the system with wind energy penetration in 40% provides the minimal cost with the same amount of generated power. It can be seen from Fig. 5.31 that, a lower wind energy penetration ratio results in higher power operating costs.

5.7.2 Results on different chance constraint probability

In Case 2, the wind energy penetration ratio is fixed as 33.3%, the chance constraint probability, α in (4.5.11), is defined as 90%, 95% and 99.73%, respectively. As shown in Fig. 5.32, the operating costs corresponding to the three different probabilities increase gradually with increasing load demand. As we can see in Fig. 5.32 that the operating cost with the probability of 99.73% is lower than others. The highest cost is obtained with the probability of 90%. This illustrates that the total

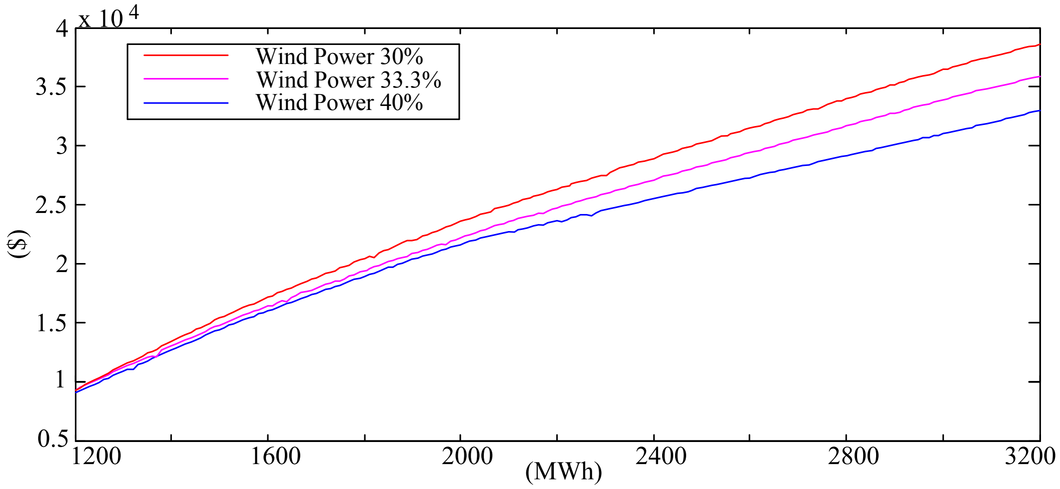

Figure 5.31: The total power operating costs of different wind energy penetrations

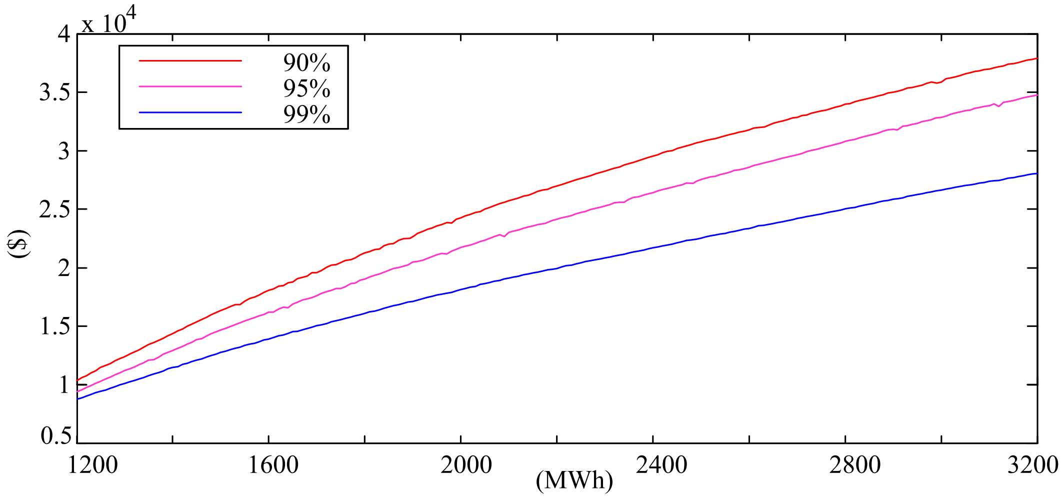

Figure 5.32: The total power operating cost with different chance constraints

power operating cost will change if the probability changes.

In detail, the total cost increases with decreasing chance constraint probability. This is due to that a larger probability places a stricter constraint that the total cost of the renewable energy needs to be lower or equal to the demand price b in (4.5.11). On the contrary, the operating cost increases if we define a smaller probability for the system, which means a weaker constraint is used for restricting the system. In sum, the proposed method provides an a robust and effective way to control the hybrid system in both transmission level and distribution level.

Chapter 6

Conclusion and future work

6.1 Conclusion

In the first decade of the twenty-one century, the world experienced the high speed increase in demand of electrical power and renewable energy penetration. The wide distributed synchrophasor sensors in the modern power systems can provide abundant data and information to analyze and control the hybrid power system. This provide a new method for wide area monitoring and renewable energy integration.

The wide area monitoring of power systems is the first step for renewable energy integration. In this paper, several approach are proposed for wide area monitoring. With the data collected by the wide distributed synchrophasor sensors, a time-frequency analysis approach is proposed for different types of faults in SGs. Wavelet analysis is used to extract signal edge features, then detect the fault. By clustering the signal edge features, the fault can be located in SG. This approach provides an effective way to detect and locate the fault in a short time.

An effective voltage security assessment is proposed to identify the locations that will have the greatest impact on the voltage at the wind power plants point of interconnection. Compared with the dynamic simulation, the proposed approach is more effective and requires fewer computations. With the present result, the proposed approach is conservative. But combined with the basic dynamic information, the proposed approach can be used to assess the voltage security for a wind power plant in power systems. The nature hazards, such as typhoon and earthquake, will change the parameters of power systems. If the parameters of power system are changed, the proposed approach provides a robust and feasible way to generate the critical bus set. The proposed approach enhances the voltage security and system resilience of power systems.

A novel data-driven method is proposed and studied which provides a multifunctional approach for fault detection, identification and location in SG systems. In addition, considering the economic issue of the proposed approach, the optimization placement of the distributed synchrophasor sensors is studied to reduce the number of the sensors without affecting accuracy and effectiveness of the proposed approach in the SGs. The detection rates and identification rates are also compared with other power system fault diagnosis methods such as ANN and SVM. The proposed method achieves the highest detection rates and identification rates for scenarios with different SNRs and reduced number of the distributed synchrophasor sensors. This indicates the robustness and implementation feasibility of the proposed approach considering the equipment and installation costs in real-world applications. Combining the SG topology information with the clustered features of voltage signals, the fault position can be inferred and located. Compared with the methods in [45, 99, 52, 53], the fault contour map proposed in this paper is very intuitive and the impacted areas can be located immediately after the fault happens.

It is our expectation that the proposed approach is able to provide prompt power system security assessment and fault diagnosis. It also helps to shorten response time for deciding the most effective protection actions such as switching generators, power system islanding and load shedding, etc. Based on the step of wide area power system monitoring, a novel auxiliary coordinated voltage control approach is proposed to improve the stability, reliability and efficiency of the renewable energy.

Compared with traditional control strategies, this proposed approach provides an effective way on transient voltage control for the power system with high wind penetration. In the proposed approach, the SVM classifier provides prediction of transient voltage stability. From our investigation the impact of reduced number of installed PMUs does not cause reduced accuracy and effectiveness of our proposed concept.

In addition to TG control loop and WTG control loop, a MIMO auxiliary coordinated control strategy based on the MPC algorithm is employed. This controller is dormant during normal operation, however, when there is a fault or other disturbances, the SVM classifier will trigger this controller action. Since there are many factors that can affect voltage stability in the system, the LTI and LTV system models are used to control the power system in different scenarios. In the numerical study, the proposed control strategy is demonstrated to be highly effective to control the voltage stability for the power system with high wind penetration on both the distribution system and the transmission system.

What is more, considering the high renewable energy penetration, a stochastic approach in joint scheduling economic dispatch has been presented. Compared to the Gaussian distribution, the Weibull distribution has a better performance in wind speed fitting. Based on the Weibull distribution, a probability chance constrain is derived into a feasible convex constrain. The valid optimization results demonstrate its effectiveness and efficiency.

With anticipated development of future power system, it can be predicted that small-scale wind turbine generators and PV panels will be pervasively located in distribution systems. Different from transmission systems, distribution systems are unbalanced and more complex such as one phase, two phase and three phase power system circuitry, which brings a challenge to power flow calculation. A graph theory based iterative approach is presented to analyze the distribution system first and then calculate the power flow.

In real-world applications, the power system is much more complicated than the test system and contains a variety of renewable energy sources such as photovoltaic, geothermal, etc. Therefore, we expect that our proposed approach to be a cornerstone for other applications that includes large scale renewable power system integration.

6.2 Future work

In the future work, the topic can be developed in details as follows:

6.2.1 Wide area monitoring

- Different types of fault, such as natural and man-made hazards, will be studied on fault detection, identification and location.
- In this paper, one fault occurred at a time is studied, multiple faults or cascading faults will be studied in the future.
- In this paper, the simulations are presented as the demonstrations of the presented monitoring approaches. In real application, more complex SG will be studied, which contains micro grid, high-voltage direct current (HVDC), etc.

6.2.2 Renewable energy integration control

- Besides voltage stability, power system stability contains frequency stability, phase angle stability, etc. In the next step, these areas will be modelled and researched.

- Because the distributed renewable energy can be located in many places of the power system, their parallel cooperation will be studied in the next step.

- In real application, the renewable energy contains solar energy, geothermal energy, etc. These issue will be taken into the consideration for future research.

6.2.3 Resilience of SG with renewable energy

- The areas will be studied that the voltage, frequency and phase angle stability of SG with different types of renewable energy.

- The natural and man-made hazards can change the topology of SG. The stability of SG under time-variant topology scenario will be a changeling topic for next step study.

- Considering the economic issue, how to manage the renewable energy, conventional energy, and power flow is a interesting topic for next step study.

6.2.4 Stochastic scheduling of economic dispatch

- Optimizing the total power cost for on emergency event, such as natural and man-made hazards.

- For real-world applications, various types of wind turbine generators should be considered to establish accuracy correlative function between wind speed and electrical power.

- IEEE 24-bus RTS is used in this paper to simulate and detect the results of the proposed model, more complex models will be chosen to validate the proposed approach in a large-scale power system.

6.2.5 Power flow of distribution system

- For real-world applications, the topology and system configuration are more complex, which brings higher requirements to the algorithm.
- The 12-bus distribution system is used as a test bench, however, more complex models will be chosen to validate the proposed approach in a large-scale power system.

6.3 Publications

6.3.1 Journal articles

1. **H. Jiang**, J.J. Zhang, D.W. Gao, and Z. Wu, "Fault Detection, Identication and Localization in Smart Grid Based on Data-Driven Computational Methods," *IEEE Transactions on Smart Grid*, 2014, accepted.
2. **H. Jiang**, Y. Zhang, J.J. Zhang, D.W. Gao, and E. Muljadi, "Synchrophasor Based Auxiliary Controller to Enhance Voltage Stability of Distribution System with a High Penetration Renewable Energy," *IEEE Transactions on Smart Grid Special Issue on Monitoring, Visualizaton, and State Estimation for Distribution Systems*, 2014, accepted.
3. Wei Shi, Huang Lei, Jian Xu, Yi Gu, **H. Jiang**, J.J. Zhang, "Fault Analysis in Big Data Situation with Optimal PMU Placement", Proceedings of the Chinese Society for Electrical Engineering, 2014, accepted.
4. Mahesh K. Banavar, J.J. Zhang, **H. Jiang**, Chaitali Chakrabarti, Antonia Papandreou-Suppappola, Andreas Spanias, Cihan Tepedelenlioglu, "Review of Sensor Signal and Information Processing Algorithms", Digital Signal Processing, 2013, accepted.

5. M. Cui, J. Zhang, AR. Florita, Bri. Hodge, **H. Jiang**, D. Ke and Y. Sun, Wind Power Ramp Event Detection Based on an Optimized Swinging Door Algorithm, IEEE Transactions on Power System, in preparation.

6.3.2 Conference proceedings papers

1. **H. Jiang**, Y. Zhang, J. Zhang, E. Muljadi, PMU-Aided Voltage Security Assessment for a Wind Power Plant, IEEE Power and energy Society General Meeting, 2015, submitted.
2. Y. Gu, **H. Jiang**, Y. Zhang and D.W. Gao, "Statistical Joint Scheduling of Economic Dispatch and Energy Reserves of Hybrid Power Systems with High Renewable Energy Penetration," Asilomar Conference on Signals, Systems, and Computers, 2014, accepted.
3. **H. Jiang**, L. Huang, J.J. Zhang, Y. Zhang and D.W. Gao, " Spatial-Temporal Characterization of Synchrophasor Measurement Systems — A Big Data Approach for Smart Grid System Situational Awareness," Asilomar Conference on Signals, Systems, and Computers, 2014, accepted.
4. **H. Jiang**, Y. Zhang, J.J. Zhang, D.W. Gao, and E. Muljadi, "Synchrophasor Based Auxiliary Controller to Enhance Power System Transient Voltage Stability in a High Penetration Renewable Energy Scenario," IEEE Symposium on Power Electronics and Machines for Wind and Water Applications 2014, accepted.
5. **H. Jiang**, J.J. Zhang, A. Hebb, M.H. Mahoor "Time-frequency Analysis of Brain Electrical Signals for Behaviour Recognition in Patients with Parkinson's Disease", Asilomar Conference on Signals, Systems, and Computers, 2013.

6. **H. Jiang**, J.J. Zhang, and Y.C. Zhang “Data-Driven Diagnosis and Control Methods in Smart Grid”, Fifth Annual Green Technologies Conference, 2013
7. **H. Jiang**, J.J. Zhang, W. Gao, “Fault Localization in Smart Grid Using Wavelet Analysis and Unsupervised Learning,” Asilomar Conference on Signals, Systems, and Computers, 2012.

Bibliography

[1] *A tutorial on hidden Markov models and selected applications in speech recognition*, 1989.

[2] Raj Aggarwal and Yonghua Song. Artificial neural networks in power systems. iii. examples of applications in power systems. *Power Engineering*, 12:279–287, 1998.

[3] Mohammad Reza Aghamohammadi and Ali Shahmohammadi. Intentional islanding using a new algorithm based on ant search mechanism. *International Journal of Electrical Power & Energy Systems*, 35, 2012.

[4] Paul M. Anderson and A. A. Fouad. *Power System Control and Stability*. Wiley-IEEE Press, 2002.

[5] Kiam Heong Ang, Gregory Chong, and Yun Li. PID control system analysis, design, and technology. *IEEE Transactions on Control Systems Technology*, 13:559–576, 2005.

[6] Ali Aref, Mohsen Davoudi, Farzad Razavi, and Majid Davoodi. Optimal DG placement in distribution networks using intelligent systems. *Energy and Power Engineering*, 4:92–98, 2012.

[7] Karl J. Astrom and Tore Hagglund. *PID Controllers: Theory, Design, and Tuning*. ISA: The Instrumentation, Systems, and Automation Society, 1995.

[8] Peter G. V. Axelberg, Irene Yu-Hua Gu, and Math H. J. Bollen. Support vector machine for classification of voltage disturbances. *IEEE Transactions on Power Delivery*, 22:1297–1303, 2007.

[9] K. Bae and J. S. Thorp. An importance sampling application: 179 bus WSCC system under voltage based hidden failures and relay misoperation. *Proceeding of the Thirty-First Hawaii International Conference on System Sciences*, 3:39–46, 1998.

[10] R. Barth, H. Brand, P. Meibom, and C. Weber. A stochastic unit-commitment model for the evaluation of the impacts of integration of large amounts of intermittent wind power. In *Probabilistic Methods Applied to Power Systems*, 2006.

[11] A Berizzi, P Bresesti, P Marannino, G Granelli, and M Montagna. System-area operating margin assessment and security enhancement against voltage collapse. *IEEE Transactions on Power Systems*, 11(3):1451–1462, 1996.

[12] A Berizzi, P Finazzi, D Dosi, P Marannino, and S Corsi. First and second order methods for voltage collapse assessment and security enhancement. *IEEE Transactions on Power Systems*, 13(2):543–551, 1998.

[13] Alberto Berizzi, Paolo Marannino, Marco Merlo, Massimo Pozzi, and Fabio Zanellini. Steady-state and dynamic approaches for the evaluation of loadability margins in the presence of secondary voltage regulation. *IEEE Transactions on Power Systems*, 19(2):1048–1057, 2004.

[14] T.S. Bi, X.N. Song, X.N. Wu, and Q.X. Yang. Novel method for disturbance identification in power systems. In *IEEE Power Engineering Society General Meeting*, 2006.

[15] Zhengjun Bi and Changzheng Gao. Power system dynamic voltage stability analysis considering wind power. In *2014 IEEE 12th International Conference on Dependable, Autonomic and Secure Computing (DASC)*, pages 129–132. IEEE, 2014.

[16] Ruddy Blonbou. Very short-term wind power forecasting with neural networks and adaptive bayesian learning. *Renewable Energy*, 36(3):1118–1124, 2011.

[17] E Bompard, Enrico Carpaneto, Gianfranco Chicco, and Roberto Napoli. Convergence of the backward/forward sweep method for the load-flow analysis of radial distribution systems. *International journal of electrical power & energy systems*, 22(7):521–530, 2000.

[18] Anjan Bose. Smart transmission grid applications and their supporting infrastructure. *IEEE Transcations on Smart Grid*, 1:11–19, 2010.

[19] Sukumar M. Brahma and Adly A. Girgis. Fault location on a transmission line using synchronized voltage measurements. *IEEE Transactions on Power Delivery*, 19:1619–1622, 2004.

[20] Barbara G Brown, Richard W Katz, and Allan H Murphy. Time series models to simulate and forecast wind speed and wind power. *Journal of climate and applied meteorology*, 23(8):1184–1195, 1984.

[21] CJC. Burges. *A Tutorial on Support Vector Machines for Pattern Recognition.* Kluwer Academic Publishers, 1998.

[22] A. Bykhovsky and J.H. Chow. Power system disturbance identification from recorded dynamic data at the Northfield substation. *International Journal of Electrical Power and Energy Systems*, 25:787–795, 2003.

[23] Yixin Cai, Mo-Yuen Chow, Wenbin Lu, and Lexin Li. Statistical feature selection from massive data in distribution fault diagnosis. *IEEE Transaction on Power Systems*, 25:642–648, 2010.

[24] Vito Calderaro, Christoforos N. Hadjicostis, Antonio Piccolo, and Pierluigi Siano. Failure identification in smart grids based on Petri Net modeling. *IEEE Transactions on Industrial Electronics*, 58:4613–4623, 2011.

[25] M. Carrin and J. M. Arroyo. A computationally efficient mixed-integer linear formulation for the thermal unit commitment problem. *IEEE transaction on power systems*, 21:1371–1378, 2006.

[26] Ali Naci Celik. A statistical analysis of wind power density based on the weibull and rayleigh models at the southern region of turkey. *Renewable energy*, 29(4):593–604, 2004.

[27] Debejyo Chakraborty, Narayan Kovvali, Jun Wei, Antonia Papandreou-Suppappola, Douglas Cochran, and Aditi Chattopadhyay. Damage classification structural health monitoring in bolted structures using time-frequency techniques. *Journal of Intelligent Material Systems and Structures*, 20:1289–1305, 2009.

[28] Madhusudan Chakraborty and Debapriya Das. Voltage stability analysis of radial distribution networks. *Electrical Power and Energy Systems*, 23:129135, 2001.

[29] GW Chang, SY Chu, and HL Wang. An improved backward/forward sweep load flow algorithm for radial distribution systems. *IEEE Transactions on Power Systems*, 22(2):882–884, 2007.

[30] T-H Chen, Mo-Shing Chen, K-J Hwang, Paul Kotas, and Elie A Chebli. Distribution system power flow analysis-a rigid approach. *IEEE Transactions on Power Delivery*, 6(3):1146–1152, 1991.

[31] Michael Chertkov, Feng Pan, and Mikhail G. Stepanov. Predicting failures in power grids: the case of static overloads. *IEEE Transcations on Smart Grid*, 2:162–172, 2011.

[32] Badrul H Chowdhury and Carson W Taylor. Voltage stability analysis: VQ power flow simulation versus dynamic simulation. *IEEE Transactions on Power Systems*, 15(4):1354–1359, 2000.

[33] R. Christie. Power system test archive. *http://www.ee.washington.edu/research/pstca.*, 1999.

[34] Kara Clark, Nicholas W. Miller, and Juan J. Sanchez-Gasca. *Modeling of GE wind turbine-generators for grid studies.* GE Energy, 2008.

[35] T. M. Cover and P. E. Hart. Nearest neighbor pattern classification. *IEEE Transactions on Information Theory*, 13:21–27, 1967.

[36] IBM ILOG CPLEX. V12. 1: Users manual for cplex. *International Business Machines Corporation*, 46:157, 2009.

[37] B.V. Dasarathy. *Nearest Neighbor: Pattern Classification Techniques.* IEEE Computer Society Press, 1990.

[38] R. Datta and V. T. Ranganathan. Variable-speed wind power generation using doubly fed wound rotor induction machinea comparison with alternative schemes. *IEEE transactions on energy conversion*, 17:414–421, 2002.

[39] E. A. DeMeo, W. Grant, M. R. Milligan, and M. J. Schuerger. Wind plant integration. *IEEE Power & Energy Magazine*, 05:38–46, 2005.

[40] Y. Ding and P. Wang. Reliability and price risk assessment of a restructured power system with hybrid market structure. *IEEE transaction on power systems*, 21:108–116, 2006.

[41] Jingyuan Dong, Jian Zuo, Lei Wang, Kyung Soo Kook, Il-Yop Chung, Yilu Liu, Sandra Affare, Bruce Rogers, and Michael Ingram. Analysis of power system disturbances based on wide-area frequency measurements. *IEEE Power Engineering Society General Meeting, 2007*, pages 1–8, 2007.

[42] Abdelsalam A. Eajal and M. E. El-Hawary. Optimal capacitor placement and sizing in unbalanced distribution systems with harmonics consideration using particle swarm optimization. *IEEE Transaction on Power Delivery*, 25:1734–1741, 2010.

[43] Xi Fang, Satyajayant Misra, Guoliang Xue, and Dejun Yang. Smart grid - the new and improved power grid: a survey. *IEEE Communications Surveys and Tutorials*, 14:944–980, 2012.

[44] Marek Fisz. *Probability Theory and Mathematical Statistics*. New York: Wiley, 1963.

[45] W. Gao and J. Ning. Wavelet-based disturbance analysis for power system wide-area monitoring. *IEEE Transactions on Smart Grid*, 2:121–130, 2011.

[46] Adly A. Girgis, Christopher M. Fallon, and David L. Lubkeman. A fault location technique for rural distribution feeders. *IEEE Transactions on Industry Applications*, 29:1170–1175, 1993.

[47] Francisco R. Gomez, Athula D. Rajapakse, Udaya D. Annakkage, and Ioni T. Fernando. Support vector machine-based algorithm for post-fault transient stability status prediction using synchronized measurements. *IEEE Transactions on Power Systems*, 26:1474 – 1483, 2011.

[48] H.B. Gooil, D.P. Mendes, K.R.W. Bell, and D.S. Kirschen. Optimal scheduling of spinning reserve. *IEEE Transactions on Power Systems*, 14:1485–1492, 1999.

[49] SK Goswami and SK Basu. Direct solution of distribution systems. In *Generation, Transmission and Distribution, IEE Proceedings C*, volume 138, pages 78–88. IET, 1991.

[50] Bei Gou. Generalized integer linear programming formulation for optimal PMU placement. *IEEE Transactions on Power Systems*, 23, 2008.

[51] ND Hatziargyriou, GC Contaxis, and NC Sideris. A decision tree method for on-line steady state security assessment. *IEEE Transactions on Power Systems*, 9(2):1052–1061, 1994.

[52] M. He and J. Zhang. Fault detection and localization in smart grid: a probabilistic dependence graph approach. *IEEE Smart Grid Communcation*, pages 43–48, 2010.

[53] Miao He and Junshan Zhang. A dependency graph approach for fault detection and localization towards secure smart grid. *IEEE Transactions on Smart Grid*, 2:342–351, 2011.

[54] H. Heinz. Parallel genetic algorithms, population genetics and combinatorial optimization. *Parallelism, Learning, Evolution*, pages 398–406, 1991.

[55] H. Heinz, M. Schomisch, and B. Joachim. The parallel genetic algorithm as function optimizer. *Parallel computing*, 17:619–632, 1991.

[56] John Hetzer, David C Yu, and Kalu Bhattarai. An economic dispatch model incorporating wind power. *IEEE Transactions on Energy Conversion*, 23(2):603–611, 2008.

[57] T.A. Hoang and D.T. Nguyen. Matching pursuit for the recognition of power quality disturbance. *IEEE 33rd Annual Power Electronics Specialists Conference*, 4:1791 – 1796, 2002.

[58] Lei Huang, Yuanzhang Sun, Jian Xu, Wenzhong Gao, Jun Zhang, and Ziping Wu. Optimal PMU placement considering controlled islanding of power system. *IEEE Transactions on Power Systems*, 29:742–755, 2014.

[59] D. Ibrahim. Renewable energy and sustainable development: a crucial review. *Renewable and Sustainable Energy Reviews*, 4:157–175, 2000.

[60] Suresh H Jangamshetti and V Guruprasada Rau. Normalized power curves as a tool for identification of optimum wind turbine generator parameters. *IEEE Transactions on Energy Conversion*, 16(3):283–288, 2001.

[61] B Jeyasurya. Artificial neural networks for power system steady-state voltage instability evaluation. *Electric power systems research*, 29(2):85–90, 1994.

[62] Huaiguang Jiang, Jun J Zhang, Wenzhong Gao, and Ziping Wu. Fault detection, identification, and location in smart grid based on data-driven computational methods. *IEEE Transactions on Smart Grid*, 5:2947 – 2956, 2014.

[63] Huaiguang Jiang, Jun Jason Zhang, and David W. Gao. Fault localization in smart grid using wavelet analysis and unsupervised learning. *2012 Conference Record of the Forty Sixth Asilomar Conference on Signals, Systems and Computers (ASILOMAR)*, pages 386–390, 2012.

[64] CG Justus, WR Hargraves, Amir Mikhail, and Denise Graber. Methods for estimating wind speed frequency distributions. *Journal of applied meteorology*, 17(3):350–353, 1978.

[65] Daniel Karlsson, Morten Hemmingsson, and Sture Lindahl. Wide area system monitoring and control-terminology, phenomena, and solution implementation strategies. *IEEE Power and Energy Magazine*, 2(5):68–76, 2004.

[66] Vojislav Kecman. *Support Vector Machines, Neural Networks, and Fuzzy Logic Models*. The MIT Press, 2001.

[67] M. Kezunovic. Automated fault analysis in a smart grid. *Transmission and Distribution Conference and Exposition: Asia and Pacific*, pages 1–3, 2009.

[68] Mladen Kezunovic, Le Xie, and Santiago Grijalva. The role of big data in improving power system operation and protection. In *Bulk Power System Dynamics and Control-IX Optimization, Security and Control of the Emerging Power Grid (IREP), 2013 IREP Symposium*, pages 1–9. IEEE, 2013.

[69] Ravindra Kollu, Srinivasa R Rayapudi, SVL Narasimham, and Krishna M Pakkurthi. Mixture probability distribution functions to model wind speed distributions. *International Journal of Energy and Environmental Engineering*, 3(1):27, 2012.

[70] George N. Korres, Peter J. Katsikas, Kevin A. Clements, and Paul W. Davis. Numerical observability analysis based on network graph theory. *IEEE Transactions on Power Systems*, 18:1035–1045, 2003.

[71] Samir Kouro, Patricio Corts, Ren Vargas, Ulrich Ammann, and Jos Rodrguez. Model predictive control-a simple and powerful method to control power converters. *IEEE Transactions on Industrial Electronics*, 56:1826–1838, 2009.

[72] K.S.Swarup and H.S.Chandrasekharaiah. Fault detection and diagnosis of power systems using artificial neural networks. *Proceedings of the First International Forum on Applications of Neural Networks to Power Systems*, pages 102–106, 1991.

[73] Prabha Kundur. *Power System Stability and Control.* McGraw-Hill Professional, 1994.

[74] Huibert Kwakernaak and Raphel Sivan. *Linear Optimal Control Systems.* Wiley-Interscience, 1972.

[75] P. Lagonotte, J.C. Sabonnadiere, J.Y. Leost, and J.P. Paul. Structural analysis of the electrical system: application to secondary voltage control in France. *IEEE Transactions on Power Systems*, 4, 1989.

[76] Mats Larsson and Daniel Karlsson. Coordinated system protection scheme against voltage collapse using heuristic search and predictive control. *IEEE Transactions on Power Systems*, 18:1001–1006, 2003.

[77] Fangxing Li, Wei Qiao, Hongbin Sun, Hui Wan, Jianhui Wang, Yan Xia, Zhao Xu, and Pei Zhang. Smart transmission grid: vision and framework. *IEEE Transction on Smart Grid*, 1:168–177, 2010.

[78] Gong Li, Jing Shi, and Junyi Zhou. Bayesian adaptive combination of short-term wind speed forecasts from neural network models. *Renewable Energy*, 36(1):352–359, 2011.

[79] T.B. Littler and D.J. Morrow. Wavelets for the analysis and compression of power system disturbances. *IEEE Transactions on Power Delivery*, 14:358–364, 1999.

[80] X. Liu. Economic load dispatch constrained by wind power availability: A wait-and-see approach. *IEEE transaction on smart grid*, 1:347–355, 2010.

[81] Petroula Louka, Georges Galanis, Nils Siebert, Georges Kariniotakis, Petros Katsafados, I Pytharoulis, and G Kallos. Improvements in wind speed forecasts for wind power prediction purposes using kalman filtering. *Journal of Wind Engineering and Industrial Aerodynamics*, 96(12):2348–2362, 2008.

[82] Qiang Lu, Yuanzhang Sun, and Shengwei Mei. *Nonlinear Control Systems and Power System Dynamics*. Springer, 2001.

[83] Jin Ma, Pu Zhang, Hongjun Fu, Bo Bo, and Zhaoyang Dong. Application of phasor measurement unit on locating disturbance source for low-frequency oscillation. *IEEE Transcation on Smart Grid*, 1:340–346, 2010.

[84] Jan Maciejowski. *Predictive Control with Constraints*. Prentice Hall, 2000.

[85] D.J.C. MacKay. *Information Theory, Inference, and Learning Algorithms*. Cambridge University Press, 2003.

[86] J.B. MacQueen. Some methods for classification and analysis of multivariate observations. In *Proceedings of 5th Berkeley Symposium on Mathematical Statistics and Probability*, 1967.

[87] S. Mallat. *A Wavelet Tour of Signal Processing*. Academic Press, 2008.

[88] S.G Mallat and Z Zhang. Matching pursuits with time-frequency dictionaries. *IEEE Transactions on Signal Processing*, 41:3397–3415, 1993.

[89] N. M. Manousakis, G. N. Korres, and P. S. Georgilakis. Taxonomy of pmu placement methodologies. *IEEE Transactions on Power System*, 27:1070–1077, 2012.

[90] M. A. Matos and R. J. Bessa. Setting the operating reserve using probabilistic wind power forecasts. *IEEE transaction on power systems*, 26:594–603, 2011.

[91] G. Michael, B. Stephen, and Y. Ye. Cvx: Matlab software for disciplined convex programming, version 2.0 beta. *Recent Advances in Learning and Control*, pages 95–110, 2012.

[92] J. Mora-Florez, V. Barrera-Nnez, and G. Carrillo-Caicedo. Fault location in power distribution systems using alearning algorithm for multivariable data analysis. *IEEE Transactions on Power Delivery*, 22:1715–1721, 2007.

[93] GK Morison, B Gao, and P Kundur. Voltage stability analysis using static and dynamic approaches. *IEEE Transactions on Power Systems*, 8(3):1159–1171, 1993.

[94] Khosrow Moslehi and Ranjit Kumar. A reliability perspective of the smart grid. *IEEE Transcations on Smart Grid*, 1:57–64, 2010.

[95] K Mosleshi and Ranjit Kumar. Smart grid - a reliability perspective. *Innovative Smart Grid Technologies*, pages 1–8, 2010.

[96] L. S. Moulin, A. P. A. da Silva, M. A. El-Sharkawi, and II R. J. Marks. Support vector machines for transient stability analysis of large-scale power systems. *IEEE Transactions on Power Systems*, 19:818–825, 2004.

[97] L. S. Moulin, A. P. Alves da Silva, M. A. El-Sharkawi, and R. J. Marks II. Support vector machines for transient stability analysis of large-scale power systems. *IEEE Transactions on Power Systems*, 19:818 – 825, 2004.

[98] E Muljadi, CP Butterfield, J Conto, and K Donohoo. Ride-through capability predictions for wind power plants in the ercot network. In *Power Engineering Society General Meeting, 2005. IEEE*, pages 72–79. IEEE, 2005.

[99] Jiaxin Ning, Jianhui Wang, Wenzhong Gao, and Cong Liu. A wavelet-based data compression technique for smart grid. *IEEE Transactions on Smart Grid*, 2, 2011.

[100] M. Ortega-Vazquez and D. Kirschen. Estimating the spinning reserve requirements in systems with significant wind power generation penetration. *IEEE Transactions on Power Systems*, 24:114–123, 2009.

[101] M. A. Ortega-Vazquez and D. S. Kirschen. Estimating the spinning reserve requirements in systems with significant wind power generation penetration. *IEEE Transactions on Power Systems*, 24:114–124, 2009.

[102] M.A. Pai. *Energy Function Analysis for Power System Stability.* Springer, 1989.

[103] Lucy Y Pao and Kathryn E Johnson. A tutorial on the dynamics and control of wind turbines and wind farms. In *American Control Conference, 2009. ACC'09.*, pages 2076–2089. IEEE, 2009.

[104] Mania Pavella, Damien Ernst, and Daniel Ruiz-Vega. *Transient Stability of Power Systems : A Unified Approach to Assessment and Control.* Springer, 2000.

[105] S.Joe Qin. and Thomas A. Badgwell. A survey of industrial model predictive control technology. *Control Engineering Practice*, 11:733–764, 2004.

[106] Lawrence R. Rabiner. A tutorial on hidden Markov models and selected applications in speech recognition. *Proceedings of the IEEE*, 77:257–286, 1989.

[107] L.R. Rabinger and B.H. Juang. An introduction to hidden Markov models. *IEEE ASSP Magazine*, 3:4–16, 1986.

[108] B. Ren and C. Jiang. A review on the economic dispatch and risk management considering wind power in the power market. *Renewable and Sustainable Energy Reviews*, 13:2169–2174, 2009.

[109] G.H. Riahy and M. Abedi. Short term wind speed forecasting for wind turbine applications using linear prediction method. *Renewable Energy*, 33:35–41, 2008.

[110] P. Rio and M. Burguillo. Assessing the impact of renewable energy deployment on local sustainability: Towards a theoretical framework. *Renewable and Sustainable Energy Reviews*, 12:1325–1344, 2008.

[111] B. K. Saha Roy, A. K. Sinha, and A. K. Pradhan. An optimal PMU placement technique for power system observability. *International Journal of Electrical Power and Energy Systems*, 8:71–77, 2012.

[112] P. A. Ruiz, C. R. Philbrick, E. Zak, K. W. Cheung, and P. W. Sauer. Uncertainty management in the unit commitment problem. *IEEE Transactions on Power Systems*, 24:642–651, 2009.

[113] Nicols Ruiz-Reyes, Pedro Vera-Candeas, and Francisco Jurado. Discrimination between transient voltage stability and voltage sag using damped sinusoids-based transient modeling. *IEEE Transactions on Power Delivery*, 20:2644–2650, 2005.

[114] B. Don Russell and Carl L. Benner. Intelligent systems for improved reliability and failure diagnosis in distribution systems. *IEEE Transactions on Smart Grid*, 1:48–56, 2011.

[115] Robert Salat and Stanislaw Osowski. Accurate fault location in the power transmission line using support vector machine approach. *IEEE Transactions on Power Systems*, 19:979–986, 2004.

[116] J. L. Sancha, J. L. Fernandez, A. Cortes, and J. Abarca. Secondary voltage control: analysis, solutions and simulation results for the spanish transmission system. *IEEE Transactions on Power Systems*, 11:630 – 638, 1996.

[117] JV Seguro and TW Lambert. Modern estimation of the parameters of the weibull wind speed distribution for wind energy analysis. *Journal of Wind Engineering and Industrial Aerodynamics*, 85(1):75–84, 2000.

[118] DIH Sun, S Abe, RR Shoults, M-S Chen, P Eichenberger, and D Farris. Calculation of energy losses in a distribution system. *IEEE Transactions on Power Apparatus and Systems*, (4):1347–1356, 1980.

[119] J. Tate and T. Overbye. Double line outage detection using phasor angle measurements. *IEEE Power and Energy Society General Meeting*, pages 1–5, 2009.

[120] Joseph Euzebe Tate and Thomas J. Overbye. Line outage detection using phasor angle measurements. *IEEE Transcations on Power Systems*, 23:1644–1652, 2008.

[121] J. Teyssen and M. Fuchs. Wind report 2005. Technical report, E.ON Energie AG, 2005.

[122] J. L. Torres, A. Garc, M. D. Blas, and A. D. Francisco. Forecast of hourly average wind speed with arma models in navarre (spain). *Solar Energy*, 79:65–77, 2005.

[123] M. Vaiman, S. Maslennikov, E. Litvinov, and X. Luo. Calculation and visualization of power system stability margin based on PMU measurements. *IEEE Smart Grid Communication*, pages 31–36, 2010.

[124] Eknath Vittal, Mark O'Malley, and Andrew Keane. A steady-state voltage stability analysis of power systems with high penetrations of wind. *IEEE Transactions on Power Systems*, 25(1):433–442, 2010.

[125] Bin Wang, Wilsun Xu, and Zhencun Pan. Voltage sag state estimation for power distribution systems. *IEEE Transactions on Power Systems*, 20:806–812, 2005.

[126] J. Wang, M. Shahidehpour, and Z. Li. Contingency-constrained reserve requirements in joint energy and ancillary services auction. *IEEE transaction on power system*, 24:1457–1468, 2009.

[127] J. Wang, X. Wang, and Y. Wu. Operating reserve model in the power market. *IEEE Transactions on Power Systems*, 20:223–229, 2005.

[128] Jianhui Wang, Mohammad Shahidehpour, and Zuyi Li. Security-constrained unit commitment with volatile wind power generation. *Power Systems, IEEE Transactions on*, 23(3):1319–1327, 2008.

[129] L. Wang and C. Singh. Balancing risk and cost in fuzzy economic dispatch including wind power penetration based on particle swarm optimization. *Electric Power Systems Research*, 78:1361–1368, 2008.

[130] Q. Wang, Y. Guan, and J. Wang. A chance-constrained two-stage stochastic program for unit commitment with uncertain wind power output. *IEEE transaction on power system*, 27:206–215, 2012.

[131] Yang Wang and S. Boyd. Fast model predictive control using online optimization. *IEEE Transactions on Control Systems Technology*, 18:267–278, 2010.

[132] Zhuding Wang, Fen Chen, and Jingui Li. Implementing transformer nodal admittance matrices into backward/forward sweep-based power flow analysis for unbalanced radial distribution systems. *IEEE Transactions on Power Systems*, 19(4):1831–1836, 2004.

[133] L. Wehenkel, M. Pavella, E. Euxibie, and B. Heilbronn. Decision tree based transient stability method a case study. *IEEE Transactions on Power Systems*, 9:459–469, 1994.

[134] L. Wehenkel, T. van Cutsem, and M. Ribbens-Pavella. An artificial intelligence framework for on-line transient stability assessment of power systems. *IEEE Transactions on Power Systems*, 9:789–800, 1989.

[135] R. Wiser and M. Bolinger. 2011 wind technologies market report. Technical report, Lawrence Berkeley National Laboratory, 2011.

[136] Xiaorong Xie, Yaozhong Xin, Jinyu Xiao, Jingtao Wu, and Yingduo Han. Wams applications in chinese power systems. *IEEE Power and Energy Magazine*, 4(1):54–63, 2006.

[137] Chunchun Xu, Zhian Zhong, Virgilio Centeno, Richard Conners, and Yilu Liu. Practical issues in frequency disturbance recorder design for wide-area monitoring. *Electrial Power Quality and Utilisation*, 11:69–76, 2005.

[138] Tai-Her Yeh and Li Wang. A study on generator capacity for wind turbines under various tower heights and rated wind speeds using weibull distribution. *IEEE Transactions on Energy Conversion*, 23(2):592–602, 2008.

[139] T. Yong, R. Entriken, and P. Zhang. Reserve determination for system with large wind generation. *IEEE Power & Energy Society General Meeting*, pages 1–7, 2009.

[140] Fan Zhang and Carol S Cheng. A modified newton method for radial distribution system power flow analysis. *IEEE Transactions on Power Systems*, 12(1):389–397, 1997.

[141] Zhian Zhong, Chunchun Xu, Bruce J. Billian, Li Zhang, Shu Steven Tsai, Richard W. Conners, Virgilio A. Centeno, Arun G. Phadke, and Yilu Liu. Power system frequency monitoring network (FNET) implementation. *IEEE Transactions on Power Systems*, 20:1914–1921, 2005.

[142] Ray D Zimmerman and Hsiao-Dong Chiang. Fast decoupled power flow for unbalanced radial distribution systems. *IEEE Transactions on Power Systems*, 10(4):2045–2052, 1995.